Spring 2022

Melanin pigments as antibacterial agents

Tahmineh Rahmani Eliato
University of New Hampshire, Durham

Melanin pigments as antibacterial agents

By

Tahmineh Rahmani Eliato

B.S. Chemical Engineering

M.S. Chemical Engineering

DISSERTATION

Submitted to the University of New Hampshire

In Partial Fulfillment of

the Requirements for the Degree of

Doctor of Philosophy

In

Chemical Engineering

May 2022

This dissertation was examined and approved in partial fulfillment of the requirements for the degree of Doctor of Philosophy in Chemical Engineering by:

Young Jo Kim, Ph.D.,
Dissertation Director
Assistant Professor, Chemical Engineering
University of New Hampshire

Cheryl P. Andam, Ph.D.,
Assistant Professor, Biological Sciences
University at Albany, State University of New York

Kyung Jae Jeong, Ph.D.,
Associate Professor, Chemical Engineering
University of New Hampshire

Linqing Li, Ph.D.,
Assistant Professor, Chemical Engineering
University of New Hampshire

Kang Wu, Ph.D.,
Associate Professor, Chemical Engineering
University of New Hampshire

On May 4, 2022

Approval signatures are on file with the University of New Hampshire Graduate School.

This dissertation is dedicated to my husband for his love, support, and encouragement.

ACKNOWLEDGEMENTS

First, I wish to express my gratitude and special thanks to my advisor Dr. Young Jo Kim for his guidance.

I want to thank my committee members Dr. Cheryl Andam, Dr. Kyung Jae Jeong, Dr. Kang Wu, and Dr. Linqing Li for providing their time and input to improve my thesis.

I am grateful to Dr. Andam for kindly allowing me to work in her lab at university of New Hampshire where I learned a lot about bacteria.

I would like to thank Darcy Fournier at the Chemical Engineering Department for her technical assistance in experimental set-up and Amy Michaud at the Department of Molecular, Cellular and Biomedical Sciences for providing type strains of *Staphylococcus aureus* and *Escherichia coli*.

I would like to acknowledge the financial support provided by the following organizations: National Science Foundation EPSCoR award (1757371), UNH Collaborative Research Excellence (CoRE) Initiative, and UNH College of Engineering and Physical Sciences (CEPS), New Hampshire Center for Multiscale Modeling and Manufacturing of Biomaterials (NH BioMade).

Finally, I would like to thank my husband, parents, and brother for their love, patience, and advice during these years.

TABLE OF CONTENTS

SECTION PAGE

LIST OF TABLES

TABLE PAGE

LIST OF FIGURES

FIGURES PAGE

ABSTRACT
Melanin pigments as antibacterial agents

By Tahmineh Rahmani Eliato

University of New Hampshire, May 2022

In this dissertation I investigated the structural properties of melanin biopigment from different sources as an antibacterial and endotoxin bonding agent. I extracted melanin from *Equus ferus* hair with acid hydrolysis (termed *Equus*Mel) and characterized it by microscopic and spectroscopic techniques. Scanning electron microscopy (SEM) and transmission electron microscopy (TEM) revealed that *Equus*Mel is mainly elliptical in shape with a mesoporous and layered structure within the individual particles. Wide-angle (WAXS) and small-angle (SAXS) X-ray scattering measurements demonstrated a semicrystalline multilayered structure with order spacing of 45.2 Å. Pore size distribution determined by the Barrett–Joyner–Halenda (BJH) method showed primary pores within the range of 30–50 Å. Nitrogen adsorption–desorption isotherms exhibited a Brunaur–Emmett–Teller (BET) surface area of 3 m^2/g. Raman, X-ray photoelectron spectroscopy (XPS), and Fourier transform infrared spectroscopy (FTIR) spectra revealed similar chemical signature between *Equus*Mel and synthetic melanin (SynMel). I investigated the antibacterial effect and its mechanism of action for *Equus*Mel. I found that *Equus*Mel has distinct antibacterial activity due to its potential to generate reactive oxygen species (ROS). ROS generated via oxidation of catechols is considered the main mechanism of antibacterial activity. The simplicity of *Equus*Mel extraction and its antibacterial property allows this biomaterial to be

applicable to a variety of areas. Zinc cations (Zn^{2+}) were loaded on melanin structure (Mel-Zn) for rapid and selective separation of gram-negative bacteria and lipopolysaccharide (LPS) from blood. Mel-Zn was characterized by XPS and Raman which revealed the successful Zn^{2+} loading. I identified that Mel-Zn rapidly captures approximately 90% of *Escherichia coli* in whole blood and 100% of LPS in PBS, which can reduce bacteremia loads and mitigate the spread of these infectious agents to other tissues and organs. Additionally, simultaneous binding to bacteria and LPS could enhance the efficacy of antibiotic therapy. Adsorption of protein from individual protein model solutions, as well as LPS-spiked protein solutions, was found to be minimal. Hemolysis and coagulation assays demonstrate the blood biocompatibility of Mel-Zn, which could be adapted for clinical use in an extracorporeal membrane to remove pathogens and LPS in acute sepsis patients.

CHAPTER 1
Background

1.1 Melanin

Among the broad variety of biopolymers found in nature, few have such unique and far-reaching applications as melanin. Melanin is a polyphenolic material broadly found in almost all types of living organisms, such as fungi, bacteria, animals, and plants [1], [2]. In animals, melanin can be found in the skin, hair, iris of the eye, some neurosensorial tissues, and the ink sac of *Sepia officinalis* (cuttlefish) [3]–[5].

Melanin has many well-studied characteristic properties such as: a broad band UV-Vis absorption, a distinct electron paramagnetic resonance (EPR) signal, free radical scavenging, antioxidant, and anti-tumor activity [6]–[9]. The diversity of its functional roles across life is a result of different complex forms that polymerize in different ways. In pathogenic fungi, melanin has been demonstrated as a virulence factor, acting against host defense mechanisms [10]. Conversely, melanin located in human *substantia nigra* may play a role in brain aging and neurodegeneration [5]. Beyond humans, the synthesis of melanin in insects is used to encapsulate pathogens [11]. In recent decades, the broad range of technological opportunities offered by the physicochemical and biological properties of melanin has generated significant interest in studying this biomolecule.

Melanin extracted from sepia ink has been used widely as one of the natural sources of melanin. A simple centrifuge and washing extraction steps [12] have made this source of melanin easy to produce and commercially available by Sigma-Aldrich. Mammalian dark hair and feather

are other popular melanin sources. To separate melanin pigments that are imbedded in the cortex layer of hair or disrupt the keratin matrix in feather, various techniques such as base dissolution & acid isolation, dissolution in ionic liquid, acid hydrolysis, and enzymatic extraction have been applied [13]. Retinal pigment epithelium (RPE) melanosomes are other natural sources of melanin which have been extracted and extensively studied [4]. The method of extraction and isolation depends on the melanin source, localization of melanin pigments, and the purpose of the extraction. Most of these extraction processes occur in harsh conditions which often result in alteration to the melanin structure. Further, melanin sourced from animals presents ethical concerns as the animal from which melanin is extracted may need to be killed.

1.1.1 Biosynthesis pathway of melanin

Natural melanin generally is an insoluble compound in aqueous and organic solvents, and its forced solubilization alters its structure. This has made studying the physicochemical structure of melanin difficult. Moreover, melanin can be synthesized through different pathways that use distinct intermediate products and enzymes, this suggests that melanin may possess a diversity of structures, resulting in many distinct activities [14].

1.1.1.1 Eumelanin

Dark-brown eumelanin is obtained from tyrosinase catalyzed oxidation of tyrosine or 3,4-dihydroxyl-L-phenylalanine (L-Dopa) to L-Dopaquinone and L-Dopachrome. L-Dopachrome undergoes aromatization to give 5,6-dihydroxyindole (DHI) and 5,6-dihydroxyindole-2-carboxylic acid (DHICA) intermediates [15]. As depicted in **Figure 1.1** polymerization of DHI

and DHICA forms eumelanin pigment. Investigating the structure of eumelanin with spectroscopic analysis methods is challenging due to insolubility of the final pigment. However, the DHI/DHICA ratio in eumelanin biopolymer impacts the number of carboxylic acids, which further alters its free radical scavenging property [8]. Examples of eumelanins include those extracted from sepia ink and dark mammalian fibers.

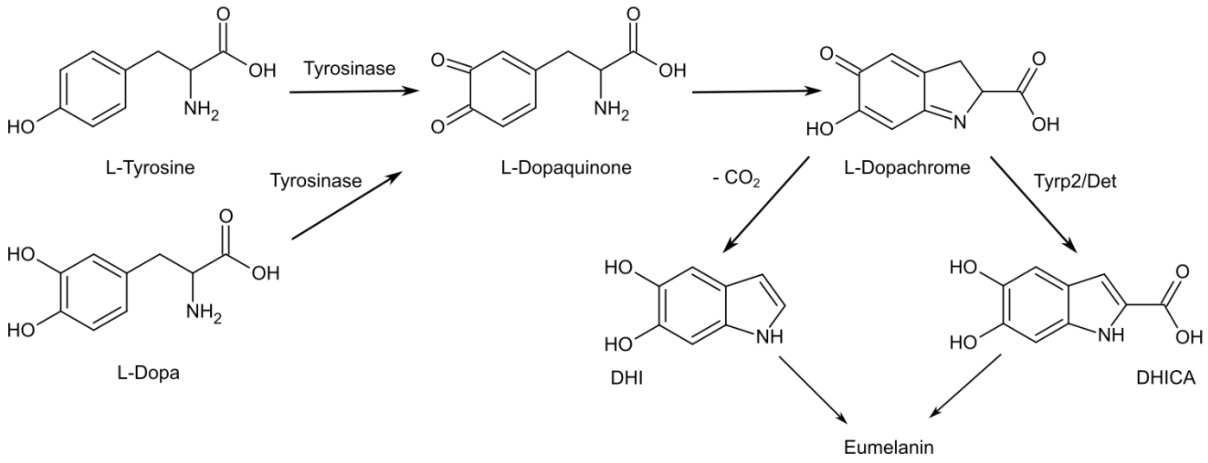

Figure 1.1: As one of the most studied melanogenesis pathways, biosynthesis of eumelanin initiates with oxidation of amino acid L-Tyrosine or 3,4-dihydroxyl-L-phenylalanine (L-Dopa) to L-Dopaquinone. Eumelanin intermediates 5,6- dihydroxyindole (DHI), 5,6-dihydroxyindole-2-carboxylic acid (DHICA) are polymerized to make the eumelanin pigment. Tyrosinase related protein 2 (Tryp 2).

1.1.1.2 Pheomelanin

Synthesis of pheomelanin, a sulfur containing pigment, is the result of a metabolic shift in the eumelanin pathway. The initial phase of the pathway, which is oxidation of L-Tyrosine to L-Dopaquinone, is the same for both eumelanin and pheomelanin, however, pheomelanin is derived from L-dopaquinone in the presence of L-Cysteine or other thiol containing compounds such as glutathione [16]. As demonstrated in **Figure 1.2** benzothiazine and benzothiazole intermediates

are formed by oxidation of 5-S-cysteinyldopa and 5-S-cysteinyldopaqunons and further polymerize to form the light yellow pheomelanin [17].

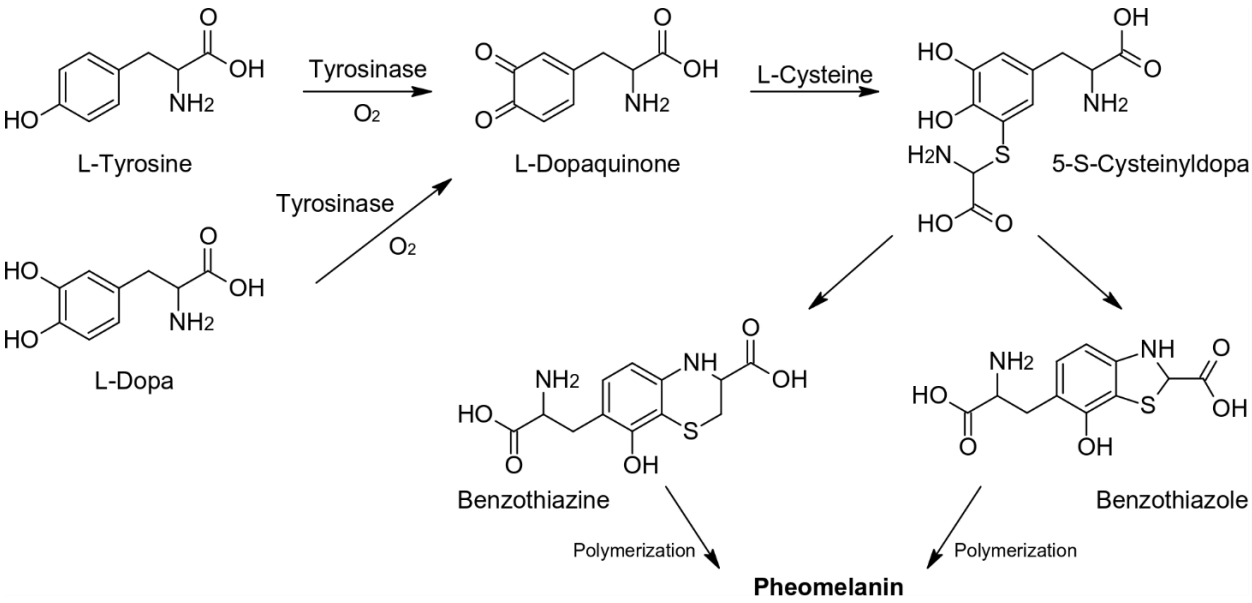

Figure 1.2: The initial biosynthesis pathway of pheomelanin is similar to eumelanin. L-Dopaquinone is the key molecule in both pathways, which in the presence of L-Cysteine gives a place to pheomelanin intermediates benzothiazine and benzothiazole. 3,4-dihydroxyl-L-phenylalanine (L-Dopa).

1.1.1.3 Allomelanin

In the pathway generating another form, allomelanin (or DHN-melanin), malonyl CoA or acetyl CoA undergo cyclization by polyketide synthase that yields 1,3,6,8-tetrahydroxy naphthalene (THN). This tetrahydroxy derivative is then transformed to the main melanin precursor, 1,8-dighydroxynaphthalene (DHN). Laccase or another phenol oxidase can catalyze naphthalene to naphthalene quinone, and the final pigment is formed by polymerization of DHN and its quinone form [18] (**Figure 1.3**).

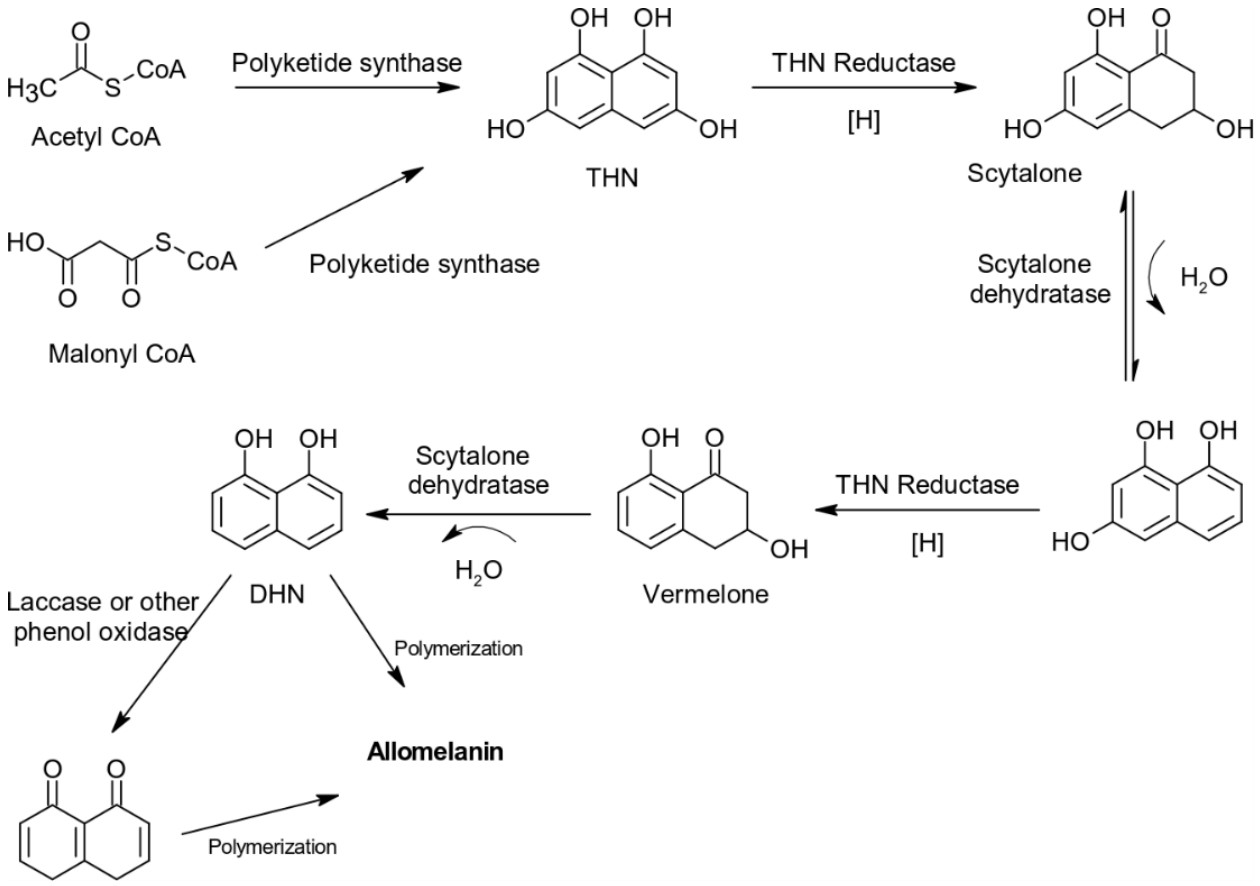

Figure 1.3: As the result of polyketide synthase action in allomelanin biosynthesis pathway,1,3,6,8-Tetrahydroxy naphthalene (THN) is formed. Passing through the formation of Scytalone and vermelone, 1,8-dighydroxynaphthalene (DHN) is synthesized and polymerized to form allomelanin along with its oxidized form quinone.

1.1.1.4 Pyomelanin

The pyomelanins are known to support microorganisms during various environmental stress. In the pyomelanin formation pathway, L-tyrosine undergoes transamination to form p-hydroxyphenyl pyruvate (HPP), which then generates homogentisic acid (HGA) through p-hydroxyphenyl dioxygenase action. Accumulation of HGA induces the oxidation to benzoquinone acetic acid (BQA) via laccase or other phenol oxidase. Like other types of melanin, p-diphenol and p-quinone polymerization leads to the formation of pyomelanin [16] (**Figure 1.4)**.

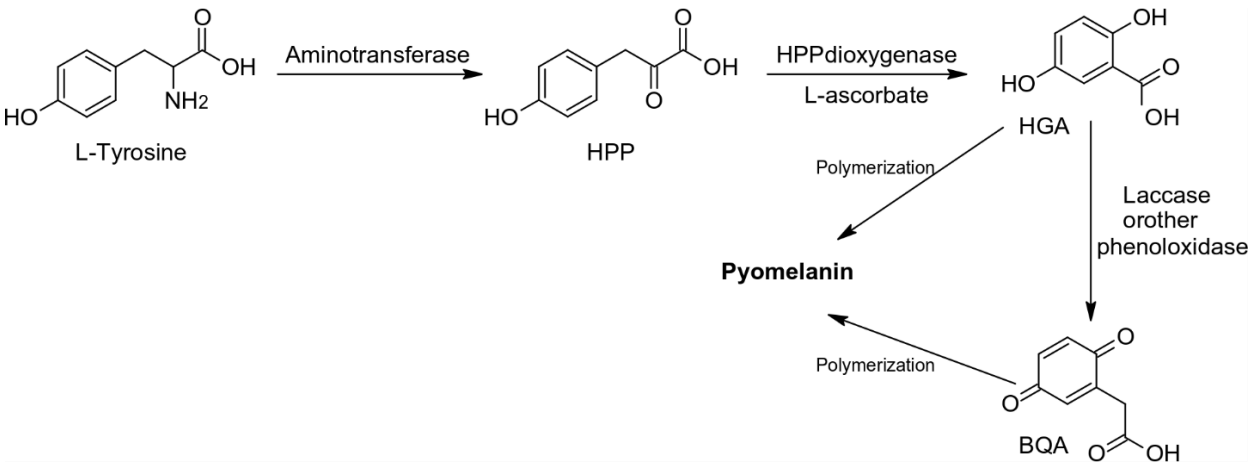

Figure 1.4: Pyomelanogenesis starts with amino acid L-Tyrosine transamination to p-hydroxyphenyl pyruvate (HPP). Homogentisic acid (HGA) and benzoquinone acetic acid (BQA) are then formed and polymerized to Pyomelanin.

1.1.2 Synthetic melanin

Melanin can be synthesized *in vitro* through reactions that resemble the natural biological pathway of melanin synthesis [13]. Oxidation of dopamine hydrochloride is one popular method for preparing a dark melanin-like material known as polydopamine or dopamine melanin (DOPA) (**Figure 1.5**). This polymerization can be mediated by Tris-Hcl buffer, sodium hydroxide, sodium bicarbonate/sodium carbonate buffer and phosphate-buffered saline (PBS) [19]. With excellent adhesion and coating properties, dopamine melanin has been studied in a variety of applications such as bioelectronics, antimicrobial agents and, membrane and surface modifications [20]–[22]. Synthetic melanin often presents a heterogeneous amorphous form, while natural melanin is made up of homogeneous spherical/elliptical aggregated nanoparticles [23]. Different structural properties between synthetic and natural melanin likely results in better performance of natural melanin in biotechnological applications. For example, cyclic voltammetry measurement reveals

that natural melanin exhibits specific capacity that is 50% higher than synthetic melanin in aqueous sodium ion batteries [24].

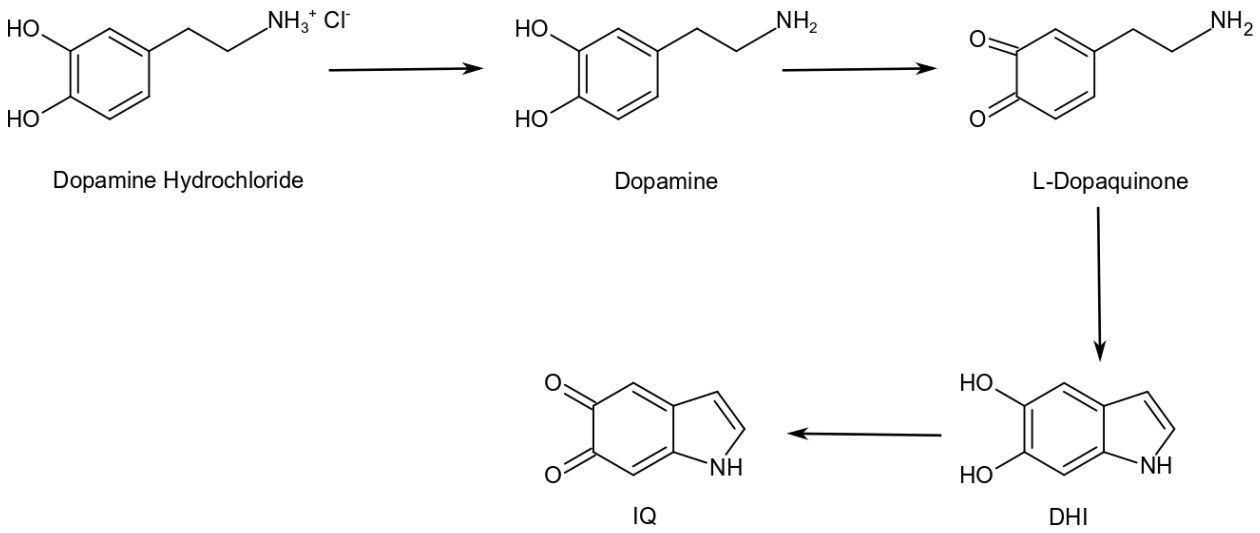

Figure 1.5: Synthesis of synthetic melanin and the chemical intermediates. Indole-5,6-quinone (IQ); 5,6-Dihydroxyindole (DHI).

1.2 Characteristics of eumelanin

1.2.1 Structure

1.2.1.1 Microstructure

Scanning electron microscopy (SEM) and transmission electron microscopy (TEM) are powerful methods for the morphological characterization and particle size analysis of melanin. Eumelanin extracted from *S. officinalis* ink consists of homogeneous spherical nanoparticle aggregates with characteristic dimensions of 100–300 nm confirmed by electron microscopy (**Figure 1.6a**) [24]. However, eumelanin extracted from other sources such as hair or eyes are generally elliptical with larger dimensions (**Figure 1.6b**) [25].

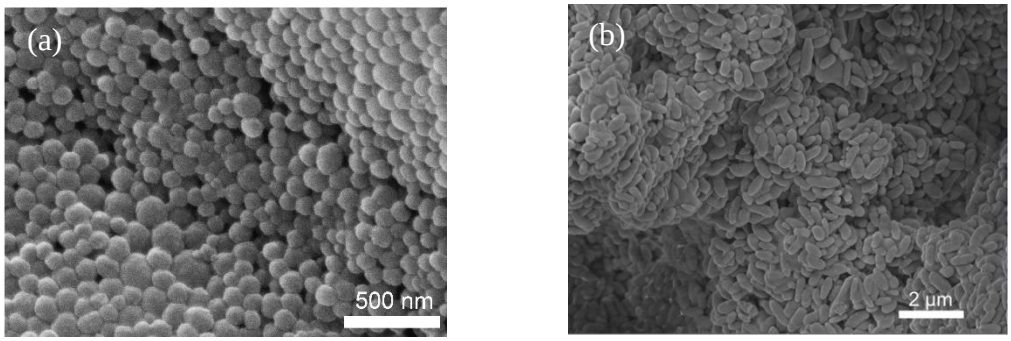

Figure 1.6: (a) Melanin extracted from S. officinalis ink [24] and (b) horsehair [25].

1.2.1.2 Meso-structure

The development of novel methods for studying condensed-matter physics, electrochemistry, and chemistry of materials, including imaging techniques and theoretical calculations, has facilitated the study of meso-scale structure of melanin [26]. As mentioned previously, eumelanin pigments are composed of randomly polymerized tetramer units of DHI and DHICA monomers. These protomolecules use strong π–π stacking that promote self-assembly into spherical nanostructures with an intermolecular spacing of 3.8 Å (**Figure 1.7**) [4]. The study of broadband UV–Vis absorption spectra of eumelanin, and the associated optoelectronic properties, have been considered essential for elucidation of its molecular structure. The broadband featureless UV–Vis spectra of melanin can be explained by the chemical disorder model. This model proposes that natural eumelanin consists of many chemically distinct protomolecules. The broadband absorption is calculated as the average of the different absorptions of every species in the UV–Vis range [26].

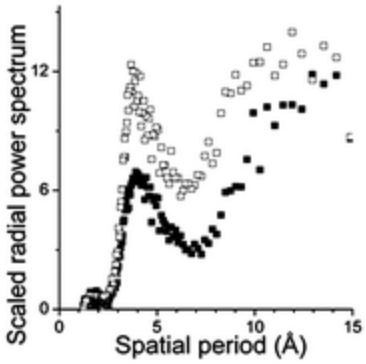

Figure 1.7: The two-dimensional discrete Fourier transform indicates that the inter-sheet spacings within melanin protomolecules are between 3.7 and 4.0 Å [4].

These protomolecules are arranged with a defined interlayer distance, forming onion-like nanostructures. The oligomers are mainly formed by bi-indole cross-linked covalent bonds between units. These covalently bonded units are symmetrical, and a porphyrin-like tetramer structure has been proposed as the meso-structure. This arrangement of the four protomolecules has the potential to bind with monovalent ions in the core and create larger molecules with high potential energy storage properties usable in batteries [27].

1.2.2 Chemistry of major functional groups

The monomers (DHICA) in eumelanin have catechol, carboxylic acid, and amine as main functional groups. A catechol is an unsaturated six-carbon ring (phenolic group) with two hydroxyl groups attached to adjacent carbons (dihydroxyphenol). The variety of functional groups in eumelanin, in particular the catechol moieties, provide affinity to metal ions. Something about pKa here? This property was applied for metal ion extraction from aqueous solutions, thus providing a beneficial environmental impact to remove heavy metal ions from water [28]. The property of

binding and releasing metal ions also makes eumelanin an ideal material in biodegradable batteries [24]. Further, the redox activities of catechol groups are a potential resource for clinical applications. Catechol oxidation by air generates H_2O_2 and $O_2^{\cdot -}$ as reactive byproducts, which can potentially be used for antimicrobial and antiviral applications [29]. Finally, amines are ubiquitous functional groups in biological systems. Hydrogen bonding significantly influences the properties of primary and secondary amines. Secondary aromatic amine group in eumelanin structure facilitates bonding with monovalent ions [27].

1.2.3 Interaction with ions in aqueous system

Eumelanin is associated with several metal ions and has the capability to incorporate metal ions within its structure. While the capacity of eumelanin to bind Ca^{2+} or Zn^{2+} is high, its affinity for these two metal ions is only moderate. This enables eumelanin to accumulate these two metal cations and then, under certain conditions release them. The relative binding affinities are in the order $Ca^{2+} < Zn^{2+} < Fe^{3+} < Cu^{2+}$, which suggests that Zn^{2+} binds to melanin stronger than Ca^{2+} [73].

Multivalent cations such as Mg^{2+}, Ca^{2+}, Fe^{3+} can bind to eumelanin through Coulombic interactions with carboxylic acids or coordination bond formation with catechols. While the electrochemistry of divalent cation–catechol bonding is well characterized, the binding locations of monovalent cations with eumelanin is more diverse owing to the broad range of prospective binding sites to indole-based subunits. Monovalent cations such as Na^+ associate with aromatic amines, in melanin structure (**Figure 1.8**) [27].

The variety of functional groups in eumelanin, in particular the catechol moieties, provide differential affinities to metal ions largely influenced by differences in pKa values of the functional groups and the pH of the initial solution [73]. Carboxylic acid, hydroxyl, and amine groups in eumelanin have pKa values of ~4.5, ~9-13, and >10, respectively. At a more acidic initial solution, carboxylic acids are mostly deprotonated and have higher affinity to metal binding [74]. Conversely, in less acidic initial solutions, hydroxyl and amine groups more often bind to metal ions. It should also be noted that this can lead to changes in the pH of the solution as protons are released [73].

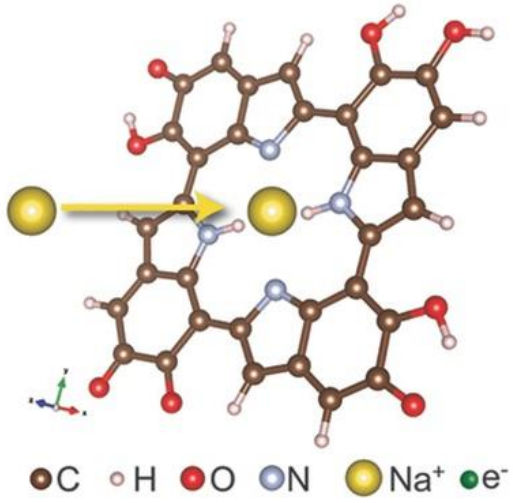

Figure 1.8: Porphyrin-like tetramers in melanin that permit sodium ion insertion [27].

1.3 Antimicrobial agents

Bacterial adhesion, growth, and proliferation on surfaces produce sticky and thick biofilms with low permeability [30]. Biofilm formation on membranes, wet surfaces, medical devices, and within host tissues during infection are major environmental and health issues. Over the past century, antibiotics have been developed and preferred treatments method for bacterial infections.

However, extensive research has shown the development of resistance to virtually every class of antibiotic. Identifying and developing new and effective antimicrobial agents would be of great importance.

1.3.1 State-of-the-art antimicrobial agents

Recently, nanoparticles have gained a great deal of attention as an antimicrobial agent. Most currently used antimicrobial therapies target bacterial machinery within the cell, which has created strong selective pressures for variant strains to evolve to overcome or circumvent those therapies. Over time these variants have emerged, with some "superbugs" resistant to all or nearly all known drugs. Because the mechanisms by which nanoparticles act as antimicrobial agents usually involves only direct contact with the exterior of the cell wall, there may be a lower probability of resistance emerging [31], [32]. Metal nanoparticles such as copper (Cu), titanium (Ti), silver (Ag), zinc (Zn), Selenium (Se) and Silicone (Si) have been wildly studied for their antimicrobial properties [33]–[36]. A more recent approach is to create biocompatible and environmentally friendly antimicrobial agents such as antimicrobial peptides or melanin nanoparticles [37]. The antimicrobial mechanism of action of nanoparticles is generally described as one of three models: oxidative stress induction, metal ion release, or non-oxidative mechanisms (**Figure 1.9**) [31]. Oxidative stress occurs as certain molecules with strong positive redox potential, including H_2O_2, $O_2^{\cdot-}$, $^{\cdot}OH$, and O_2, build up and induce a highly damaging oxidative state that can kill cells, primarily by impacting cell membrane permeability. Metal ion release across the cellular membrane is another model of antimicrobial mechanism, which interact with functional groups in nucleic acids and proteins to alter their structure or function; however, their impact is relatively weak compared to other models and is generally supplemental to other mechanisms. Finally, one

non-oxidative mechanism using MgO nanoparticles is capable of killing bacterial cells via a combination of factors, including disruptive attachment to phosphate groups on the surface of the cell, induction of pH change, and release of Mg^{2+}, which disrupts the cellular membrane. Further, these three types of mechanisms can occur simultaneously.

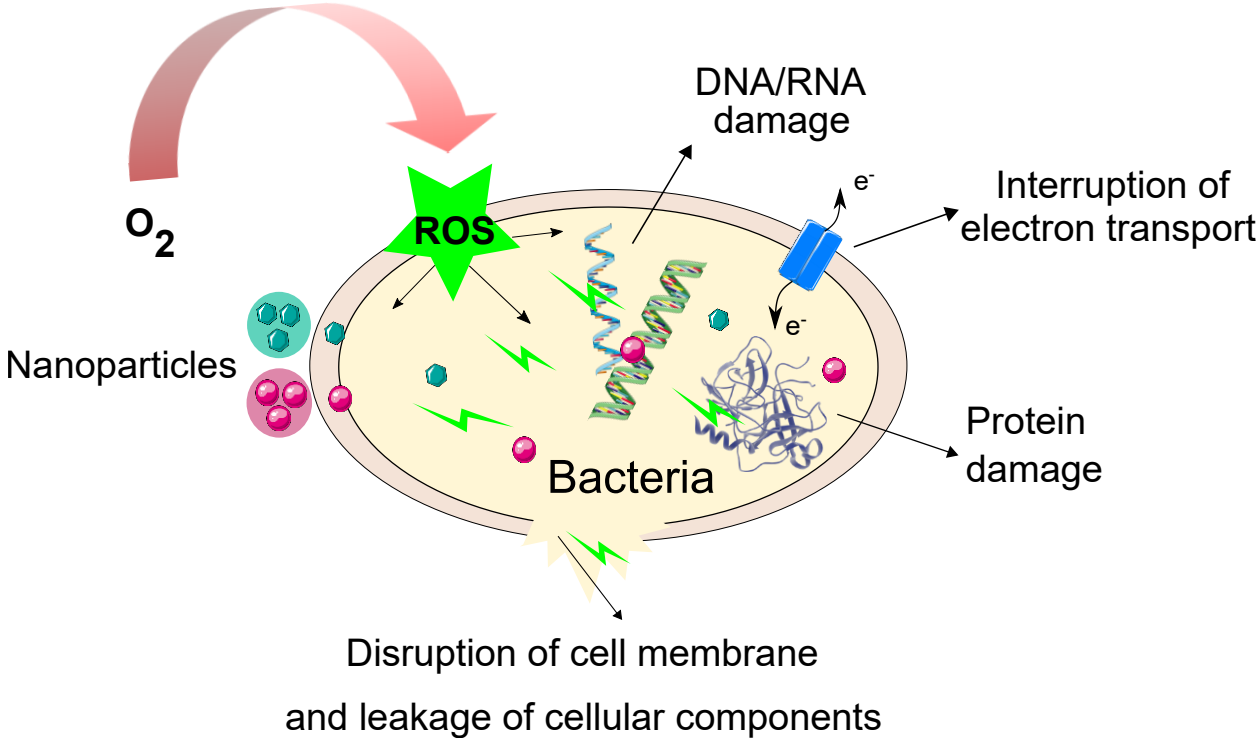

Figure 1.9: Mechanisms of antibacterial activity of nanoparticles.

Ag nanoparticles are considered the most common inorganic nanoparticles used as antimicrobial agents. The antimicrobial application of Ag additives is widely studied in various plastic and biopolymer products, textiles, and coating-based materials. It has been demonstrated that Ag nanoparticles have antimicrobial activity against a wide range bacteria and viruses. The antibacterial mechanism of Ag nanoparticles results in damage of the outer membrane bacteria. Ag nanoparticles can induce pits and gaps in the bacterial membrane and eventually fragment the

cell. Additionally, Ag ions interact with and disrupt disulfide and sulfhydryl groups, which play important roles in protein structure and protection against DNA damage from oxidative stress. These disruptions are capable of leading to cell death [32].

1.3.2 Antimicrobial activity of melanin

The catechol group is a key functional component of the melanin structure. As mentioned earlier, catechol group oxidations involve the electron transfer that converts the O_2 into superoxide ($O^{\cdot-}_2$) and hydrogen peroxide (H_2O_2). Oxygen free radicals and any other oxygen-containing molecule in which an oxygen atom has a greater reactivity than molecular oxygen is considered reactive oxygen species (ROS). Previous publications have reported generation of these ROS during catechol oxidation in melanin. The release of H_2O_2 from catechol oxidation was found to facilitate both antimicrobial and antiviral activity [38].

Researchers have designed bioadhesives and coatings using the adhesive moiety catechol to mimic the strong adhesion capability of mussel adhesive proteins. To accomplish this, 3,4-dihydroxyphenylalanine (DOPA) was incorporated into microgels, which generates millimolar levels of H_2O_2 by simply hydrating the microgels. The sustained release of H_2O_2 was both antimicrobial and antiviral, notably inactivating biocide resistant non-enveloped viruses. The simplicity of this design will enable this biomaterial to function as a lightweight and portable source of disinfectant for a wide range of applications [29].

The antimicrobial activity of melanins from different biological origins such as bacteria, fungi, and human hair has been studied in a number of settings. Studies have shown that commercial synthetic melanin (Sigma Aldrich^{TM}) had an antifungal activity against *Candida*

albicans and other *Candida spp.*, such as *Candida parapsilosis* strain 22019, *Candida glabrata* strain 2001, *Candida krusei* strain 6258 [39]. Interestingly, an inhibiting activity has been observed in isolates of *Candida spp.* resistant to fluconazol. Correa et al. extracted melanin from black hair through an acid/base method [14]. The high-performance liquid chromatography (HPLC) patterns of human and fungal melanins were similar to the synthetic melanin obtained through the oxidation of tyrosine, which demonstrates that both human and fungal melanins contain eumelanin as their principal element. Human melanin showed a significantly higher antifungal activity against both *Cryptococcus neoformans* and *Cryptococcosis gattii*, compared to the synthetic and fungal melanins. In addition, this antifungal activity against clinical isolates obtained from patients was higher than the reference strains.

Pigments like melanin produced across diverse fungal and bacterial taxa play an important role in their ecological relationships among other microbes as well as with colonized hosts by limiting microbial growth of competing microbes [40]. One bacterial taxon found ubiquitously across different environments that has been repeatedly demonstrated to produce a melanin pigment with antimicrobial activity is *Pseudomonas*. Many of the species in this genus live in complex relationships with eukaryotic hosts that can be symbiotic or pathogenic in how they limit microbial growth. Additionally, the production of melanin pigments is often regulated in response to environmental pressures [41]. In one example, certain *Pseudomonas putida* strains that colonize grass rhizosphere can produce a dark melanin pigment in response to the presence of phytopathogens, limiting growth of the pathogens and protecting the plant from damage [42].

Notably, the antimicrobial effects of melanin are often broad spectrum, showing growth inhibition of important clinical species that also inhabit a wide range of environments [43], [44], such as *Escherichia coli*, *Pseudomonas aeruginosa*, *Staphylococcus aureus*, and *Mycobacterium*

smegmatis. In one study, melanin produced by a *Bacillus subtilis* strain colonizing a *Salicornia* plant demonstrated strong antimicrobial effects against many plant, marine, and human pathogens. Due to these effects against diverse taxa, the mechanism of action likely impacts highly conserved bacterial structures or pathways common to both gram-negative and gram-positive bacteria (**Figure 1.10**) [45].

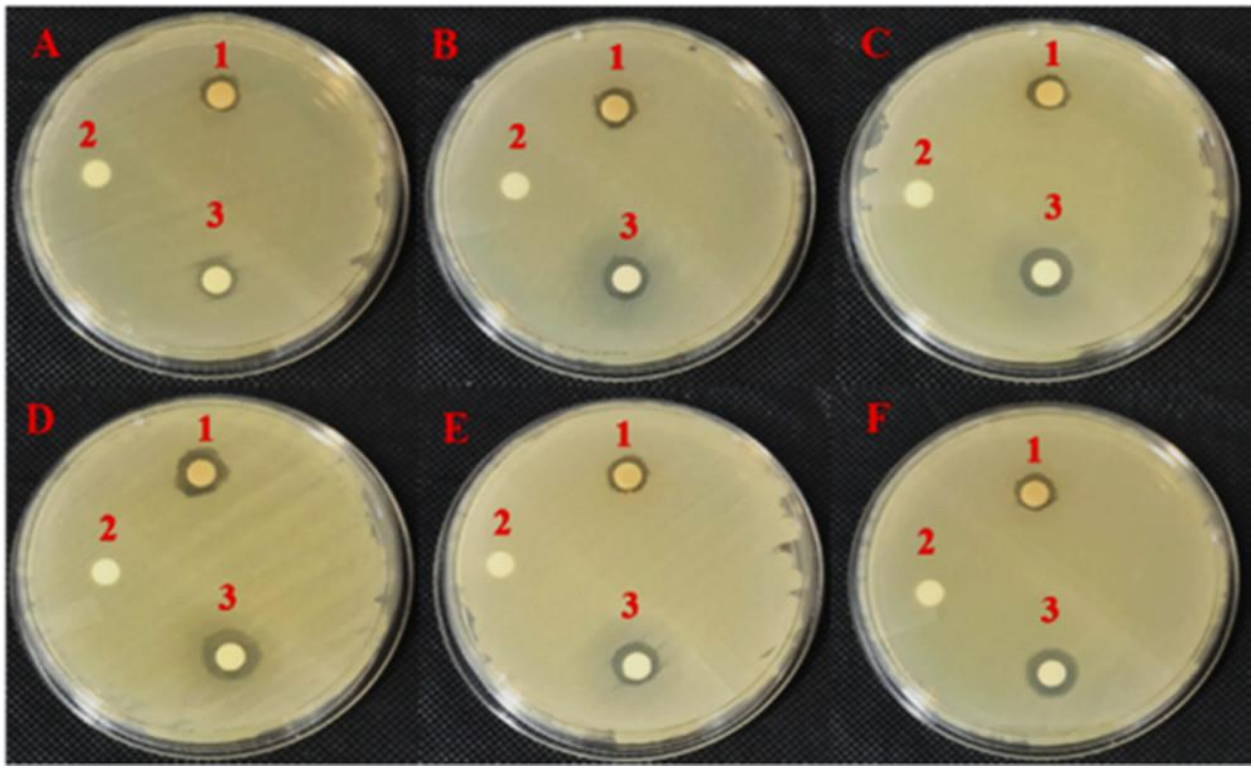

Figure 1.10: Antimicrobial activity of purified melanin. (A) *K. pneumoniae* MCC 2451, (B) *A. macleodii* MCC 2815, (C) *E. coli* MCC 2412, (D) *M. smegmatis* MTCC 6, (E) *E. aerogenes* MCC 3092, and (F) *X. campestris* NCIM 5028; (1 = melanin, 2 = negative control, 3 = standard antibiotics) [45].

In Chapter 2, I extract melanin from horsehair and study its antimicrobial activity (**Figure 1.11**). I show that extracted melanin biopigments have a homogeneous elliptical microstructure with highly ordered semicrystalline features. Raman, Fourier transform infrared (FTIR), and X-ray photoelectron spectroscopy (XPS) suggest that extracted melanin has similar chemical

signatures to melanins extracted from *S. officinalis* and synthetic melanin. I test the antibacterial activity of melanin by incubating *E. coli* and *S. aureus* with melanins and investigate the mechanism of action via reactive oxygen species (ROS) generation.

Figure 1.11: Melanin extracted from horsehair as antibacterial agent [25].

1.4 Endotoxin removal form blood

Endotoxin, or lipopolysaccharide (LPS), is a major component of the cell wall of gram-negative bacteria. When endotoxins are released into the bloodstream, a strong reactive response is generated by the immune system, which can develop into life-threatening sepsis. Notably, endotoxin is one of the strongest bacterial inducers of inflammatory cytokines [46]. The massive systemically dysregulated cytokine response, referred to as a "cytokine storm", is usually considered to be the key pathophysiological response that leads to organ dysfunctions.

Conventional septic shock management includes antibiotics, symptomatic support for organ dysfunction, and surgery to contain the infection source if required. Despite recent advances

in intensive care of systemic infections, 28-day mortality can reach 40% in cases of septic shock. Therefore there is an unmet need to develop extracorporeal devices and membranes to separate endotoxin and bacteria as an adjuvant therapy for septic shock [46].

1.4.1 State-of-the-art technology for endotoxin removal

1.4.1.1 Polymyxin B-immobilized fiber column

One of the most widely used endotoxin removal therapies is polymyxin B-immobilized fiber column (Toraymyxin®; Toray, Tokyo, Japan). The Toraymyxin® cartridge is made of an island-sea type conjugated polystyrene and polypropylene polymer. In this design, polymyxin B, a well-known antibiotic, is fixed on the modified polystyrene to bind to endotoxin (**Figure 1.12**). The binding of polymyxin B to endotoxin is reported to be via ionic and hydrophobic interactions. Toraymyxin® showed promising result in *in vitro* studies and no serious side effects in clinical use of the cartridge [47]. However, the results of clinical trials remain inconclusive regarding the impact of Toraymyxin® on mortality. A few randomized controlled trials (RCTs) comparing polymyxin B adsorption to a standard treatment found conflicting results, suggesting that the positive effect of Toraymyxin® could be greater in particular subgroups of patients [48]. A recent clinical trial in the United States examining the impact of polymyxin B hemoperfusion on mortality in patients with septic shock and endotoxemia indicates no difference in 28-day all-cause mortality after using Toraymyxin®. However, in a post hoc analysis, they evaluated the impact of polymyxin B hemoperfusion use in patients with septic shock and high endotoxin activity measured between 0.6-0.89 (scale from 0 to 1) [49].

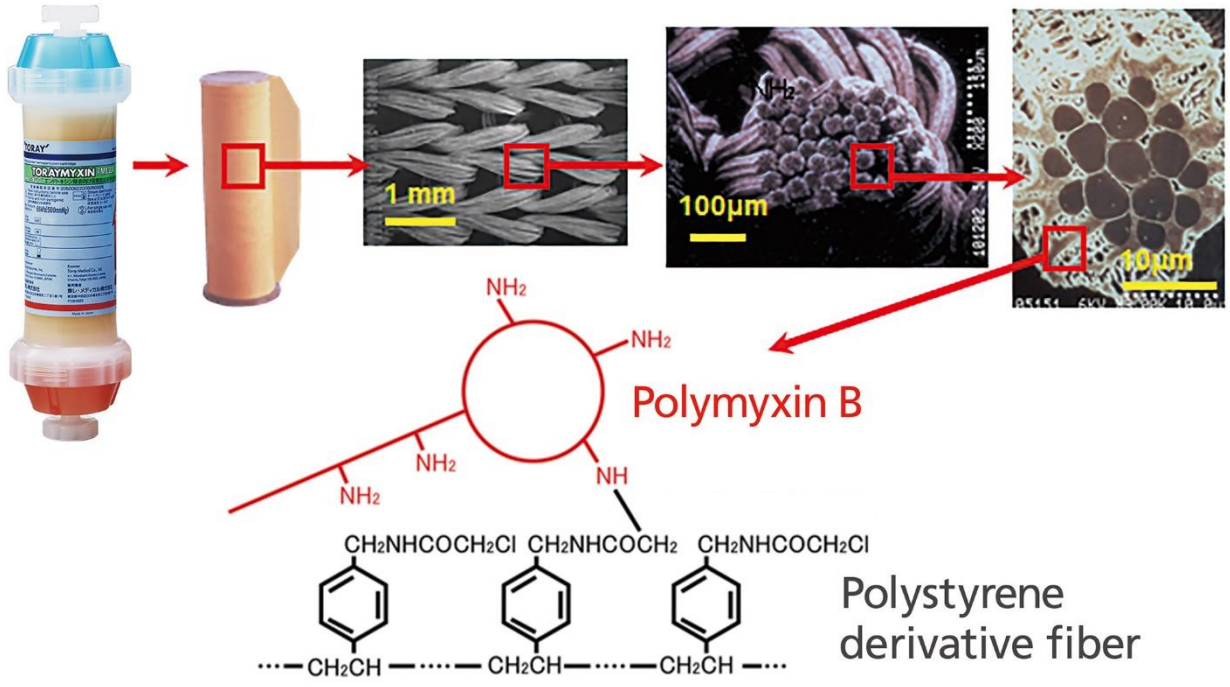

Figure 1.12: Toraymyxin® is an extracorporeal hemoperfusion cartridge designed to remove endotoxin in blood. It is composed of polymyxin B-immobilized polystyrene derivative fibers. Polymyxin B is an antibiotic which is well known to bind endotoxin selectively [47].

1.4.1.2 Alteco® LPS adsorber

The Alteco® LPS adsorber (Alteco® Medical AB; Lund, Sweden) contains discs made of porous polyethylene (PE), with an average pore size of 100 microns. In the pores and on the surface of the discs, the covalently immobilized synthetic cationic peptide captures the negatively charged endotoxin molecules [50].

A few case series in critically ill adults have reported a decrease in endotoxin levels and a hemodynamic improvement after using Alteco® LPS adsorber [50]. However, clinical double-blind RCT in 2019 reached the conclusion that endotoxin removal in septic shock with Alteco® LPS adsorber is safe but shows no benefit compared to placebo [51].

1.4.1.3 oXiris®

The oXiris® hemofilter (Baxter, Global headquarter in USA) was developed to enhance the adsorption properties of the AN69 membrane. AN69 membrane is composed of acrylonitrile and sodium methallylsulfonate. Due to the sulfonate groups, the membrane is negatively charged and is able to adsorb cytokines and toxins via their cationic residues (**Figure 1.13**). The polyethyleneimine (PEI) surface treatment allows for the adsorption of endotoxins. Finally, the heparin graft on the membrane reduces membrane thrombogenicity. This unique design allows for the combination of 4 properties in 1 device: renal support, cytokine removal, endotoxin removal, and local anticoagulant treatment [52].

The oXiris® set is authorized by US Food and Drug Administration (FDA) under an Emergency Use Authorization (EUA) for the treatment of patients 18 years of age or older with confirmed COVID-19 and admittance to the ICU to reduce pro-inflammatory cytokine levels. Zhang *et. al* reported a reduced level of overexpressed cytokines, stabilization of hemodynamic status, and staged improvement of organ function during the treatment of five COVID-19 patients with the oXiris membrane [53]. A clinical study on 16 patients with septic shock showed reduction in circulating endotoxin and cytokine levels after using oXiris® membrane, indicating the potential of this biomedical device as an adjuvant therapy for sepsis [54].

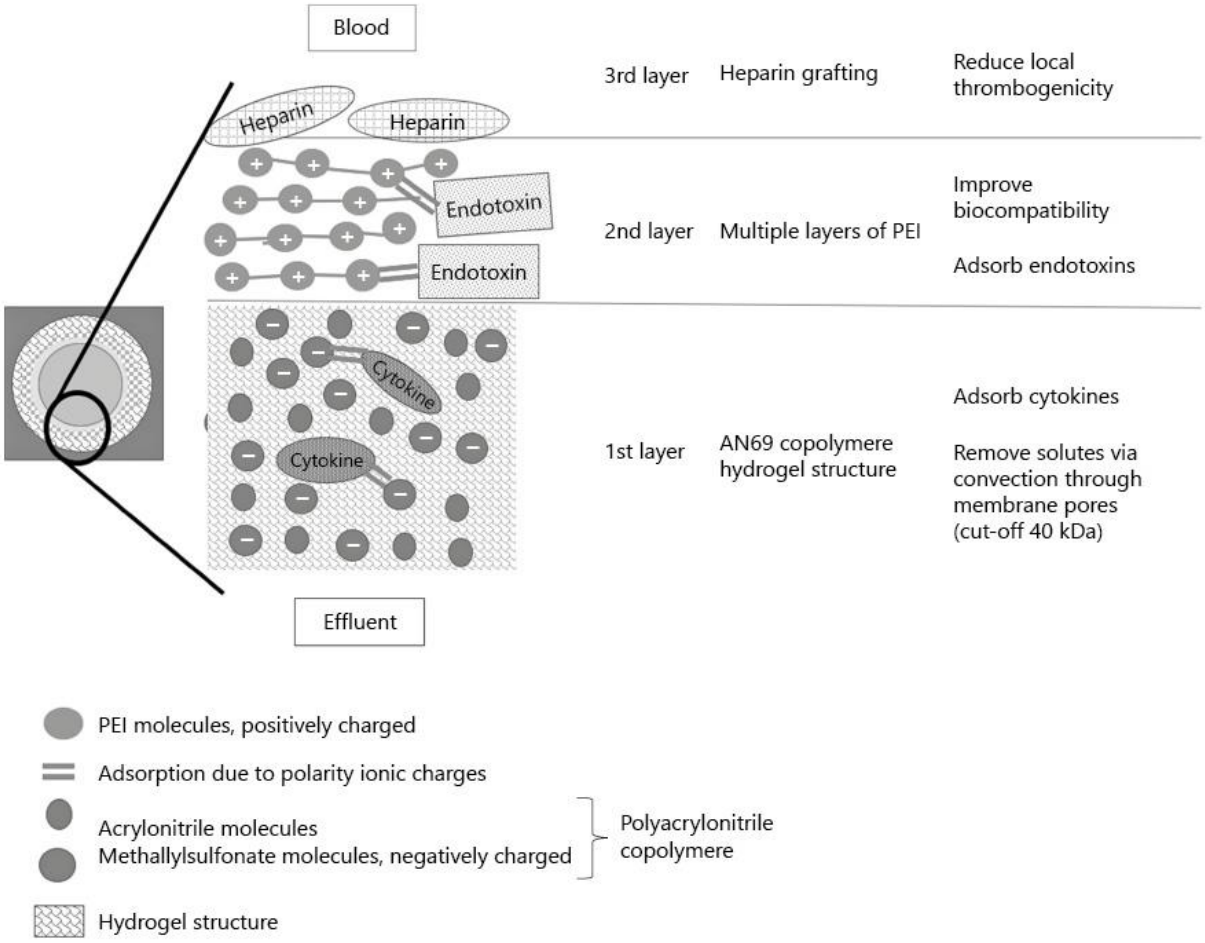

Figure 1.13: The oXiris® membrane set has a three-layer membrane structure. AN69 membrane, Polyethyleneimine (PEI) surface to capture endotoxin and the heparin grafted layer to reduces thrombogenicity [48].

1.4.1.4 Seraph® 100 Microbind®

In late 2019, the European Union licensed Seraph® 100 (ExThera Medical, Martinez, CA, USA) for removal of bacteria from the blood. The Seraph® 100 is a hemoperfusion cartridge containing ultrahigh molecular weight polyethylene beads with end point-attached heparin and is effective in the reduction of pathogens from the bloodstream either as a single agent or as an adjuvant to conventional anti-infective agents. Bacteria, viruses, fungi, and toxins have been

shown to bind to the immobilized heparin on beads in a similar way to the interaction with heparan sulfate that naturally occurs on mammalian cellular surfaces (**Figure 1.14**). This binding is nonreversible and as such, the pathogens are removed from the bloodstream [55]. Notably, *in vitro* studies have demonstrated that methicillin-resistant *S. aureus* (MRSA), methicillin-resistant *Staphylococcus epidermidis*, carbapenem-resistant *Klebsiella pneumoniae*, carbapenem-resistant *E. coli*, *Streptococcus pneumoniae*, *Streptococcus pyogenes*, vancomycin-resistant *Enterococcus faecalis*, *Enterococcus faecium*, *Acinetobacter baumannii*, and *Serratia marcescens* bind to the Seraph hemofilter's adsorption media. Up to 99% pathogen reduction has been observed with a single Seraph® 100 treatment. Reducing the patient's pathogen load in blood lowers the risk of metastatic infection and a dysfunctional host response stemming from the release of a variety of virulence factors, toxins, and cytokines [56]–[59].

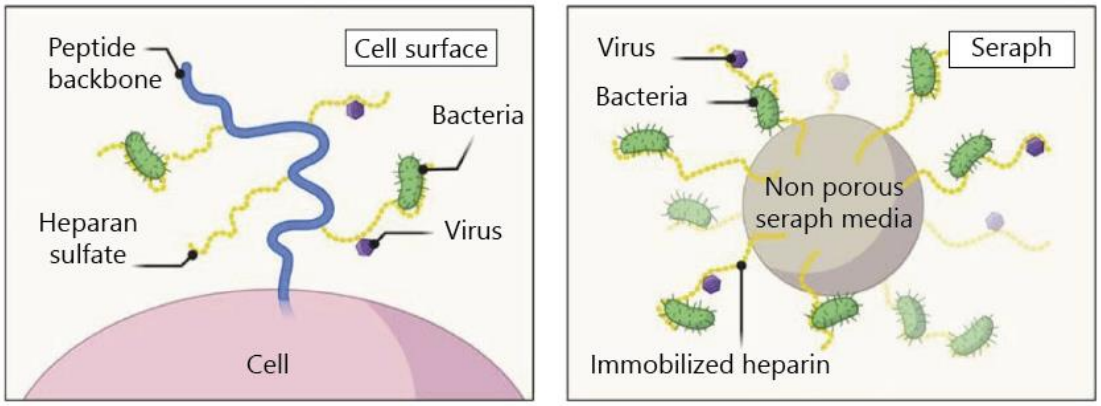

Figure 1.14: Structural similarities between Heparan sulfate on the cell surface and heparin immobilized to polyethylene beads in the Seraph® 100 facilitates adhesion of microorganisms in the blood to the Seraph® 100 [55].

Similar to oXiris, Seraph 100 is granted for emergency use in patients with COVID-19. Published studies have shown high efficacy of the Seraph 100 in clearing SARS-COV-2 from COVID-19 patients [60]. ExThera Medical began its first RCT in 2022 to evaluate the safety and

efficacy of the Seraph® 100 Microbind® Affinity Blood Filter for bacterial sepsis therapy. The study is expected to randomize approximately 60 patients over a 12-month timeframe, with preliminary results expected in early 2023 [59].

The main limitation of sepsis clinical studies are the small cohort sizes. Small cohort studies will be limited in their statistical strength, making it difficult to make conclusive decisions. Large double-blind studies are laborious, and the analyses are expensive and time-consuming. However, further clinical analyses with larger patient populations and data are necessary to make strong conclusions on efficacy of these hemoperfusion cartridges.

Magnetic nanoparticle (MNP) technology has been extensively studied for bacteria and LPS separation, however, they are not yet available for clinical use. Lee et al. developed an approach to clearing bacteria from the bloodstream using MNPs modified with a synthetic ligand, zinc-coordinated bis(dipicolylamine) (bis-Zn-DPA). Magnetic microfluidic devices were used to remove MNPs bound to *E. coli* from whole blood at flowrates as high as 60 mL/h, resulting in almost 100% rapid clearance. Bis-Zn-DPA forms coordination bonds with anionic phospholipids which are present at high density on the outer membrane of gram-negative bacterial cells [61]. In another study, polydopamine (PDA) coating was used as a hemocompatible platform for the functionalization of Fe_3O_4 clusters. Further, a thiol-terminated IBIL, 1-(12-(mercaptododecyl)-3-methylimidazolium bromide (MDMIBr) was designed to decorate the surface of the MNPs via Michael addition or Schiff-base reaction (Fe3O4@PDA-IL), endowing the MNPs with robust bacteria capture capability. The Fe3O4@PDA-IL exhibited good hemocompatibility and performed well in the removal of various species of clinically significant pathogens from human whole blood, including *E. coli*, *P. aeruginosa* and MRSA. The Fe3O4@PDA-IL removes pathogens and bacterial endotoxins via electrostatic and hydrophobic interactions [62]. In an

extracorporeal blood-cleansing device, blood flowing from an infected individual is mixed with MNPs coated with an engineered form of the human opsonin Mannose Binding Lectin linked to an Fc domain (FcMBL) that captures a broad range of pathogens and toxins without activating complement factors or coagulation. MBL is a blood opsonin that captures pathogens such as microorganisms and endotoxin to the spleen for further phagotrophy [63]. Magnets pull the opsonin-bound pathogens and endotoxin from the blood; the cleansed blood is then returned to the individual. This system efficiently removes multiple gram-negative and gram-positive bacteria, fungi, and endotoxin from whole human blood flowing through a single unit at up to 1.25 liters per h *in vitro*. More than 90% of bacteria from blood was cleared in rats infected with *S. aureus* or *E. coli*, resulting in reduced pathogen and immune cell infiltration in multiple organs and decreased inflammatory cytokine levels. In a model of endotoxemia shock, survival rates increased after a 5 h treatment [64].

To remove the requirement for magnetic beads or microfluidics, a more robust, simple, and clinically relevant extracorporeal device is being developed by the same group. They have designed their device to use commercially available polyethersulfone (PES) hollow fibers as a scaffolding with FcMBL attached. This approach leverages the better utility of PES-based cartridges for clinical use and the broad-spectrum pathogen and endotoxin capture capabilities of FcMBL (**Figure 1.15 a-c**). When tested with human whole blood *in vitro*, the FcMBL hemoadsorption filter (FcMBL-HF) produced efficient (90–99%) removal of *E. coli*, *S. aureus*, *Candida albicans* and endotoxin. When tested in rats, extracorporeal therapy with the FcMBL-HF device reduced circulating pathogen and endotoxin levels by more than 99% and prevented pathogen engraftment and inflammatory cell recruitment in the spleen, lung, liver, and kidney when compared to controls (**Figure 1.15 d and e**). Importantly, cleansing of ‘pathogen-associated

molecular patterns' (PAMPs) from the blood of antibiotic-treated animals with the FcMBL-HF device resulted in reduced organ pathogen and endotoxin loads, suppressed inflammatory responses, and resulted in more stable vital signs compared to treatment with antibiotics alone [65].

In addition to the previously described membrane-based materials for microorganism and/or endotoxin removal that have been successfully developed, other products are currently being studied. In one example, Zhao et al. have immobilized l-serine onto a PES electrospun fiber membrane, using PDA as intermediate layer (PES/PDA-Ser). The adsorption kinetics and isothermal adsorption of the PES/PDA-Ser fiber membrane demonstrated an adsorption capacity of 1.28 EU/mg with the equilibrium adsorption time about 1 h. PES/PDA-Ser fiber membrane displayed an endotoxin removal efficiency of 0.85 EU/mg. Hemolysis (0.6%), coagulation, and protein assays showed that the PES/PDA-Ser fiber membrane is hemocompatible and has anti-protein adsorption performance [66]. Endotoxin bonding capacity of polymyxin B has been studied for more than a decade. Peng et al. used the dry-jet wet-spinning process to fabricate fibers containing polymyxin B. In this process, polymyxin B is loaded onto gellan–polylysine polyion complex to prepare the spinning solution. Prepared fibers were then knitted to make a membrane. The tensile strength of the fibers prepared with this method ranged from 1.49 N to −1.58 N. The membrane has LPS adsorption capacity of 2.452 EU/mg from plasma and causes no significant hemolysis or coagulation [67].

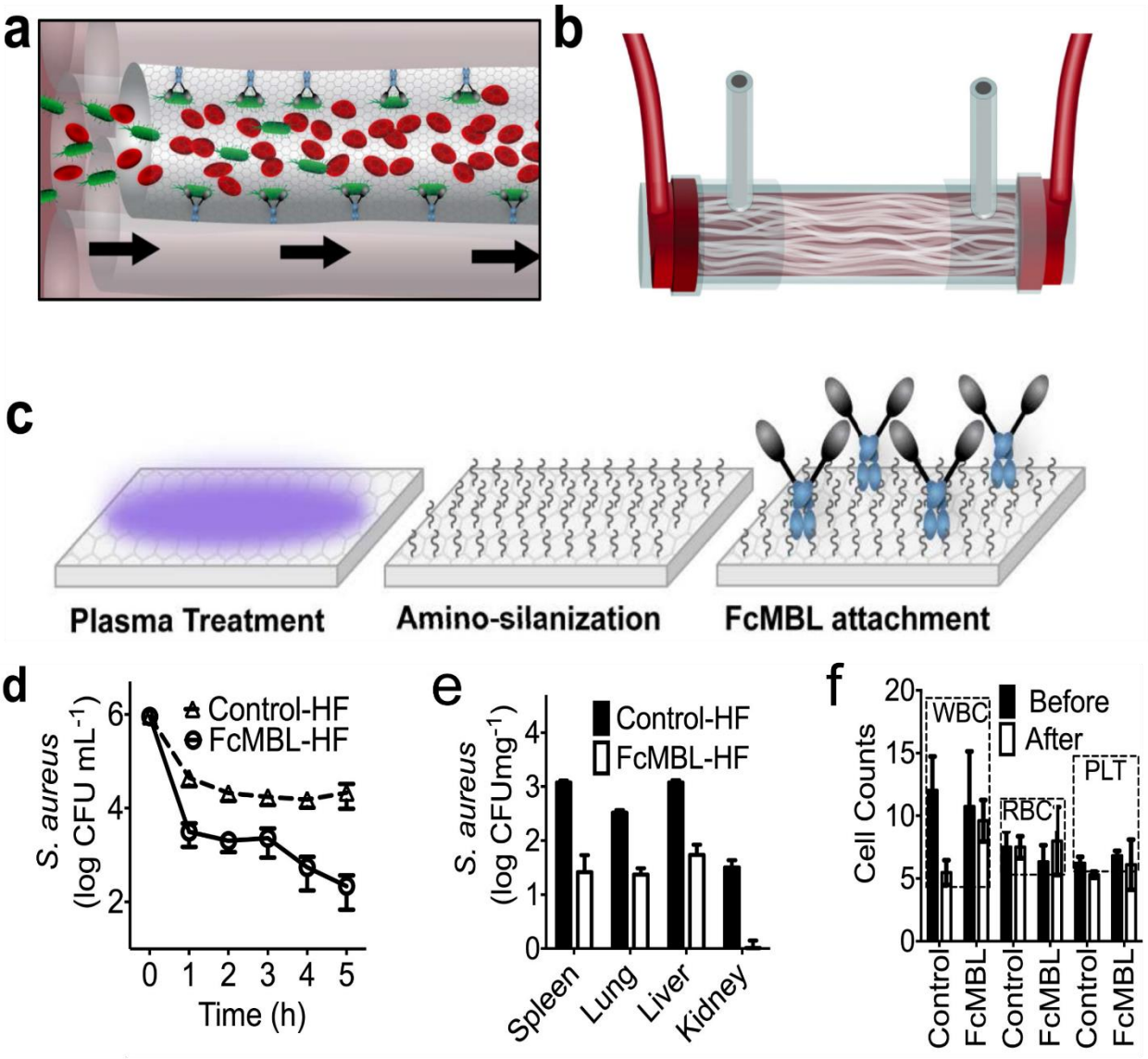

Figure 1.15: (a) Schematic representation of a hollow fiber covalently functionalized with FcMBL which is used to capture pathogens (oval shapes) in blood flowing through the fiber lumen (arrows indicate flow direction). (b) Drawing of a commercially available hemofilter containing many internal hollow fibers that function in parallel. (c) Schematic representation of the procedure for functionalizing hollow fiber surfaces with FcMBL. (d) *S. aureus* concentration in the blood of rats treated with the FcMBL-HF (n = 3) or a control hollow fiber (n = 3) *in vivo*. In less than 3 h, FcMBL-HF treatment resulted in a 1 Log reduction in *S. aureus* concentration compared to treatment with the control device (mean ± s.d., n = 3, $P < 0.05$). (e) Concentration of *S. aureus* in the major organs of rats after treatment compared to the control rats. FcMBL-HF treatment resulted in over 90% reduction in *S. aureus* concentration in these organs compared to the controls (mean ± s.d., n = 3, $P < 0.05$). (f) White blood cell (WBC, $10^3/\mu L$) counts remained in the normal range for both control and treated animals infected with *S. aureus*; however, control rats had lower white blood cell counts compared to the treated animals. Dashed boxes show the normal range (mean ± s.d., n = 3).

Hydrogel has attracted attention as a mediator for endotoxin and bacteria removal due to its biocompatibility. Genipin crosslinked chitosan-kappa-carrageenan composite hydrogels (C-K hydrogels) have been developed to reduce endotoxin level and bacteria burden in septic blood. Chitosan is widely recognized as a cationic polysaccharide that can selectively bind to negatively charged endotoxin by electrostatic interaction. The C-K hydrogels were competent to eliminate 63.3% of endotoxin in septic blood with a maximum adsorption capacity of 95.0 EU/g during a 3 h simulative hemoperfusion procedure. Bacteria cleansing experiments further demonstrated that the C-K hydrogels effectively decreased 46.0% of *E. coli* and 68.7% of *S. aureus* load, respectively. C-K hydrogels were nonhemolytic and noncytotoxic and the outer carrageenan shells were able to significantly attenuate non-specific plasma protein adsorption, complement activation, contact activation, and platelet activation of the C-K hydrogels compared to raw crosslinked chitosan hydrogel [68].

1.4.2 Melanin in endotoxin removal

In a typical year in the United States, more than 1.7 million adults develop sepsis and 1 in 3 patients who die in a hospital have sepsis [69]. Considering the high mortality rate and prevalence of sepsis, there is a large unmet need to study and develop materials for clearing endotoxin and bacteria. Due to the limitations of hemofiltration cartridges mentioned above, there are further approaches that could be employed to take advantage of natural biopolymers such as melanin while also providing effective endotoxin removal. Multivalent cations such as Zn^{2+}, Mg^{2+}, Cu^{2+} and $Fe^{2+/3+}$ bind to catechol groups in melanin via coordination bonding. Melanin, as a biocompatible biopolymer, can bind to zinc ions via catechol group oxidation. Zinc is the second most abundant trace element (after iron) essential for all living organisms [70]. Previous studies show that zinc

compounds can be used as inhibitors of phosphopeptide and protein reactions as well as selective sensing of biologically important phosphate oxyanions [71]. In living organisms, zinc is redox-inert and has only one valence state: Zn^{2+}. The d-block orbital cation Zn^{2+} differs from s-block orbital cations such as Ca^{2+} or Mg^{2+} by demonstrating significantly higher affinity for ligands, preference for the donor atoms of ligands, and coordination dynamics [72]. Therefore, zinc loaded melanin can selectively bond to negatively charged phosphate groups in the endotoxin structure.

In Chapter 3, I leverage zinc loaded melanin for endotoxin and bacteria removal (**Figure 1.16**). I load zinc ions in melanin structure and confirm successful loading using XPS and Raman spectroscopy. I find that zinc loaded melanin can selectively bond to gram negative bacteria and endotoxin, facilitating their separation from blood. Additionally, I find that zinc loaded melanin causes minimal hemolysis and coagulation, indicating blood biocompatibility of the material.

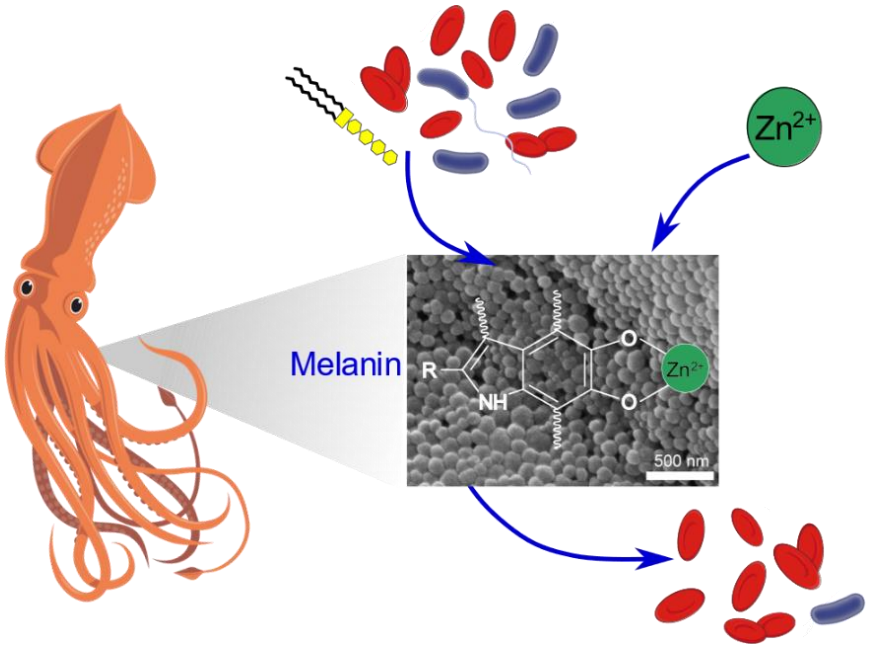

Figure 1.16: Melanin zinc complex as a biocompatible agent for clearing bacteremia.

1.5 References

[1] D. Singh, J. Kumar, and A. Kumar, “Isolation of pyomelanin from bacteria and evidences showing its synthesis by 4-hydroxyphenylpyruvate dioxygenase enzyme encoded by hppD gene,” *Int. J. Biol. Macromol.*, vol. 119, pp. 864–873, Nov. 2018, doi: 10.1016/j.ijbiomac.2018.08.003.

[2] M. Ye, G. Guo, Y. Lu, S. Song, H. Wang, and L. Yang, “Purification, structure and anti-radiation activity of melanin from Lachnum YM404,” *Int. J. Biol. Macromol.*, vol. 63, pp. 170–176, Feb. 2014, doi: 10.1016/j.ijbiomac.2013.10.046.

[3] A. R. Katritzky, N. G. Akhmedov, S. N. Denisenko, and O. V. Denisko, “^{1} H NMR Spectroscopic Characterization of Solutions of *Sepia* Melanin, *Sepia* Melanin Free Acid and Human Hair Melanin,” *PIGMENT CELL Res.*, vol. 15, no. 2, pp. 93–97, Apr. 2002, doi: 10.1034/j.1600-0749.2002.1o062.x.

[4] A. A. R. Watt, J. P. Bothma, and P. Meredith, “The supramolecular structure of melanin,” *Soft Matter*, vol. 5, no. 19, p. 3754, 2009, doi: 10.1039/b902507c.

[5] F. A. Zucca *et al.*, “Neuromelanin of the Human Substantia Nigra: An Update,” *Neurotox. Res.*, vol. 25, no. 1, pp. 13–23, Jan. 2014, doi: 10.1007/s12640-013-9435-y.

[6] Y. Liu *et al.*, “Comparison of Structural and Chemical Properties of Black and Red Human Hair Melanosomes¶,” *Photochem. Photobiol.*, vol. 81, no. 1, p. 135, 2005, doi: 10.1562/2004-08-03-RA-259.1.

[7] P. Meredith, B. J. Powell, J. Riesz, S. P. Nighswander-Rempel, M. R. Pederson, and E. G. Moore, “Towards structure–property–function relationships for eumelanin,” *Soft Matter*, vol. 2, no. 1, pp. 37–44, 2006, doi: 10.1039/B511922G.

[8] L. Panzella *et al.*, “Atypical Structural and π-Electron Features of a Melanin Polymer That Lead to Superior Free-Radical-Scavenging Properties,” *Angew. Chem. Int. Ed.*, vol. 52, no. 48, pp. 12684–12687, Nov. 2013, doi: 10.1002/anie.201305747.

[9] Z. Ye *et al.*, “Structure, molecular modification and anti-tumor activity of melanin from Lachnum singerianum,” *Process Biochem.*, vol. 76, pp. 203–212, Jan. 2019, doi: 10.1016/j.procbio.2018.09.007.

[10] E. Geib *et al.*, “A Non-canonical Melanin Biosynthesis Pathway Protects Aspergillus terreus Conidia from Environmental Stress,” *Cell Chem. Biol.*, vol. 23, no. 5, pp. 587–597, May 2016, doi: 10.1016/j.chembiol.2016.03.014.

[11] P. Zhao, Z. Lu, M. R. Strand, and H. Jiang, “Antiviral, anti-parasitic, and cytotoxic effects of 5,6-dihydroxyindole (DHI), a reactive compound generated by phenoloxidase during insect immune response,” *Insect Biochem. Mol. Biol.*, vol. 41, no. 9, pp. 645–652, Sep. 2011, doi: 10.1016/j.ibmb.2011.04.006.

[12] S. Roy and J.-W. Rhim, “Agar-based antioxidant composite films incorporated with melanin nanoparticles,” *Food Hydrocoll.*, vol. 94, pp. 391–398, Sep. 2019, doi: 10.1016/j.foodhyd.2019.03.038.

[13] M. d’Ischia *et al.*, “Melanins and melanogenesis: methods, standards, protocols,” *Pigment Cell Melanoma Res.*, vol. 26, no. 5, pp. 616–633, Sep. 2013, doi: 10.1111/pcmr.12121.

[14] N. Correa *et al.*, “Differential Antifungal Activity of Human and Cryptococcal Melanins with Structural Discrepancies,” *Front. Microbiol.*, vol. 8, p. 1292, Jul. 2017, doi: 10.3389/fmicb.2017.01292.

[15] M. d’Ischia, A. Napolitano, A. Pezzella, P. Meredith, and T. Sarna, “Chemical and Structural Diversity in Eumelanins: Unexplored Bio-Optoelectronic Materials,” *Angew. Chem. Int. Ed.*, vol. 48, no. 22, pp. 3914–3921, May 2009, doi: 10.1002/anie.200803786.

[16] F. Solano, “Melanins: Skin Pigments and Much More—Types, Structural Models, Biological Functions, and Formation Routes,” *New J. Sci.*, vol. 2014, pp. 1–28, Mar. 2014, doi: 10.1155/2014/498276.

[17] S. Felz, S. Al-Zuhairy, O. A. Aarstad, M. C. M. van Loosdrecht, and Y. M. Lin, “Extraction of Structural Extracellular Polymeric Substances from Aerobic Granular Sludge,” *J. Vis. Exp.*, no. 115, p. 54534, Sep. 2016, doi: 10.3791/54534.

[18] S. Singh *et al.*, “Microbial melanin: Recent advances in biosynthesis, extraction, characterization, and applications,” *Biotechnol. Adv.*, vol. 53, p. 107773, Dec. 2021, doi: 10.1016/j.biotechadv.2021.107773.

[19] I. Singh, G. Dhawan, S. Gupta, and P. Kumar, “Recent Advances in a Polydopamine-Mediated Antimicrobial Adhesion System,” *Front. Microbiol.*, vol. 11, p. 607099, Jan. 2021, doi: 10.3389/fmicb.2020.607099.

[20] Z. Jin *et al.*, “Flexible Polydopamine Bioelectronics,” *Adv. Funct. Mater.*, vol. 31, no. 30, p. 2103391, Jul. 2021, doi: 10.1002/adfm.202103391.

[21] J. Li, S. Yuan, J. Wang, J. Zhu, J. Shen, and B. Van der Bruggen, “Mussel-inspired modification of ion exchange membrane for monovalent separation,” *J. Membr. Sci.*, vol. 553, pp. 139–150, May 2018, doi: 10.1016/j.memsci.2018.02.046.

[22] H. Qian *et al.*, “Mussel-inspired superhydrophilic surface with enhanced antimicrobial properties under immersed and atmospheric conditions,” *Appl. Surf. Sci.*, vol. 465, pp. 267–278, Jan. 2019, doi: 10.1016/j.apsusc.2018.09.173.

[23] Z. Tian, W. Hwang, and Y. J. Kim, “Mechanistic understanding of monovalent cation transport in eumelanin pigments,” *J. Mater. Chem. B*, vol. 7, no. 41, pp. 6355–6361, 2019, doi: 10.1039/C9TB01211G.

[24] Y. J. Kim, W. Wu, S.-E. Chun, J. F. Whitacre, and C. J. Bettinger, “Biologically derived melanin electrodes in aqueous sodium-ion energy storage devices,” *Proc. Natl. Acad. Sci.*, vol. 110, no. 52, pp. 20912–20917, Dec. 2013, doi: 10.1073/pnas.1314345110.

[25] T. Rahmani Eliato *et al.*, “Melanin pigments extracted from horsehair as antibacterial agents,” *J. Mater. Chem. B*, vol. 9, no. 6, pp. 1536–1545, 2021, doi: 10.1039/D0TB02475A.

[26] F. Solano, “Melanin and Melanin-Related Polymers as Materials with Biomedical and Biotechnological Applications—Cuttlefish Ink and Mussel Foot Proteins as Inspired Biomolecules,” *Int. J. Mol. Sci.*, vol. 18, no. 7, p. 1561, Jul. 2017, doi: 10.3390/ijms18071561.

[27] Y. J. Kim *et al.*, “Evidence of Porphyrin-Like Structures in Natural Melanin Pigments Using Electrochemical Fingerprinting,” *Adv. Mater.*, vol. 28, no. 16, pp. 3173–3180, Apr. 2016, doi: 10.1002/adma.201504650.

[28] Z. Wang *et al.*, “Mussel-Inspired Surface Engineering for Water-Remediation Materials,” *Matter*, vol. 1, no. 1, pp. 115–155, Jul. 2019, doi: 10.1016/j.matt.2019.05.002.

[29] H. Meng *et al.*, “Biomimetic recyclable microgels for on-demand generation of hydrogen peroxide and antipathogenic application,” *Acta Biomater.*, vol. 83, pp. 109–118, Jan. 2019, doi: 10.1016/j.actbio.2018.10.037.

[30] G. Zhang, J. Lv, and F. Yang, “Optimized anti-biofouling performance of bactericides/cellulose nanocrystals composites modified PVDF ultrafiltration membrane for micro-polluted source water purification,” *Water Sci. Technol.*, vol. 79, no. 8, pp. 1437–1446, Apr. 2019, doi: 10.2166/wst.2019.137.

[31] L. Wang, C. Hu, and L. Shao, “The antimicrobial activity of nanoparticles: present situation and prospects for the future,” *Int. J. Nanomedicine*, vol. Volume 12, pp. 1227–1249, Feb. 2017, doi: 10.2147/IJN.S121956.

[32] A. Khezerlou, M. Alizadeh-Sani, M. Azizi-Lalabadi, and A. Ehsani, “Nanoparticles and their antimicrobial properties against pathogens including bacteria, fungi, parasites and viruses,” *Microb. Pathog.*, vol. 123, pp. 505–526, Oct. 2018, doi: 10.1016/j.micpath.2018.08.008.

[33] N. S. Leyland, J. Podporska-Carroll, J. Browne, S. J. Hinder, B. Quilty, and S. C. Pillai, “Highly Efficient F, Cu doped TiO2 anti-bacterial visible light active photocatalytic coatings to combat hospital-acquired infections,” *Sci. Rep.*, vol. 6, no. 1, p. 24770, Jul. 2016, doi: 10.1038/srep24770.

[34] J. Podporska-Carroll *et al.*, “Antibacterial properties of F-doped ZnO visible light photocatalyst,” *J. Hazard. Mater.*, vol. 324, pp. 39–47, Feb. 2017, doi: 10.1016/j.jhazmat.2015.12.038.

[35] H. Qian *et al.*, “Mussel-inspired superhydrophilic surface with enhanced antimicrobial properties under immersed and atmospheric conditions,” *Appl. Surf. Sci.*, vol. 465, pp. 267–278, Jan. 2019, doi: 10.1016/j.apsusc.2018.09.173.

[36] A. Nastulyavichus *et al.*, “Antibacterial coatings of Se and Si nanoparticles,” *Appl. Surf. Sci.*, vol. 469, pp. 220–225, Mar. 2019, doi: 10.1016/j.apsusc.2018.11.011.

[37] H. Kim, J. H. Jang, S. C. Kim, and J. H. Cho, “Development of a novel hybrid antimicrobial peptide for targeted killing of Pseudomonas aeruginosa,” *Eur. J. Med. Chem.*, vol. 185, p. 111814, Jan. 2020, doi: 10.1016/j.ejmech.2019.111814.

[38] Z. Zhang *et al.*, “Iron Magnetic Nanoparticle-Induced ROS Generation from Catechol-Containing Microgel for Environmental and Biomedical Applications,” *ACS Appl. Mater. Interfaces*, vol. 12, no. 19, pp. 21210–21220, May 2020, doi: 10.1021/acsami.9b19726.

[39] M. Fuentes *et al.*, “Actividad antifúngica de melanina en cepas clínicas de Candida spp,” *Rev. Chil. Infectol.*, vol. 31, no. 1, pp. 28–33, Feb. 2014, doi: 10.4067/S0716-10182014000100004.

[40] J. D. Nosanchuk and A. Casadevall, “Impact of Melanin on Microbial Virulence and Clinical Resistance to Antimicrobial Compounds,” *Antimicrob. Agents Chemother.*, vol. 50, no. 11, pp. 3519–3528, Nov. 2006, doi: 10.1128/AAC.00545-06.

[41] P. Sharma, T. A. Singh, B. Bharat, S. Bhasin, and H. A. Modi, “Approach towards different fermentative techniques for the production of bioactive actinobacterial melanin,” *Beni-Suef Univ. J. Basic Appl. Sci.*, vol. 7, no. 4, pp. 695–700, Dec. 2018, doi: 10.1016/j.bjbas.2018.08.002.

[42] M. F. Sosa, P. Sobrero, C. Valverde, and B. Agaras, “A black-pigmented pseudomonad isolate with antibacterial activity against phyllospheric pathogens,” *Rhizosphere*, vol. 15, p. 100207, Sep. 2020, doi: 10.1016/j.rhisph.2020.100207.

[43] L. Wang, Y. Li, and Y. Li, “Metal ions driven production, characterization and bioactivity of extracellular melanin from Streptomyces sp. ZL-24,” *Int. J. Biol. Macromol.*, vol. 123, pp. 521–530, Feb. 2019, doi: 10.1016/j.ijbiomac.2018.11.061.

[44] C. Xu, J. Li, L. Yang, F. Shi, L. Yang, and M. Ye, “Antibacterial activity and a membrane damage mechanism of Lachnum YM30 melanin against Vibrio parahaemolyticus and Staphylococcus aureus,” *Food Control*, vol. 73, pp. 1445–1451, Mar. 2017, doi: 10.1016/j.foodcont.2016.10.048.

[45] V. Ghadge *et al.*, “Natural Melanin Produced by the Endophytic *Bacillus subtilis* 4NP-BL Associated with the Halophyte *Salicornia brachiata*,” *J. Agric. Food Chem.*, vol. 68, no. 25, pp. 6854–6863, Jun. 2020, doi: 10.1021/acs.jafc.0c01997.

[46] L. Zhang, Y. Feng, and P. Fu, “Blood purification for sepsis: an overview,” *Precis. Clin. Med.*, vol. 4, no. 1, pp. 45–55, Apr. 2021, doi: 10.1093/pcmedi/pbab005.

[47] H. Shoji, “Extracorporeal Endotoxin Removal For The Treatment of Sepsis:Endotoxin Adsorption Cartridge (Toraymyxin),” *Ther. Apher. Dial.*, vol. 7, no. 1, pp. 108–114, Feb. 2003, doi: 10.1046/j.1526-0968.2003.00005.x.

[48] C. Monard, T. Rimmelé, and C. Ronco, “Extracorporeal Blood Purification Therapies for Sepsis,” *Blood Purif.*, vol. 47, no. Suppl. 3, pp. 2–15, 2019, doi: 10.1159/000499520.

[49] D. J. Klein, D. Foster, P. M. Walker, S. M. Bagshaw, H. Mekonnen, and M. Antonelli, “Polymyxin B hemoperfusion in endotoxemic septic shock patients without extreme

endotoxemia: a post hoc analysis of the EUPHRATES trial," *Intensive Care Med.*, vol. 44, no. 12, pp. 2205–2212, Dec. 2018, doi: 10.1007/s00134-018-5463-7.

[50] Alteco Medical AB, "Endotoxin removal," *Alteco Medical AB*, Mar. 28, 2022. https://altecomed.com/endotoxin-removal/ (accessed Mar. 28, 2022).

[51] M. Lipcsey *et al.*, "Endotoxin Removal in Septic Shock with the Alteco LPS Adsorber Was Safe But Showed no Benefit Compared to Placebo in the Double-Blind Randomized Controlled Trial—the Asset Study," *Shock*, vol. 54, no. 2, pp. 224–231, Aug. 2020, doi: 10.1097/SHK.0000000000001503.

[52] Baxter, "Oxiris for Critical Care," *Baxter*, Mar. 28, 2022. https://www.baxter.com/healthcare-professionals/critical-care/oxiris-critical-care (accessed Mar. 28, 2022).

[53] H. Zhang, G. Zhu, L. Yan, Y. Lu, Q. Fang, and F. Shao, "The absorbing filter Oxiris in severe coronavirus disease 2019 patients: A case series," *Artif. Organs*, vol. 44, no. 12, pp. 1296–1302, Dec. 2020, doi: 10.1111/aor.13786.

[54] M. E. Broman, F. Hansson, J.-L. Vincent, and M. Bodelsson, "Endotoxin and cytokine reducing properties of the oXiris membrane in patients with septic shock: A randomized crossover double-blind study," *PLOS ONE*, vol. 14, no. 8, p. e0220444, Aug. 2019, doi: 10.1371/journal.pone.0220444.

[55] M.-T. Seffer, D. Cottam, L. G. Forni, and J. T. Kielstein, "Heparin 2.0: A New Approach to the Infection Crisis," *Blood Purif.*, vol. 50, no. 1, pp. 28–34, 2021, doi: 10.1159/000508647.

[56] M.-T. Seffer, G. Eden, S. Engelmann, and J. T. Kielstein, "Elimination of *Staphylococcus aureus* from the bloodstream using a novel biomimetic sorbent haemoperfusion device," *BMJ Case Rep.*, vol. 13, no. 8, p. e235262, Aug. 2020, doi: 10.1136/bcr-2020-235262.

[57] K. McCrea, R. Ward, and S. P. LaRosa, "Removal of Carbapenem-Resistant Enterobacteriaceae (CRE) from Blood by Heparin-Functional Hemoperfusion Media," *PLoS ONE*, vol. 9, no. 12, p. e114242, Dec. 2014, doi: 10.1371/journal.pone.0114242.

[58] I. Mattsby-Baltzer, T. Bergstrom, K. McCrea, R. Ward, L. Adolfsson, and O. Larm, "Affinity Apheresis for Treatment of Bacteremia Caused by Staphylococcus aureus and/or Methicillin-Resistant S. aureus (MRSA)," *J. Microbiol. Biotechnol.*, vol. 21, no. 6, pp. 659–664, Jun. 2011, doi: 10.4014/jmb.1102.02016.

[59] ExThere Medical, “Revolutionary COVID-19 Pathogen Adsorption | ExThera Medical.” https://extheramedical.com/ (accessed Apr. 08, 2022).

[60] J. J. Schmidt *et al.*, “Interim analysis of the COSA (COVID-19 patients treated with the Seraph® 100 Microbind® Affinity filter) registry,” *Nephrol. Dial. Transplant.*, vol. 37, no. 4, pp. 673–680, Mar. 2022, doi: 10.1093/ndt/gfab347.

[61] J.-J. Lee *et al.*, “Synthetic Ligand-Coated Magnetic Nanoparticles for Microfluidic Bacterial Separation from Blood,” *Nano Lett.*, vol. 14, no. 1, pp. 1–5, Jan. 2014, doi: 10.1021/nl3047305.

[62] Z. Shi *et al.*, “Hemocompatible magnetic particles with broad-spectrum bacteria capture capability for blood purification,” *J. Colloid Interface Sci.*, vol. 576, pp. 1–9, Sep. 2020, doi: 10.1016/j.jcis.2020.04.115.

[63] Q. Yang *et al.*, “Advances in the Development of Biomaterials for Endotoxin Adsorption in Sepsis,” *Front. Bioeng. Biotechnol.*, vol. 9, p. 699418, 2021, doi: 10.3389/fbioe.2021.699418.

[64] J. H. Kang *et al.*, “An extracorporeal blood-cleansing device for sepsis therapy,” *Nat. Med.*, vol. 20, no. 10, pp. 1211–1216, Oct. 2014, doi: 10.1038/nm.3640.

[65] T. F. Didar *et al.*, “Improved treatment of systemic blood infections using antibiotics with extracorporeal opsonin hemoadsorption,” *Biomaterials*, vol. 67, pp. 382–392, Oct. 2015, doi: 10.1016/j.biomaterials.2015.07.046.

[66] K. Zhao *et al.*, “Polydopamine-assisted immobilization of L-serine onto PES electrospun fiber membrane for effective endotoxin removal,” *Compos. Commun.*, vol. 20, p. 100365, Aug. 2020, doi: 10.1016/j.coco.2020.100365.

[67] X. Peng, X. Yan, L. Zhu, Y. Gu, Z. Sun, and X. Zhan, “Preparation of polymyxin B-loaded gellan–polylysine polyion complex fibers with high affinity to endotoxin,” *Int. J. Biol. Macromol.*, vol. 160, pp. 703–710, Oct. 2020, doi: 10.1016/j.ijbiomac.2020.05.263.

[68] Y. Li *et al.*, “Anticoagulant chitosan-kappa-carrageenan composite hydrogel sorbent for simultaneous endotoxin and bacteria cleansing in septic blood,” *Carbohydr. Polym.*, vol. 243, p. 116470, Sep. 2020, doi: 10.1016/j.carbpol.2020.116470.

[69] CDC, “Sepsis is a medical emergency. ACT FAST.,” *Centers for Disease Control and Prevention*, Aug. 17, 2021. https://www.cdc.gov/sepsis/what-is-sepsis.html (accessed Mar. 28, 2022).

[70] T. Kambe, T. Tsuji, A. Hashimoto, and N. Itsumura, “The Physiological, Biochemical, and Molecular Roles of Zinc Transporters in Zinc Homeostasis and Metabolism,” *Physiol. Rev.*, vol. 95, no. 3, pp. 749–784, Jul. 2015, doi: 10.1152/physrev.00035.2014.

[71] H. T. Ngo, X. Liu, and K. A. Jolliffe, “Anion recognition and sensing with Zn(ii)–dipicolylamine complexes,” *Chem. Soc. Rev.*, vol. 41, no. 14, p. 4928, 2012, doi: 10.1039/c2cs35087d.

[72] A. Krężel and W. Maret, “The biological inorganic chemistry of zinc ions,” *Arch. Biochem. Biophys.*, vol. 611, pp. 3–19, Dec. 2016, doi: 10.1016/j.abb.2016.04.010.

[73] L. Hong, Y. Liu, and J.D. Simon, “Binding of metal ions to melanin and their effects on the aerobic reactivity,” *Photochemistry and Photobiology*, vol. 80, pp. 477-481, Jul. 2004, doi: 10.1562/0031-8655(2004)080<0477:BOMITM>2.0.CO;2.

[74] L. Hong and J.D. Simon, “Insight into the Binding of Divalent Cations to Sepia Eumelanin from IR Absorption Spectroscopy,” *Photochemistry and Photobiology*, vol. 82, pp. 1265-1269, May 2006, 10.1562/2006-02-23-RA-809.

CHAPTER 2
Melanin pigments extracted from horsehair as antibacterial agents

2.1 Introduction

Bacterial adherence and subsequent proliferation on solid surfaces are ongoing challenges in a variety of areas including daily consumables, industrial processes, and biomedical devices [1]. The most common cause of biomedical implant failure is bacterial infection, which is exacerbated due to biofilm formation [2]–[4]. Between 7-8 % of hernia repair surgical procedures result in infection and bacteria formation [5]. Biofilm formation also leads to major challenges in wastewater treatment processes that use membranes [6]. Membrane filtration is one of the most common approaches to convert effluents into water with acceptable level of impact to the environment by removing the ions and microorganisms [7]. Such filtration techniques are affordable and cost-effective, however long-term use of a filter can promote biofilm formation which can consequently reduce its efficacy, and lifetime with increasing operational costs [8], [9]. Hence, development of effective strategies to minimize bacterial growth and prevent biofilm formation in these settings is critical.

Metal nanoparticles such as copper (Cu), titanium (Ti), silver (Ag), zinc (Zn), selenium (Se) and silicone (Si) have been studied for their antibacterial properties [10]–[13]. Oxidative stress generated by reactive oxygen species (ROS) and metal ion penetration into the bacteria are two main mechanisms that damage bacteria cells and lead to cell death [14], [15]. However, there are many potential challenges associated with the depletion of metal ions from this class of metallic nanomaterials. Surface coating with polymers can be another approach to prevent biofouling and

minimize bacterial growth on surfaces. Hydrophilic polymers such as polyethylene glycol and polyglycerol, or zwitterionic polymers such as 2-methacryloyloxyethyl phosphorylcholine and poly(sulfobetaine methacrylate) have been widely used to form a hydration layer on the surface to prevent bacterial adhesion and biofouling [16]–[19]. This hydration layer near the surface acts as a physical barrier and prevents direct contact between biomolecules and the surface. However, disordered disruption of polymeric surfaces in the complex media can result in potential challenges that shortens the longevity [20]. Moreover, the disruption of biofilms using antibacterial agents requires concentrations that are 10-1000X higher than those that target isolated bacterial colonies [21], [22]. Both surface properties and surface area are two major factors that dictate biofilm formation [23]. The antibacterial agents that are biologically-derived, bioinert, scalable, and cost effective are therefore intrinsically advantageous.

As a subset of melanins, eumelanins (hereafter called melanins) are a broad class of biopigments that can be found in the skin, hair, iris of the eye, and neurosensorial tissues [24]–[26]. Melanins are largely composed of two subunits of 5,6-dihydroxyindole (DHI) and 5,6-dihydroxyindole-2-carboxylic acid (DHICA) [27]. These subunits are randomly stacked into planar macromolecular structures via π-π interactions to form homogeneous microstructures [28], [29]. Biological functions of melanins vary depending on their location in the physiological system however, the major role of melanins is to protect cells from radiation damage [30]. Melanins contain diverse chemical functional groups such as redox-active catechols, pendant carboxylic acids, and aromatic amines, which allow conjugate bonding with a variety of cations including protons or metallic cations [31], [32]. Utility of these chemical features have allowed melanins to be used in many applications such as surgical meshes, biomedical imaging, cancer treating

materials, functional coatings for tissue engineering, and aqueous charge storage devices [33]–[36].

Furthermore, recent studies have shown that catechol-embedded thin film composites can produce ROS by electrochemical insertion of ions and inhibit bacterial growth [37]–[39]. Antimicrobial activities based on catechol chemistry have been reported from dopamine methacrylamide as well as melanins that are naturally sourced from fungi or bacteria [40]–[43]. The unique structure of naturally-occurring melanins and the redox activity via catechol functional groups suggest that they can serve as biocompatible antibacterial agents. Herein we report the extraction of melanin pigments from *Equus ferus* (horse) hair and investigate their antibacterial activity. Structures in micro- and meso-scale are examined by electron microscope and x-ray scattering techniques and the chemical functionalities are evaluated by spectroscopic tools. These structural and chemical analysis will assist to understand the structure-chemistry-property relationship of the naturally occurring biopigment as an antibacterial agent.

2.2 Materials and methods

2.2.1 Materials

Hydrochloric acid (HCl, ACS reagent, 37 %), acetone, ethanol, Synthetic melanin (SynMel) in analytical grade were purchased from Sigma-Aldrich (St. Louis, MO USA). *E. ferus* hair was collected from the Equine Facilities at the University of New Hampshire (Durham, NH USA). Amplex™ Red hydrogen peroxide/peroxidase assay kit was obtained from Invitrogen (Waltham, MA USA).

2.2.2 Extraction of melanin from *E. ferus* hair

Melanin pigments extracted from black *E. ferus* hair were prepared as previously described using acid hydrolysis.[44] Initially, the hair was washed thoroughly by acetone and ethanol (1:2 vol %) three times. Approximately 4 g of washed hair was vigorously stirred in a solution of 1 % HCl (V = 80 ml) to remove the water-soluble components. They were then mixed with 32 % HCl (V = 160 ml) followed by heating to 100 ^{o}C for 3 h (**Figure 2.1**). The solution was centrifuged at 3500 rpm for 5 min, and the precipitates were washed with double-distilled water (ddH_2O) four times. After discarding the supernatant, the sediment was dried in a vacuum oven overnight. Extracted melanin was kept in a closed container in darkness at ambient conditions until further processing.

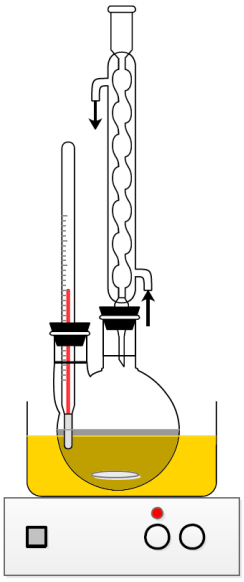

Figure 2.1: Experimental setup for melanin extraction.

2.2.3 Spectroscopic and microscopic characterization of melanins

As-prepared *Equus*Mel powder was fixed on Al stubs with double-sided carbon adhesive tape followed by Pt sputter coating. Images were taken using a scanning electron microscope (SEM, Lyra3 GMU FIB, Tescan, Brno, Czechia).

Small and wide-angle X-ray scattering (SAXS/WAXS) were performed using the *in situ* SAXS/WAXS Xeuss System (Xenocs, Grenoble, France) with a CuKα X-ray source (λ = 1.5418 Å, GeniX3D Cu ULD, Xenocs, SA, France) at 23°C. The scattering data were collected on a Pilatus (DECTRIS, Switzerland) over 6 frames with a 10 minutes acquisition time for each frame. The sample to detector distance (SDD) for SAXS/WAXS was 2464 mm and 365 mm, respectively, after the calibration using silver behenate (AgBe). Melanin in ethanol solution was suspended and dispersed using ultrasonic bath and dried in vacuum oven followed by placing in two Mylar films for SAXS/WAXS performance. The data of two Mylar films in an empty cell were collected as

background. Six frames (600 s frame^{-1}) were collected for each sample, then normalized by the number of frames and circular averaged to obtain an intensity-wave vector (q) after background subtraction. Scattering images were analyzed using Igor Pro software (ver. 6.37) with the Irena package to obtain circular averaged 1D plots of intensity vs. scattering wave vector q [45].

Transmission Electron Microscopy was performed to analyze the shape and structure of *Equus*Mel particles using JEOL JEM 2100 LaB6. The particles solution was dropped on a carbon coated TEM grid (Structure Probe, Inc., West Chester, PA). Once the surface of the carbon coated TEM grids dried, it was transferred to the TEM grid holder and examined without staining. The acceleration voltage was set to 200 kV. All images were collected via the CCD camera attached to the TEM.

Raman spectra were collected using an AFM-Raman microscope (NTEGRA Spectra, NT-MDT Spectrum Instruments, Moscow, Russia) with a 10x objective and 500 nm wavelength laser over a Raman shift range of 800–2500 cm^{-1}. Data from five separate scans using 1 mW of laser power and 10 s exposure time were averaged to minimize sample degradation while maximizing the signal-to-noise ratio. Raman peak deconvolution was performed using automatic multiple peak fit methods and viogt function (Originlab, Northampton, MA., USA).

Fourier transform infrared spectroscopy (FTIR) Spectra of melanin samples were directly measured with Thermo Nicolet instrument (Is10 FTIR, Thermo Nicolet, Thermo Fisher Scientific, USA). Spectra were recorded in wavenumber range of 400-4000 cm^{-1}, resolution of 4 cm^{-1} and 30 sample scans.

UV-Vis spectra of *Equus*Mel (200 µg/ml in DMSO) was measured by a spectrophotometer (Nanodrop 2000c, Thermo Scientific, USA) from a wavenumber range of 250-850 cm^{-1}.

X-ray Photoelectron Spectroscopy was performed using the Kratos Axis Supra XPS. Survey and high-resolution spectra of 1s orbitals of carbon (C), oxygen (O), and nitrogen (N) were obtained using Al source. Elemental analysis was done by the peak areas and the relative sensitivity factors of the instrumentation to individual atomic species. High-resolution spectra were further analyzed by CasaXPS software.

Specific surface area and pore size distribution of *Equus*Mel was examined by nitrogen physisorption measurements using NOVA 2200E BET (Quantachrome Instrument) at 77.3 K. *Equus*Mel was degassed at 200 °C for 12 h before BET measurements.

Static water contact angle was measured by sessile drop method using optical tensiometer (Theta lite Tensiometer, Biolin Scientific, Gothenburg, Sweden). 10 µl of ddH_2O droplet was applied on the melanin pellet (50 mg) that was hydraulic pressed with pressure, p = 4 metric tons at room temperature. Water contact angle was automatically calculated according to five point-traced droplet shapes.

2.2.4 Antibacterial activity

The antibacterial activity of *Equus*Mel and SynMel biopolymers was evaluated using gram-negative *Escherichia coli* (*E. coli,* ATCC®15597™) and gram-positive *Staphylococcus aureus* (*S. aureus*, ATCC®25923™) strains. Prior to each antibacterial test, *E. coli* and *S. aureus* were streaked from a frozen glycerol stock onto lysogeny broth (LB) agar and commercially prepared tryptic soy agar with 10% sheep red blood cells (TSA-B) agar, respectively. A single bacterial colony was collected from the *E. coli* and *S. aureus* plates and inoculated in 5 mL of LB and brain heart infusion (BHI) liquid media, respectively. The cultures were incubated for 16 h at 37°C in a platform shaker. Bacterial growth concentrations were determined by means of optical

density (OD) (Spectrophotometer, Nanodrop 2000c, Thermo Scientific, USA) at a 600 nm wavelength. Different concentrations of melanins (2.5, 5, 20, and150 mg/ml) were inoculated with 5×10^5 CFU/ml bacteria suspensions in a 96-well plate. The plates were incubated at 37℃ for 1, 2, 4, and 24 h. Aliquots of the samples were serially diluted and plated on agar media for overnight incubation at 37°C. Visible colonies were counted and compared with the negative controls, which grown without melanins. Each experiment was repeated three times. The bactericidal activity rate (R) of the *Equus*Mel and SynMel was calculated according to following equation:

$$R = \frac{N_C - N_S}{N_C} \times 100\ \%$$

where N_C represents average concentration of bacteria in control and N_S represents average concentration of bacteria when treated with a specific concentration of melanin.

2.2.5 Pro-oxidant activity assay

The level of H_2O_2 production was used as the metric for reactive oxygen species (ROS) generation. Melanins at different concentrations (2.5, 5, 20, and 150 mg/ml) were incubated with ddH_2O for 4 h under ambient condition. Aliquots of the aqueous solutions were assayed for the generation of H_2O_2 using Amplex Red reagent (ThermoFisher Scientific, Waltham, MA USA) [46]. In brief, the assay detects the excitation and emission at wavelengths of 571 and 585 nm. The amount of H_2O_2 can be detected by the degree of oxidation from 10-acetyl-3,7-dihydroxyphenoxazine (ADHP) to resorufin (**Figure 2.2**). Data were measured using a

fluorescence plate reader (SpectraMax M2e/EA, Molecular Devices, San Jose, CA USA). Each experiment was repeated three times.

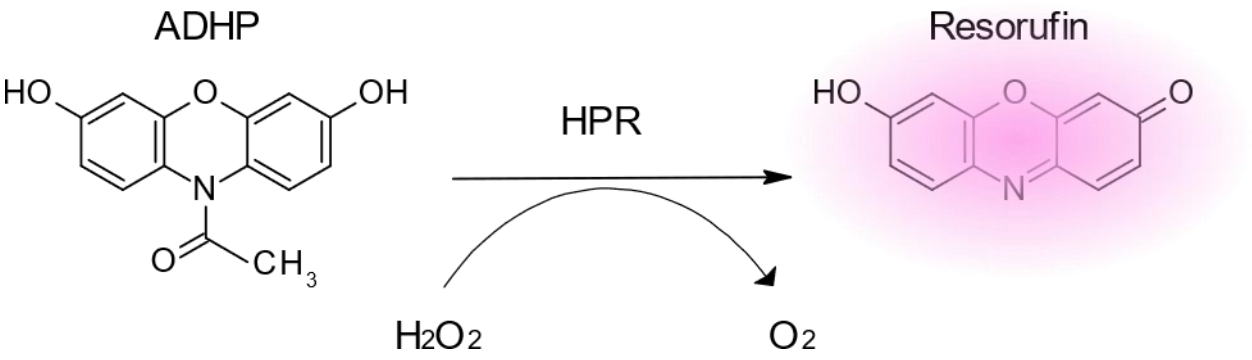

Figure 2.2: ADHP is a non-fluorescent and colorless compound that upon enzymatic oxidation is transformed into resorufin which is a highly absorbing and fluorescing compound. Amplex™ Red assay is widely used for specific and quantitative analysis of extracellular H_2O_2.

2.3 Results and discussion

2.3.1 Extraction and characterization of *Equus*Mel

Melanins from the hair are synthesized by specialized dendritic cells, which are melanocytes derived from the neural crest [47]. Various techniques have been applied to extract melanins from hair, i.e., base dissolution & acid isolation, dissolution in ionic liquid, and acid hydrolysis. Among these techniques, acid hydrolysis was used in this study due to facile extraction steps, which results in high purity and yield [44]. The initial *E. ferus* hair and resulting melanin powder (*Equus*Mel) after the acid hydrolysis extraction are shown in supporting **Figure 2.3 (a and b)**. The UV-vis absorption spectrum of *Equus*Mel shows a monotonic decrease with no noticeable peak throughout the visible wavelength region, which is similar to other naturally-sourced melanin pigments (**Figure 2.3(c)**) [48].

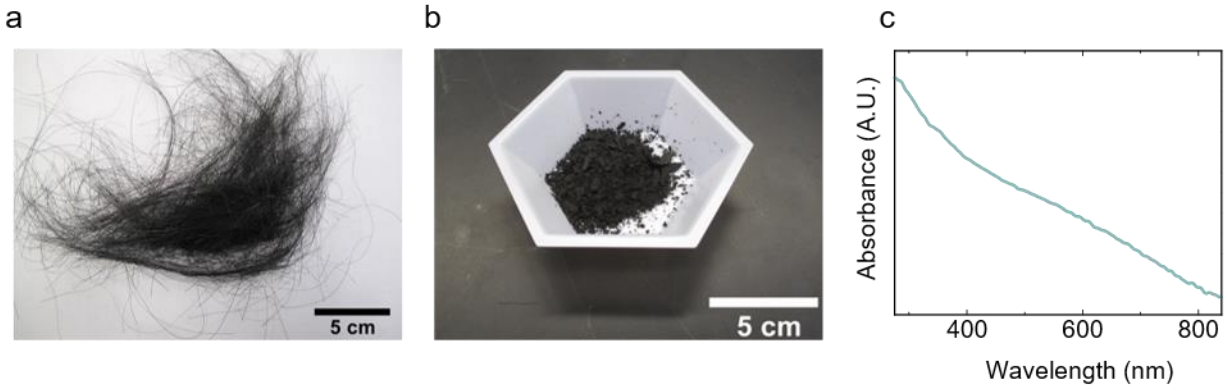

Figure 2.3: (a) *Equus ferrus* hair fibers and (b) *Equus*Mel powder after extraction. (c) UV-Vis absorbance spectrum is shown for the *Equus*Mel solution (200 μg/ml). This exhibits the broad band monotonic absorbance without the distinct peaks.

The microstructure of *Equus*Mel is shown in **Figure 2.4 (a)**. Broadly, it shows an elliptical shape in the range of 638 ± 93.7 nm in length and 266.3 ± 56 nm in width. Compared to the homogeneous and spherical nanoparticle form factors of the naturally occurring melanins extracted

from *Sepia officinalis* ink sac, *Equus*Mel exhibits less homogeneous structure [49]. TEM images display the sub-nanometer scale textured microstructures, especially at the exterior of the individual particulates (**Figure 2.4(b and c)**). Furthermore, both wide-angle (WAXS) and small-angle (SAXS) X-ray scattering measurements demonstrate that there is a noticeable scattering peak at q = 0.14 $Å^{-1}$. This is indicative of an ordered structure in *Equus*Mel with d-spacing of 45.2 Å (**Figure 2.4(d and e)**). Relatively weak and broad behavior was found from the higher order peaks at q > 0.2 $Å^{-1}$, and the ratio of the scattering peaks did not match with other well-known structures such as lamellae, or hexagonally packed cylinders. This ordered structure in meso-scale is considered as the spacing between the layers or the aperture of the fibril structure that is originated from the melanogenesis [50], [51]. Melanogenesis is the biological process that takes place in specialized organelles called melanosomes. Melanosomes use enzymes, such as Pmel17, that catalyze polymerization reactions to control melanin assembly. Pmel17 assembles melanin protomolecules into large fibrils within melanosomes *in vivo* [51], [52]. This natural synthesis mechanism leads to the extended fibrils and porous structure of *Equus*Mel in meso-scale. Similar ordered arrangement can be found from the atomic force microscopy of the melanins isolated from *S. officinalis* ink, which reveals the presence of palisade-like filaments in the order of 3-6 nm [53]. The semi-crystalline structure in meso-scale is largely a unique characteristic of various naturally-derived melanin pigments [54]. Layered structure in sub-nanometer scale can be found from yak and human hair melanins and the melanins from *S. officinalis* ink sac, which exhibit ordered arrangement ranges from 2 to 6 Å [54], [55]. Both microscopy and X-ray scattering data suggest that *Equus*Mel largely consists of a fibril mesostructure with a distance of 45.2 Å. This unique structural feature of *Equus*Mel is dissimilar with the synthetic melanins (SynMel) prepared by autooxidation of tyrosine ,which contain amorphous topography [35].

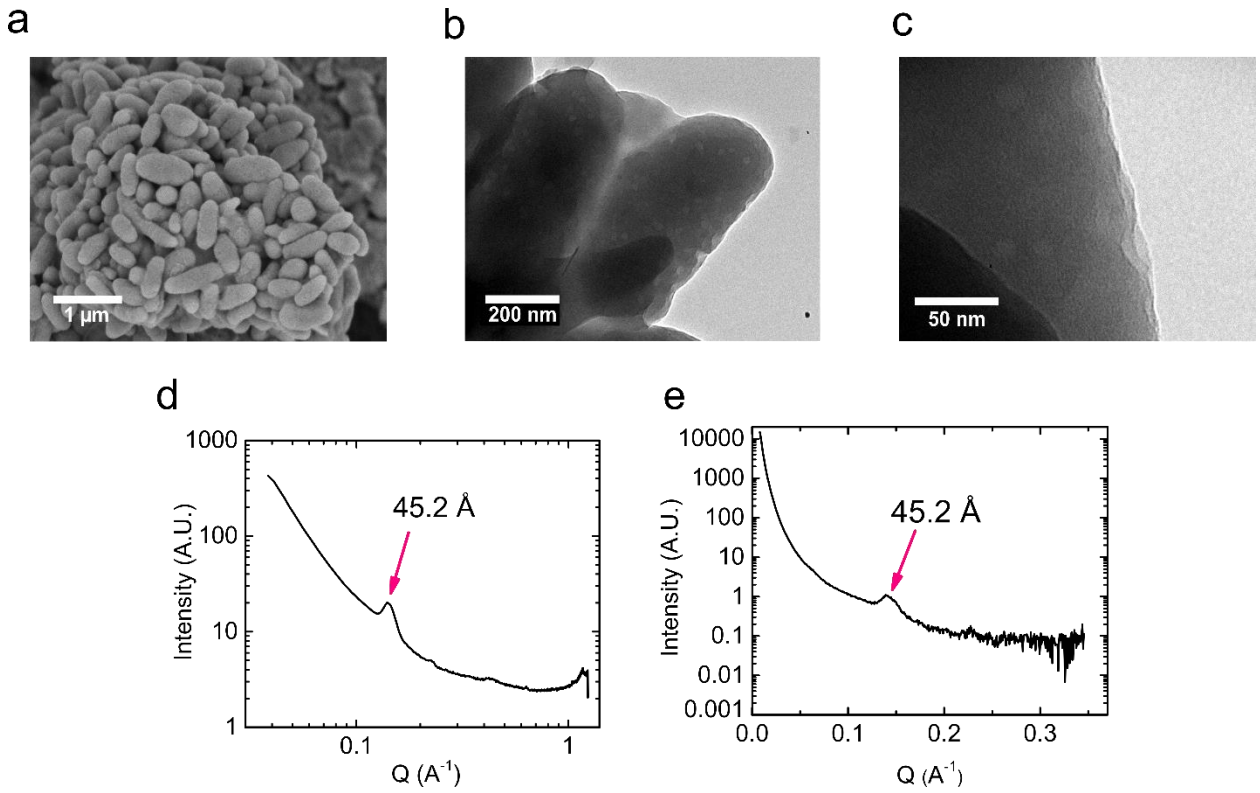

Figure 2.4: (a) SEM and (b and c) TEM images of *Equus*Mel show the elliptical microstructure with a mesoporous and layered structure within the individual particles. (d) both wide-angle (WAXS) and (e) small-angle (SAXS) X-ray scattering corroborates the presence of a semicrystalline structure of *Equus*Mel in a meso scale that largely contains the ordered layers with a d-spacing of 45.2 Å.

The ordered meso-scale structure of *Equus*Mel can also be observed by measuring nitrogen physisorption. Pore size distribution of *Equus*Mel determined by the Barret-Joyner-Halenda (BJH) method exhibits the presence of the primary pores within the range of 30-50 Å, which is in a good agreement with the d-spacing of 45.2 Å from WAXS and SAXS (**Figure 2.5(a)**). In addition, N_2 adsorption-desorption isotherms indicate that *Equus*Mel contains Brunaur-Emmett-Teller (BET) surface area of 3 m^2/g (**Figure 2.5(b)**) [56]. This BET surface area is slightly lower compared to those from the natural melanin from *Sepia officinalis* ink sac (19.9 m^2/g), and the synthetic melanin (10.7 m^2/g) [35]. *Equus*Mel exhibits a type IV behavior according to the presence of a rounded

point at low values of p/p_o and an indistinct slope at intermediate values of p/p_o. These features correspond to the formation of monolayers and multilayers, respectively.

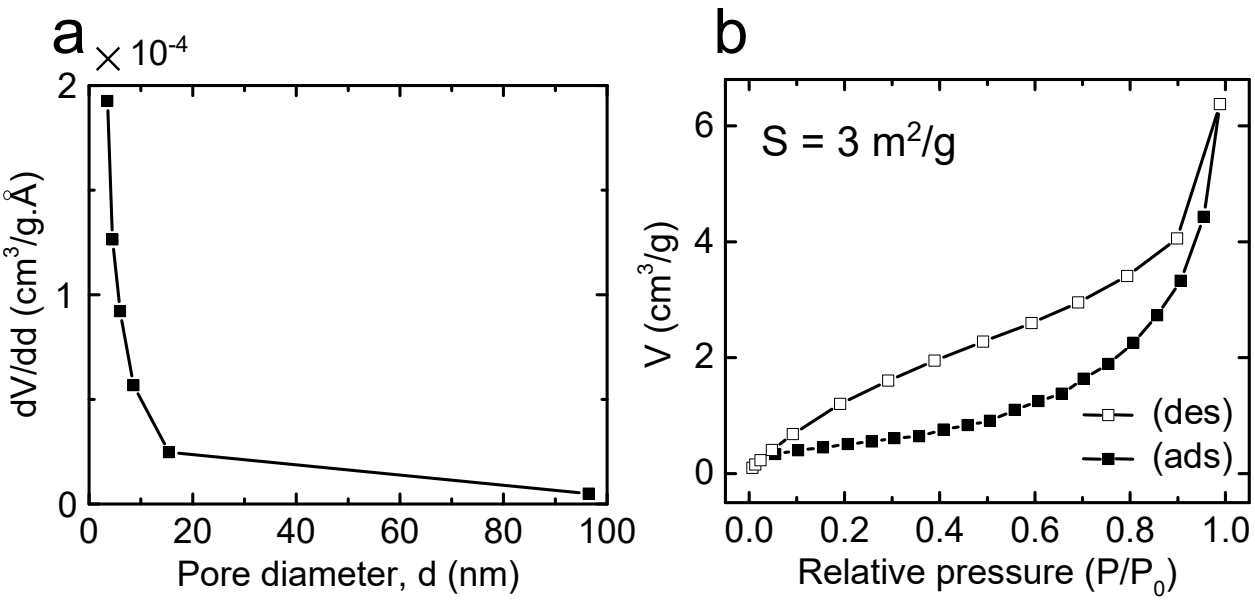

Figure 2.5: (a) Pore size distribution determined by the Barrett–Joyner–Halenda method shows the existence of primary pores within the range of 30–50 Å. (b) Nitrogen adsorption–desorption isotherms exhibit the multilayered type IV structural behavior with a BET surface area of 3 m^2/g.

Chemical cues of *Equus*Mel and SynMel were interrogated by Fourier transform infrared spectroscopy (FTIR), confocal Raman spectroscopy, and X-ray photoelectron spectroscopy (XPS) (**Figure 2.6**). FTIR spectra of both melanins exhibit no significant differences indicating similar chemical functionality. The broad band recorded at 3800-2800 cm^{-1} is assigned to O-H stretching from carboxylic acid or catechol groups [57]. The peak centered at 1260 cm^{-1} represents C-N stretching of pyrrole ring or O-H deformation of catechols [58], [59]. The peaks centered at 1650 and 1720 cm^{-1} are attributed to conjugated C=C and vibration of aromatic C=O, which are present in both *Equus*Mel and SynMel [49]. Two distinct peaks at 2950-2850 cm^{-1} were observed from *Equus*Mel but not from SynMel. These peaks are attributed to the stretching vibration of aliphatic

C–H bonds that are induced by lipid or amino acid residues during extraction [60]–[62]. Detailed FTIR peak assignments are summarized in **Table 2.1**.

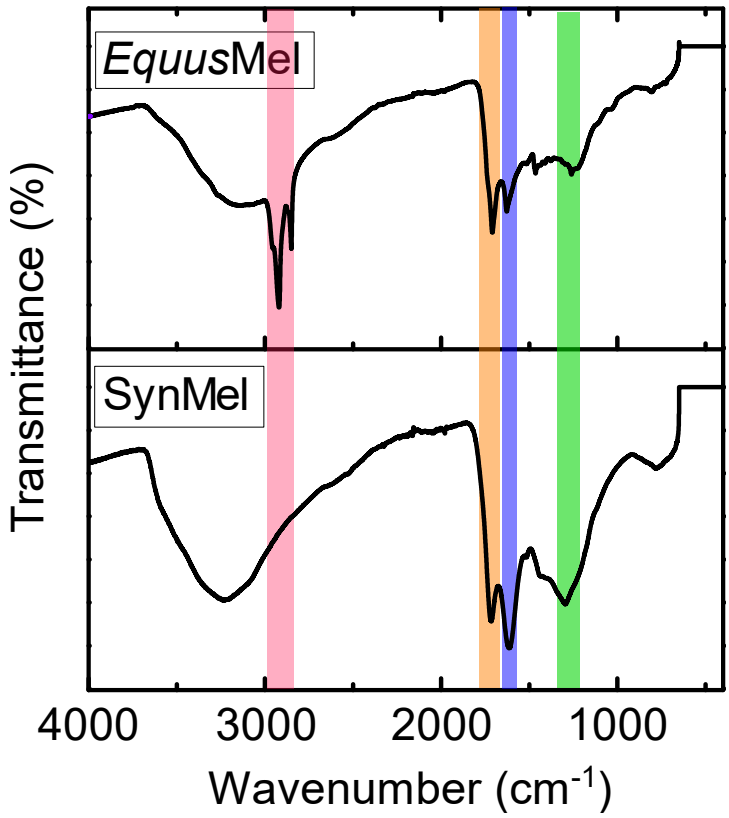

Figure 2.6: FTIR spectra of *Equus*Mel and SynMel. Two distinct peaks at 2850–2950 cm^{-1} suggest the presence of the aliphatic C–H stretch in *Equus*Mel.

Table 2.1: Peak assignments of FTIR spectra for *Equus*Mel and SynMel.

Absorption bands, cm^{-1}	Vibration mode and main functional groups
3800 – 2800	Stretching vibration of O–H and N–H groups (carboxylic acid and phenolic OH, anime in indole, pyrrole and amino acids)
2950 – 2850	Stretching vibration of C–H
1720 – 1706	Stretching vibration of aromatic C=O in carboxylic acid
1650 – 1600	Stretching vibration of Conjugated C=C
1342 – 1266	Stretching vibration of C−N in indole
680 – 860	Bending vibration of aromatic C−H

Raman spectra of *Equus*Mel and SynMel exhibit the broad peak ranges between wavenumbers of 1000 and 2000 cm^{-1}. (**Figure 2.7**) These behaviors are associated with the vibrational mode of indole groups [63], [64]. Raman spectra were deconvoluted into five peaks (α- ε) that are designated to the known functional groups in melanin subunits [32]. No significant peak shift was found between *Equus*Mel and SynMel, indicating the similarity in chemical signatures between both melanins. Deconvolved peak assignments are summarized in **Table 2.2**.

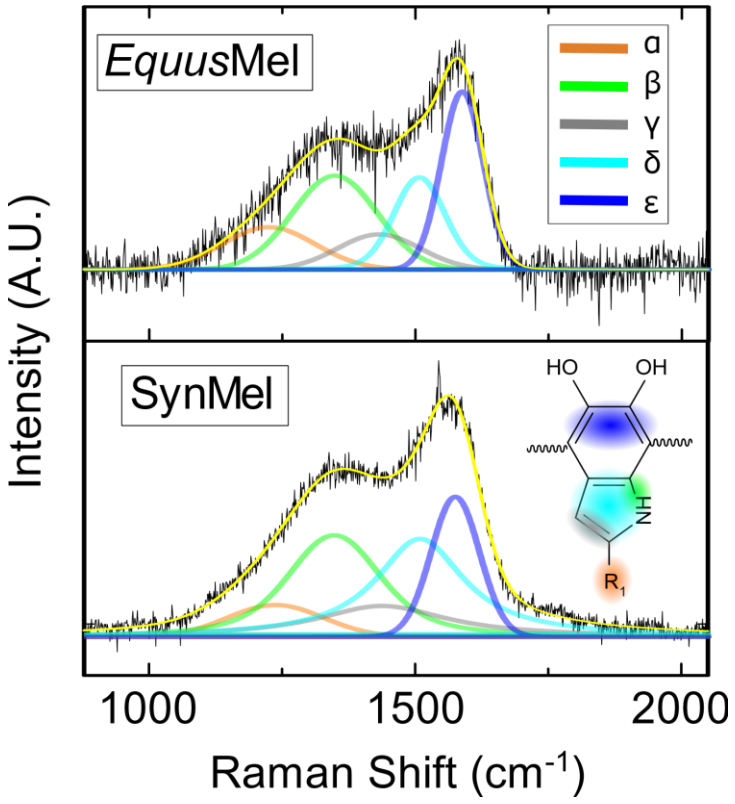

Figure 2.7: Raman spectra of *Equus*Mel and SynMel are deconvolved into five bands (α – ε). Black lines represent the raw spectra. Bindings are highlighted in the respective colors in the chemical structure of eumelanin. Functional group R1 is COOH for SynMel and COOH or H for *Equus*Mel.

Table 2.2: Peak positions of Raman spectra of *Equus*Mel and SynMel are shown after the deconvolution using Voigt function.

Peak position, cm^{-1}		Vibration mode and main functional groups
*Equus*Mel	SynMel	
1224.404	1237.68445	(α) C–O stretching in carboxylic acid and C–OH
1348.694	1348.01362	(β) stretching vibration of aromatic C–N in indole
1431.441	1437.68445	(γ) pyrrole ring stretching
1507.377	1509.1941	(δ) stretching vibration of C=N in semiquinone and bending vibration of N–H
1588.081	1575.48241	(ε) stretching vibration of aromatic C=C in indole

XPS was used to further examine the chemical contrast between *Equus*Mel and SynMel (**Figure 2.8**). Atomic weight percentages based on XPS survey peak indicate that *Equus*Mel contains more carbon and less oxygen and nitrogen compared to SynMel (**Figure 2.8(b and c)**). Considering the carbon as the main backbone of indole and the oxygen in the functional groups, we could speculate that a lower population of redox-active groups is present in *Equus*Mel compared to SynMel.

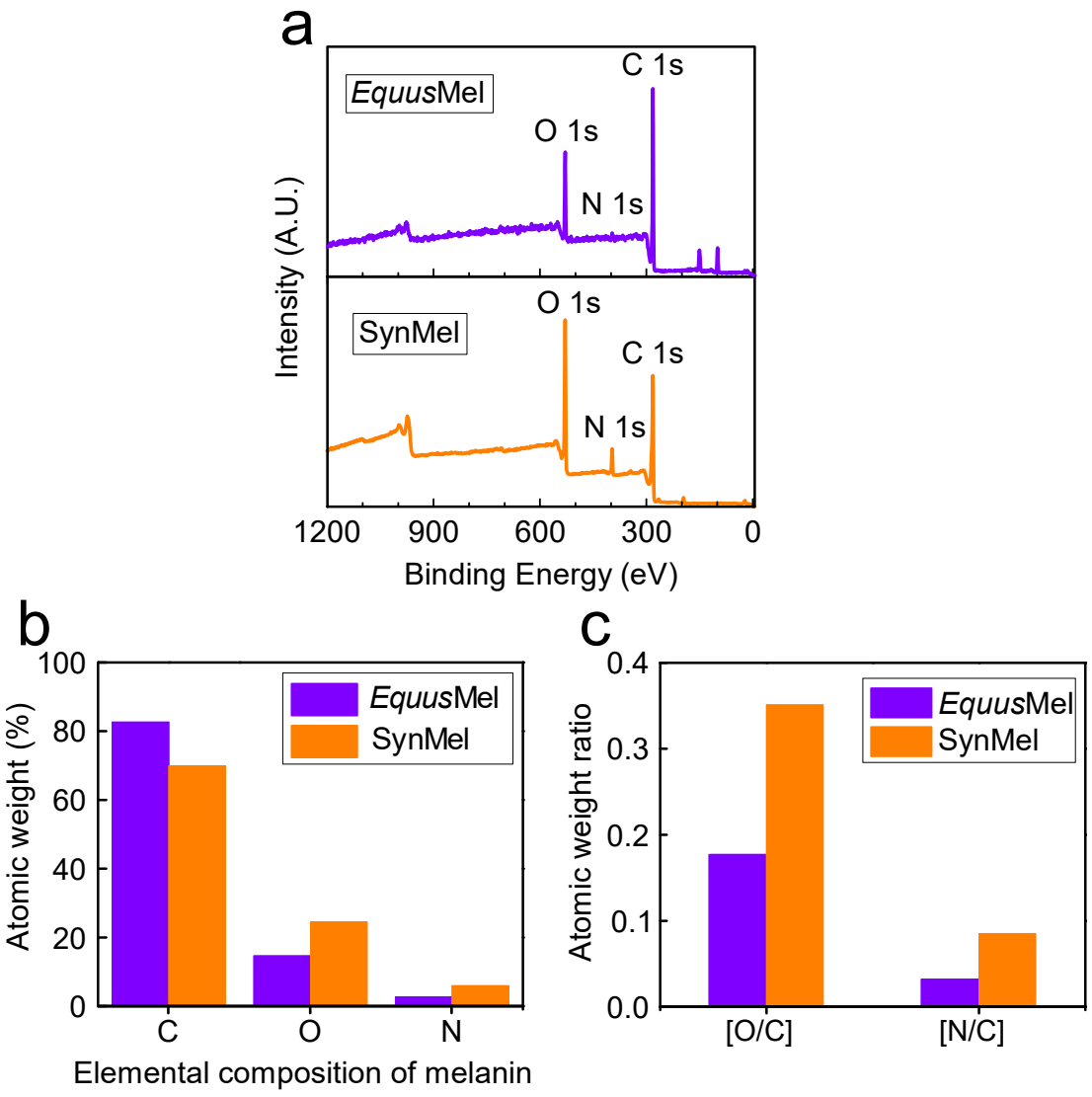

Figure 2.8: (a) XPS are shown for *Equus*Mel and SynMel. The atomic weight percentages of melanins shown in (b) suggest that *Equus*Mel largely contains higher carbon and lower oxygen and nitrogen contents than SynMel. (c) The weight ratio of oxygen and nitrogen is shown based on the weight% of carbon.

A similar trend can be observed from the high-resolution C1s peak analysis. Each C1s peak was deconvolved into two peaks with the binding energies at 284.8, and 287.2 eV that are associated with C-C/C=C, and C-N/C-O functionalities, respectively. Peak area comparison between two peaks indicates higher population of C-N/C-O from SynMel than *Equus*Mel (**Figure 2.9(a)**). High-resolution O1s peaks enable to further quantify the distinction in the amount of redox-active functional groups that exists between *Equus*Mel and SynMel. Deconvolved O1s peaks (**Figure 2.9(b)**) exhibit two peaks centered at 532.39, and 533.82 eV from *Equus*Mel and 532.39, and 531.12 eV from SynMel. The peaks at 533.82, and 531.12 eV are attributed to COOH and C-O functionalities. The deviation of these two peaks could result from the vibrational energy difference of carboxylates that were synthesized via a different route. The major peak at 532.39 eV is assigned to C-OH from the catechol functional group [35]. Higher presence of C-OH group was found in *Equus*Mel (90.51%) compared to SynMel (81.03%). Moreover, the association of the high-resolution O1s peak at 532.39 eV and the atomic weight percentage from the survey peak can provide insightful understanding about the potential population of redox-active catechol groups. *Equus*Mel contains 14.65 % oxygen (survey peak), of which 90.51 % is present in C-OH chemical form, indicating the total C-OH population is 13.3 %. Similar assessment results in 19.9 % (81.03 % x 24.55 %) of the C-OH composition present in SynMel. Taken together, XPS analysis indicates that the redox-active catechol group of *Equus*Mel is approximately 1.5 times less than that of SynMel. It should be noted that exposure to acid during the extraction process may damage the structure, which could result in reducing the chemical functionalities of *Equus*Mel [65].

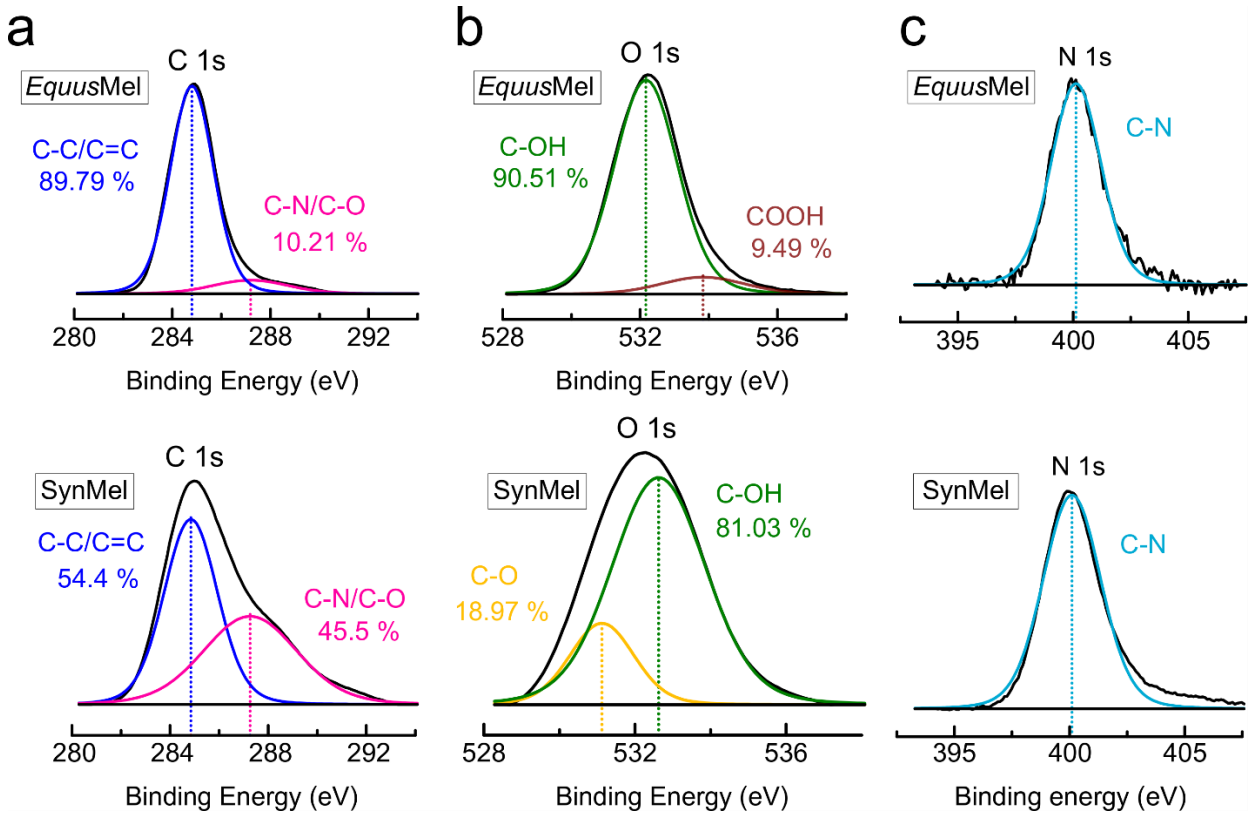

Figure 2.9: (a) The high-resolution carbon peak indicates the higher presence of the aromatic C–C or C=C bonding compared to the C–N or C–O stretching. High-resolution peaks of oxygen in (b) corroborate the higher content of catechol groups from both *Equus*Mel and SynMel. (c) The peak at binding energy of 400 represents C-N stretching from the secondary amine functional group in indole. High-resolution peaks are deconvolved by CasaXPS and shown as color lines. Detailed peak positions are summarized in Table 2.3.

Table 2.3: Summary of high-resolution XPS analysis of *Equus*Mel and SynMel.

	Binding energy, eV		
	O 1s	N 1s	C 1s
*Equus*Mel	532.17 [C–OH]	400.12 [C–N]	284.8 [C–C]/[C=C]
	533.82 [COOH]		287.19 [C–N]/[C–O]
SynMel	531.12 [C–O]	400.10 [C–N]	284.8 [C–C]/[C=C]
	532.62 [C–OH]		287.26 [C–N]/[C–O]

2.3.2 Antibacterial activity and its mechanism of action

To study the antibacterial activity of melanin across two distinct bacterial taxa, we chose well-known type strains of the gram-positive *Staphylococcus aureus* and the gram-negative *Escherichia coli*. Both species are common members of the human microflora but are also known to cause serious infections [66]. The antibacterial activity of both *Equus*Mel and SynMel melanins against *E. coli* and *S. aureus* was quantitatively evaluated using a colony count method after incubating each bacterial species ($c = 5 \times 10^5$ CFU/ml; CFU-colony forming units) with various melanin concentrations. Survival rates are depicted in **Figure 2.10 (a)** and **(c)** after 4 h incubation. Both melanins generally exhibit significant decline in the number of CFUs of *E. coli* and *S. aureus* in comparison to the negative controls. Complete bacterial inhibition (i.e., no CFUs were observed) was achieved when incubated in melanin concentrations of 20 mg/ml and higher. This is comparable with antibacterial activity of natural cationic polymers such as chitosan. Chitosan is a positively charged polysaccharide synthesized by deacetylation of chitin [67]. Qian *et al.* achieved 35% and 50% reduction in *E. coli* and *S. aureus* growth, respectively after co-incubation with chitosan nanoparticles (12 µg/ml) for 24 h [68]. SynMel appears to have a greater impact in inhibiting bacterial growth than *Equus*Mel at concentrations of 2.5 and 5 mg/ml. The variation of antibacterial activities between *Equus*Mel and SynMel is correlated with the different density of redox-active functional groups that are present in each melanin. **Table 2.4** summarizes the bactericidal activity of *Equus*Mel and SynMel against *E. coli* and *S. aureus*.

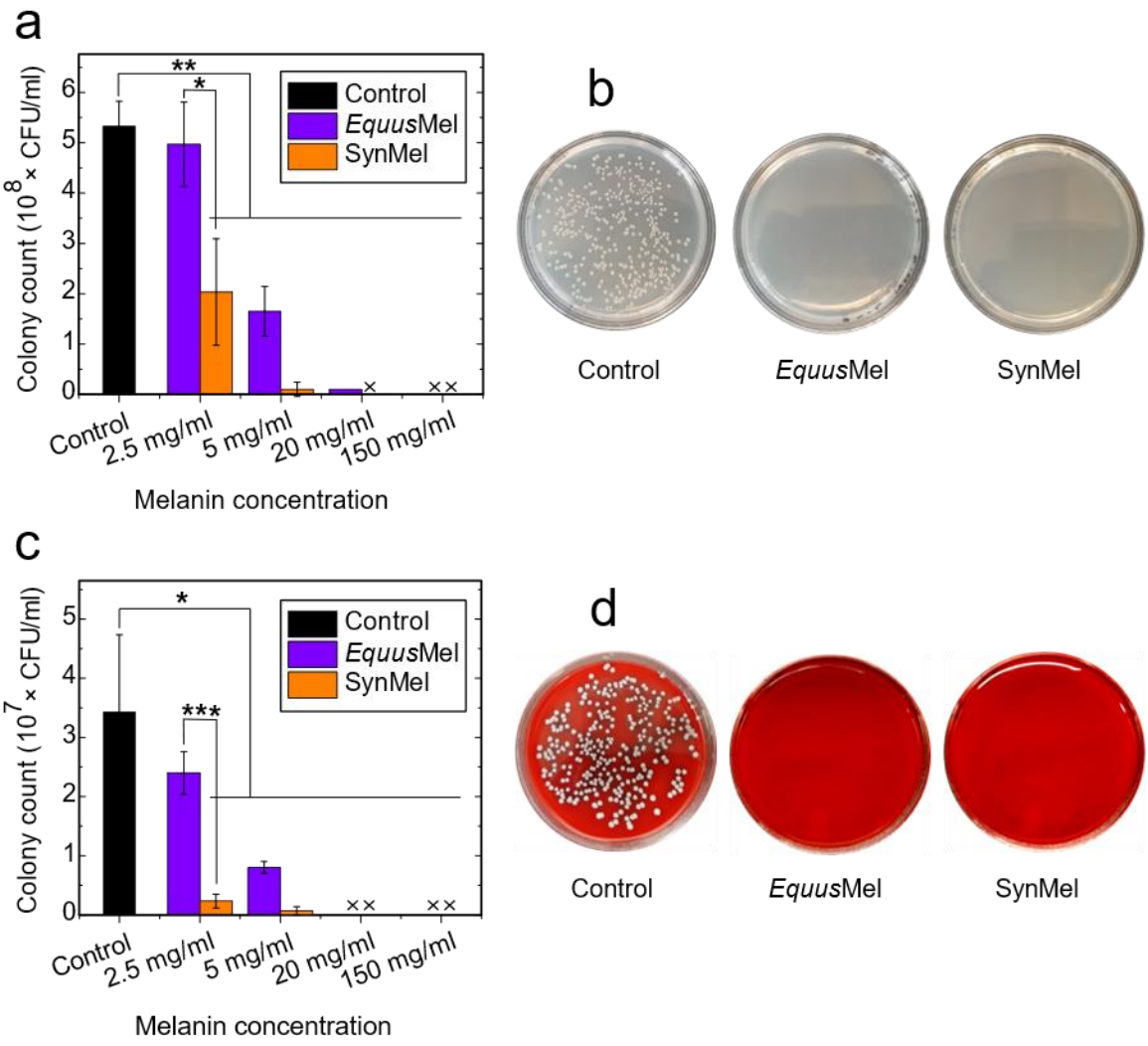

Figure 2.10: *In vitro* antibacterial activities are tested using (a) *E. coli* and (c) *S. aureus*. Bacteria colony count was performed after 4 h exposure to *Equus*Mel and SynMel at 37 ℃ with four different concentrations. Bacterial growth is broadly suppressed compared to the controls. Apart from 2.5 mg/ml *Equus*Mel, all concentrations of both melanins exhibit significant decreases in bacterial growth for both *E. coli* and *S. aureus*. X indicates zero colonies. Data are presented as mean ± SD (n = 3). Statistically significant differences are indicated by ***$p < 0.001$, **$p < 0.01$, and *$p < 0.05$ compared to the control. Detailed bactericidal activities are given in Table 2.4. Representative images of agar plates are shown after incubating (b) *E. coli* and (d) *S. aureus* in melanins (150 mg/ml) for 4 h at 37 ℃.

Table 2.4: Bactericidal activity of *Equus*Mel and SynMel against *E. coli* and *S. aureus* after incubating for 4 h.

Bacterial species	*E. coli*		*S. aureus*	
Melanin Type / Concentration (mg/ml)	***Equus*Mel**	**SynMel**	***Equus*Mel**	**SynMel**
150	100 %	100 %	100 %	100 %
20	98.12 %	100 %	100 %	100 %
5	69.06 %	98.12 %	76.67 %	98.54 %
2.5	6.87 %	61.87 %	30.1 %	93.2 %

In addition, the difference of antibacterial activities may be due to the dissimilar surface characteristics of melanins. Static water contact angle measurement suggests that SynMel has a superhydrophilic surface (contact angle = 0°), while the *Equus*Mel surface is hydrophobic (contact angle = 104.7 ± 2.2°) (**Figure 2.11**). The hydrophobic surface characteristics are ubiquitous and can be found from the melanins that are naturally sourced [59]. The inherent hydrophobic nature of *Equus*Mel would possibly lead to the aggregation of particles, hindering the full interface with bacteria. This contrast of surface properties could potentially lead to the lower antibacterial activity of *Equus*Mel.

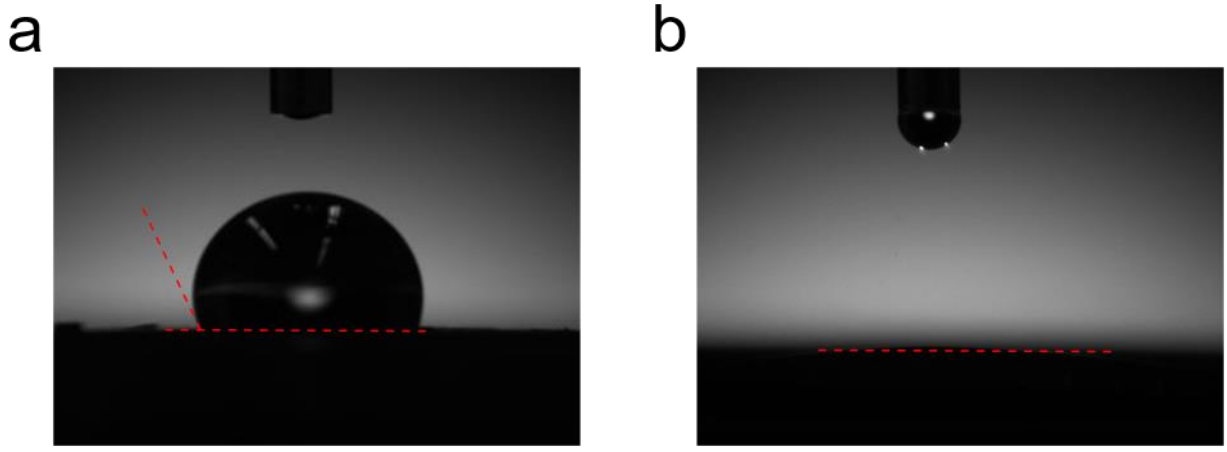

Figure 2.11: Static water contact angle measurement exhibits (a) hydrophobic *Equus*Mel (contact angle= 104.7 ± 2.2°) and (b) superhydrophilic SynMel (contact angle= 0°). Melanin pellets were prepared to exhibit the flat top surface before applying 10 µl of ddH_2O.

Antibacterial activity via melanins is further examined by the time-course reduction of *E. coli* and *S. aureus*. We determined the growth inhibition of each bacteria by counting colonies at timepoints between 0 and 24 h, as shown in **Figure 2.12** Both *E. coli* and *S. aureus* exhibit substantial reduction in the number of CFUs throughout the measurement period in comparison to the monotonic growth of the controls. However, the time to complete bacterial inhibition varies between *Equus*Mel and SynMel. The growth of both bacterial species was completely suppressed after 2 h of incubation in SynMel while *Equus*Mel exhibited a slower response until 4 h of incubation. The delayed response of *Equus*Mel is associated with the inherent characteristic of *Equus*Mel that contains a lower density of redox-active catechol groups than SynMel. These rates of bacteria growth inhibition by both melanins are comparable to the recent studies. A recent study shows that growth curves obtained from incubation of chitosan nanoparticles with *S. aureus* V329 decreases in CFUs starting after 2 h [67]. In addition, Sarwar *et al.* observed complete bacterial growth inhibition after incubating chitosan at different molecular weights with *E. coli* and *S. aureus* for 8 h.[69]

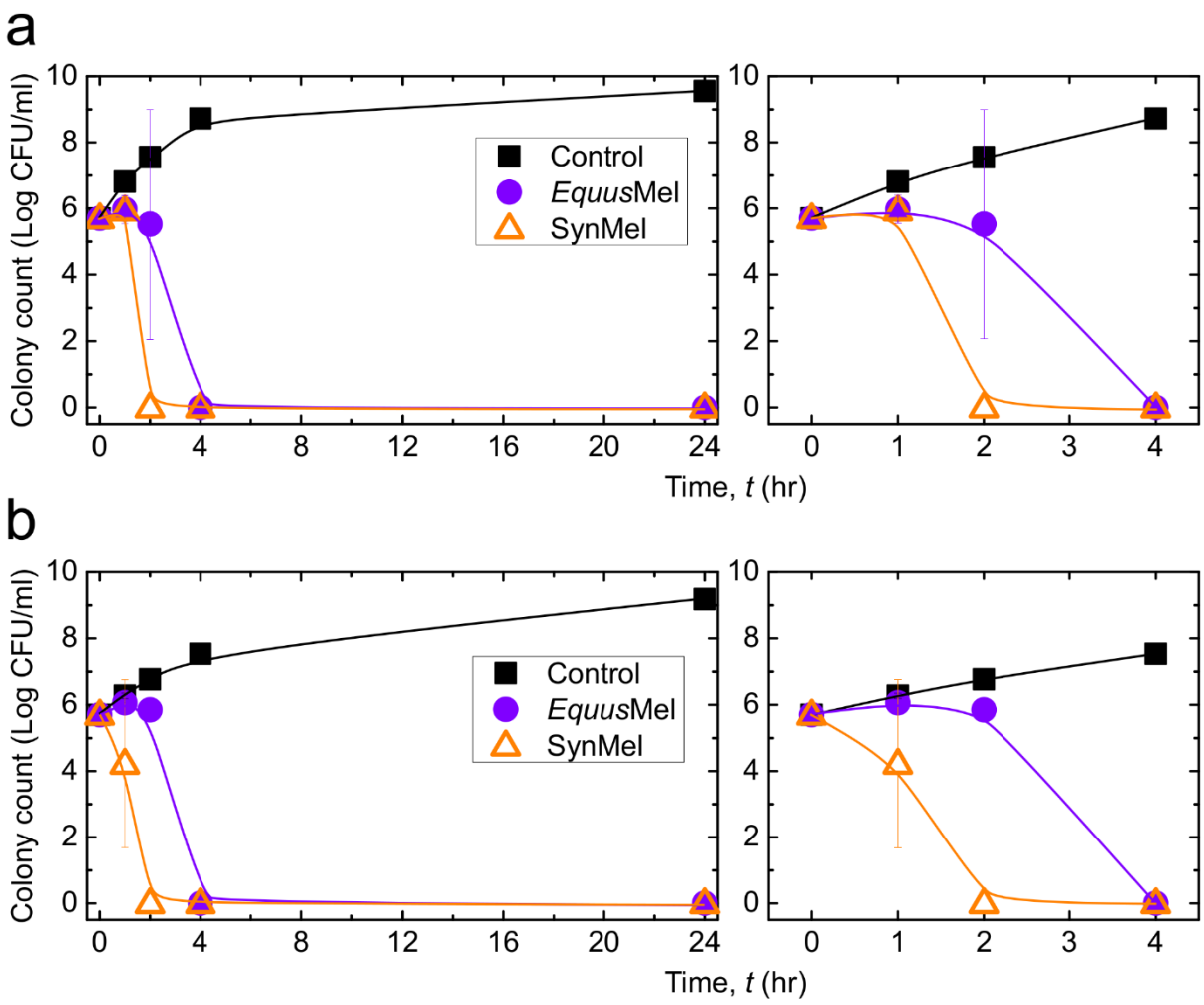

Figure 2.12: Temporal kinetics of bacterial reduction is shown for (a) *E. coli*, and (b) *S. aureus* through 24 h incubation at 37 ℃. *Equus*Mel exhibits a slight delayed response until 2 h compared to SynMel, however 100 % reduction is achieved for both melanins after 4 h of incubation. Bacteria incubation was performed at 37 ℃ with a melanin concentration of 150 mg/ml under ambient light (n = 3). Graphs on the right column show the enlarged view of the full measurements. Trendlines are generated by interpolating the measured data.

Generation of ROS by *Equus*Mel and SynMel was quantitatively corroborated by the H_2O_2 generation using a colorimetric assay. Oxidative stress by ROS is one of the main mechanisms that can damage the structure and function of proteins and other cellular components and may lead to cell death. Superoxide radical ($O_2^{\bullet-}$), hydroxyl radical ($HO^{\bullet}$), hydroperoxyl radical ($HO_2^{\bullet}$), singlet oxygen ($^1O_2$), and hydrogen peroxide (H_2O_2) are representatives of ROS [13]. Among the ROS candidates, H_2O_2 is chosen in this study since it provides a quantitative result with facile measurement [70]. Four different concentrations of *Equus*Mel and SynMel were incubated for 4 h in ddH_2O under ambient light, and H_2O_2 concentrations were measured (**Figure 2.13(a)**). The colorimetric assay displays the increment of H_2O_2 generation as the concentrations of melanins increase. The concentrations of 2.5 mg/ml *Equus*Mel and 150 mg/ml SynMel reacted to form the lowest (0.56 µM) and highest (129.8 µM) concentrations of H_2O_2, respectively. It should be mentioned that at low concentration of H_2O_2, *E. coli* and *S. aureus* cells die as a result of damage to DNA, whereas at higher concentrations of H_2O_2, the death of the microorganism is due to damage to other part(s) of the cell [71], [72]. The outer structures of the gram-positive *S. aureus* and the gram-negative *E. coli* may explain differences in response to ROS exposure between these two species. *S. aureus* has an external peptidoglycan cell wall that can be directly attacked by ROS while *E. coli* has an outer membrane that provides greater protection against damage [73], [74]. Furthermore, the amounts of H_2O_2 produced from SynMel are 1.5 ± 0.2 times higher than *Equus*Mel. This is in close agreement with our findings of the chemical signatures of redox-active groups in *Equus*Mel. Spectroscopic data indicates that SynMel contains 49.6 % more catechol groups than *Equus*Mel.

The pro-oxidant property of melanins has been also reported in other literatures [70]. Catechols present in melanins are reversibly oxidized into ortho(*o*)-quinones by two-electron two-

proton removal process. During oxidation, oxygen will react with electrons to form hydroxyl or superoxide radicals as an intermediate. The superoxides can further bind to protons to reproduce H_2O_2 [75]. A proposed mechanism is shown in **Figure 2.13(b)**. A previous electron paramagnetic resonance (EPR) study in melanin shows that production of semiquinone and subsequent ROS is light- and water-driven, supporting the proposed antibacterial mechanism [76]. Moreover, another EPR study on catechol-containing material demonstrates ROS generation within the hydrated solution [77]. Although the exact antibacterial mechanism of melanin is still unclear, we cautiously posit that the melanins are able to generate ROS by reversible oxidation of catechols, which can inhibit bacterial growth. Furthermore, the semicrystalline structure of *Equus*Mel may adversely affect its ability to promote the ROS since the multi-layered structure provides a kinetically disadvantageous environment to interact between superoxides and electrons/protons.

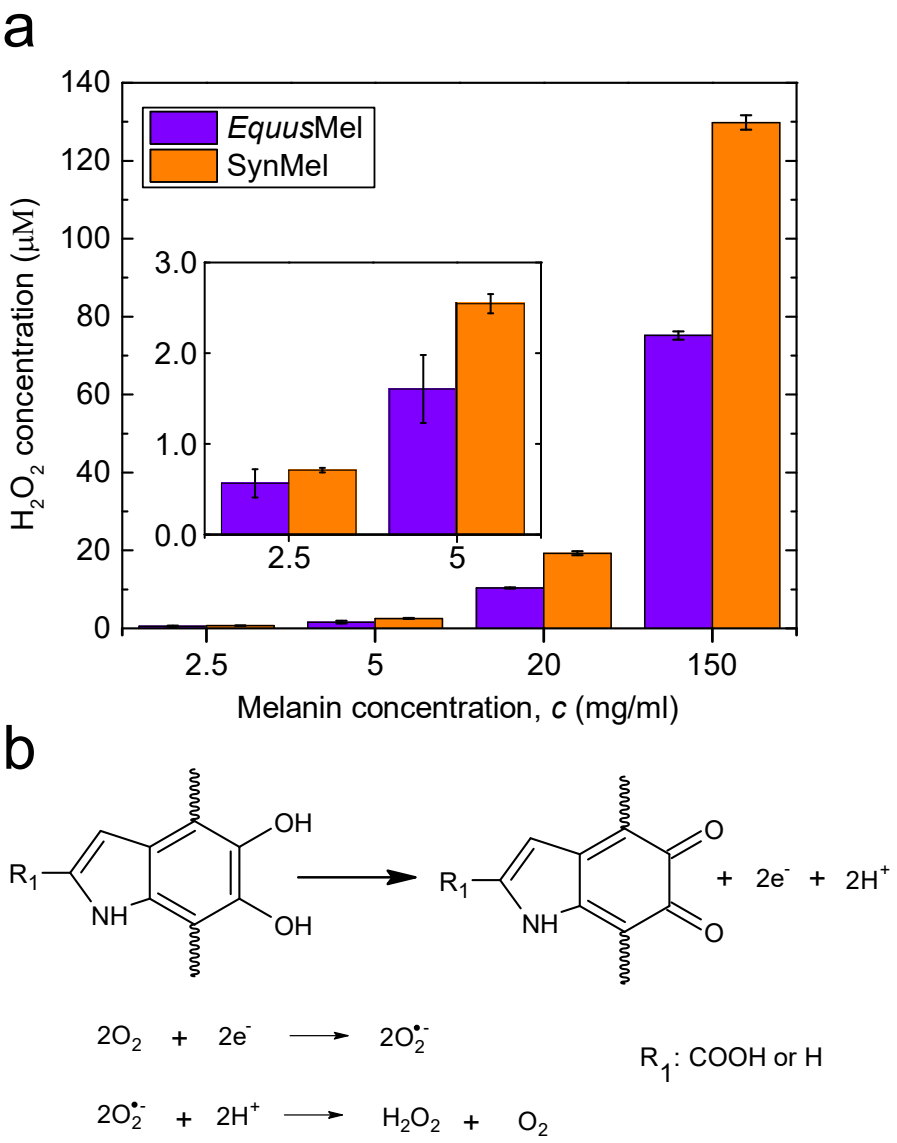

Figure 2.13: (a) The measured concentrations of hydrogen peroxide generated by four defined concentrations of melanins. Measurements were performed by colorimetry assay in 4 h after the aqueous solution under ambient light (n = 3). Inset displays the magnified values from 2.5 and 5 mg/ml. (b) Proposed mechanism of ROS generation by melanins is shown. Oxidation of melanins induces two electrons and protons leading to the production of superoxides. Superoxides and free protons can incorporate to reproduce H_2O_2.

2.4 Conclusion

*Equus*Mel extracted from *E. ferus* hair is examined by microscopic and spectroscopic approach. Electron microscopy verified the elliptical microstructure of *Equus*Mel in nanoscale and the layer-by-layer stacked structure on the exterior surface. Highly organized multilayered structure of *Equus*Mel was corroborated by x-ray scattering measurement, which exhibits ordered spacing of 45.2 Å. Spectroscopic techniques suggest that *Equus*Mel contains similar chemical signatures to melanins extracted from *S. officinalis* and SynMel. Among various chemical functionalities, catechols are considered to be the main functional group that allows the reversible oxidation and reduction within the hydrated condition. ROS generated via oxidation of catechols is considered the main mechanism of antibacterial activity, reaching 100% cell death within 4 h. However, the lower densities of catechol groups present in *Equus*Mel resulted in less amount of ROS promotion compared to SynMel.

The results herein indicate that *Equus*Mel exhibits potential for naturally-derived biopigments to be utilized as functional antibacterial agents for a variety of applications. Antibacterial performance and kinetics can be further improved by molecular level modification of the surface of melanins to extend the redox functionalities [78]–[80]. Exfoliation of the layered structure of *Equus*Mel can also assist to maximize the interface resulting in the enhanced generation of ROS [81]. These classes of biologically-derived melanins can be further applied in a variety of research and engineering areas. Fabrication of a composite membrane with *Equus*Mel would be advantageous to prevent biofilm formation and therefore increase the lifespan of the filtration process [82]. In addition, melanins can be utilized to prepare antibacterial surfaces in biomedical applications including neural interface, biomedical electronics, medical consumables, or clinical equipment [83], [84].

2.5 References

[1] S. Galié, C. García-Gutiérrez, E. M. Miguélez, C. J. Villar, and F. Lombó, “Biofilms in the Food Industry: Health Aspects and Control Methods,” *Front. Microbiol.*, vol. 9, p. 898, May 2018, doi: 10.3389/fmicb.2018.00898.

[2] Z. Khatoon, C. D. McTiernan, E. J. Suuronen, T.-F. Mah, and E. I. Alarcon, “Bacterial biofilm formation on implantable devices and approaches to its treatment and prevention,” *Heliyon*, vol. 4, no. 12, p. e01067, Dec. 2018, doi: 10.1016/j.heliyon.2018.e01067.

[3] J. S. VanEpps and J. G. Younger, “Implantable Device-Related Infection,” *Shock*, vol. 46, no. 6, pp. 597–608, Dec. 2016, doi: 10.1097/SHK.0000000000000692.

[4] C. R. Arciola, D. Campoccia, and L. Montanaro, “Implant infections: adhesion, biofilm formation and immune evasion,” *Nat. Rev. Microbiol.*, vol. 16, no. 7, pp. 397–409, Jul. 2018, doi: 10.1038/s41579-018-0019-y.

[5] R. A., R. J., M. V., A. P., P. Flores, and P. P., “Antibiotic prophylaxis in incisional hernia repair using a prosthesis,” *Hernia*, vol. 5, no. 3, pp. 148–152, Sep. 2001, doi: 10.1007/s100290100026.

[6] M. D. Firouzjaei *et al.*, “Recent advances in functionalized polymer membranes for biofouling control and mitigation in forward osmosis,” *J. Membr. Sci.*, vol. 596, p. 117604, Feb. 2020, doi: 10.1016/j.memsci.2019.117604.

[7] Q. Shen, S.-J. Xu, Z.-Q. Dong, H.-Z. Zhang, Z.-L. Xu, and C. Y. Tang, “Polyethyleneimine modified carbohydrate doped thin film composite nanofiltration membrane for purification of drinking water,” *J. Membr. Sci.*, vol. 610, p. 118220, Sep. 2020, doi: 10.1016/j.memsci.2020.118220.

[8] R. Li, Y. Wu, L. Shen, J. Chen, and H. Lin, “A novel strategy to develop antifouling and antibacterial conductive Cu/polydopamine/polyvinylidene fluoride membranes for water treatment,” *J. Colloid Interface Sci.*, vol. 531, pp. 493–501, Dec. 2018, doi: 10.1016/j.jcis.2018.07.090.

[9] G. Zhang, J. Lv, and F. Yang, “Optimized anti-biofouling performance of bactericides/cellulose nanocrystals composites modified PVDF ultrafiltration membrane for micro-polluted source water purification,” *Water Sci. Technol.*, vol. 79, no. 8, pp. 1437–1446, Apr. 2019, doi: 10.2166/wst.2019.137.

[10] N. S. Leyland, J. Podporska-Carroll, J. Browne, S. J. Hinder, B. Quilty, and S. C. Pillai, "Highly Efficient F, Cu doped TiO2 anti-bacterial visible light active photocatalytic coatings to combat hospital-acquired infections," *Sci. Rep.*, vol. 6, no. 1, p. 24770, Jul. 2016, doi: 10.1038/srep24770.

[11] J. Podporska-Carroll *et al.*, "Antibacterial properties of F-doped ZnO visible light photocatalyst," *J. Hazard. Mater.*, vol. 324, pp. 39–47, Feb. 2017, doi: 10.1016/j.jhazmat.2015.12.038.

[12] A. Nastulyavichus *et al.*, "Antibacterial coatings of Se and Si nanoparticles," *Appl. Surf. Sci.*, vol. 469, pp. 220–225, Mar. 2019, doi: 10.1016/j.apsusc.2018.11.011.

[13] A. Khezerlou, M. Alizadeh-Sani, M. Azizi-Lalabadi, and A. Ehsani, "Nanoparticles and their antimicrobial properties against pathogens including bacteria, fungi, parasites and viruses," *Microb. Pathog.*, vol. 123, pp. 505–526, Oct. 2018, doi: 10.1016/j.micpath.2018.08.008.

[14] B. Ezraty, A. Gennaris, F. Barras, and J.-F. Collet, "Oxidative stress, protein damage and repair in bacteria," *Nat. Rev. Microbiol.*, vol. 15, no. 7, pp. 385–396, Jul. 2017, doi: 10.1038/nrmicro.2017.26.

[15] F. C. Fang, "Antimicrobial Actions of Reactive Oxygen Species," *mBio*, vol. 2, no. 5, pp. e00141-11, Sep. 2011, doi: 10.1128/mBio.00141-11.

[16] A. B. Asha *et al.*, "Rapid Mussel-Inspired Surface Zwitteration for Enhanced Antifouling and Antibacterial Properties," *Langmuir*, vol. 35, no. 5, pp. 1621–1630, Feb. 2019, doi: 10.1021/acs.langmuir.8b03810.

[17] I. Francolini, I. Silvestro, V. Di Lisio, A. Martinelli, and A. Piozzi, "Synthesis, Characterization, and Bacterial Fouling-Resistance Properties of Polyethylene Glycol-Grafted Polyurethane Elastomers," *Int. J. Mol. Sci.*, vol. 20, no. 4, p. 1001, Feb. 2019, doi: 10.3390/ijms20041001.

[18] Q. Wei, T. Becherer, P.-L. M. Noeske, I. Grunwald, and R. Haag, "A Universal Approach to Crosslinked Hierarchical Polymer Multilayers as Stable and Highly Effective Antifouling Coatings," *Adv. Mater.*, vol. 26, no. 17, pp. 2688–2693, May 2014, doi: 10.1002/adma.201304737.

[19] S. Jiang and Z. Cao, "Ultralow-Fouling, Functionalizable, and Hydrolyzable Zwitterionic Materials and Their Derivatives for Biological Applications," *Adv. Mater.*, vol. 22, no. 9, pp. 920–932, Mar. 2010, doi: 10.1002/adma.200901407.

[20] H. Qian *et al.*, “Mussel-inspired superhydrophilic surface with enhanced antimicrobial properties under immersed and atmospheric conditions,” *Appl. Surf. Sci.*, vol. 465, pp. 267–278, Jan. 2019, doi: 10.1016/j.apsusc.2018.09.173.

[21] D. Sharma, L. Misba, and A. U. Khan, “Antibiotics versus biofilm: an emerging battleground in microbial communities,” *Antimicrob. Resist. Infect. Control*, vol. 8, no. 1, p. 76, Dec. 2019, doi: 10.1186/s13756-019-0533-3.

[22] L. Dieltjens *et al.*, “Inhibiting bacterial cooperation is an evolutionarily robust anti-biofilm strategy,” *Nat. Commun.*, vol. 11, no. 1, p. 107, Dec. 2020, doi: 10.1038/s41467-019-13660-x.

[23] G. Feng, Y. Cheng, S.-Y. Wang, D. A. Borca-Tasciuc, R. W. Worobo, and C. I. Moraru, “Bacterial attachment and biofilm formation on surfaces are reduced by small-diameter nanoscale pores: how small is small enough?,” *Npj Biofilms Microbiomes*, vol. 1, no. 1, p. 15022, Dec. 2015, doi: 10.1038/npjbiofilms.2015.22.

[24] A. A. R. Watt, J. P. Bothma, and P. Meredith, “The supramolecular structure of melanin,” *Soft Matter*, vol. 5, no. 19, p. 3754, 2009, doi: 10.1039/b902507c.

[25] A. R. Katritzky, N. G. Akhmedov, S. N. Denisenko, and O. V. Denisko, “^{1} H NMR Spectroscopic Characterization of Solutions of *Sepia* Melanin, *Sepia* Melanin Free Acid and Human Hair Melanin,” *PIGMENT CELL Res.*, vol. 15, no. 2, pp. 93–97, Apr. 2002, doi: 10.1034/j.1600-0749.2002.1o062.x.

[26] F. A. Zucca *et al.*, “Neuromelanin of the Human Substantia Nigra: An Update,” *Neurotox. Res.*, vol. 25, no. 1, pp. 13–23, Jan. 2014, doi: 10.1007/s12640-013-9435-y.

[27] M. d’Ischia, A. Napolitano, A. Pezzella, P. Meredith, and T. Sarna, “Chemical and Structural Diversity in Eumelanins: Unexplored Bio-Optoelectronic Materials,” *Angew. Chem. Int. Ed.*, vol. 48, no. 22, pp. 3914–3921, May 2009, doi: 10.1002/anie.200803786.

[28] F. Solano, “Melanin and Melanin-Related Polymers as Materials with Biomedical and Biotechnological Applications—Cuttlefish Ink and Mussel Foot Proteins as Inspired Biomolecules,” *Int. J. Mol. Sci.*, vol. 18, no. 7, p. 1561, Jul. 2017, doi: 10.3390/ijms18071561.

[29] L. Panzella *et al.*, “Atypical Structural and π-Electron Features of a Melanin Polymer That Lead to Superior Free-Radical-Scavenging Properties,” *Angew. Chem. Int. Ed.*, vol. 52, no. 48, pp. 12684–12687, Nov. 2013, doi: 10.1002/anie.201305747.

[30] M. Brenner and V. J. Hearing, “The Protective Role of Melanin Against UV Damage in Human Skin†,” *Photochem. Photobiol.*, vol. 84, no. 3, pp. 539–549, May 2008, doi: 10.1111/j.1751-1097.2007.00226.x.

[31] Y. J. Kim, W. Wu, S.-E. Chun, J. F. Whitacre, and C. J. Bettinger, “Catechol-Mediated Reversible Binding of Multivalent Cations in Eumelanin Half-Cells,” *Adv. Mater.*, vol. 26, no. 38, pp. 6572–6579, Oct. 2014, doi: 10.1002/adma.201402295.

[32] Y. J. Kim *et al.*, “Evidence of Porphyrin-Like Structures in Natural Melanin Pigments Using Electrochemical Fingerprinting,” *Adv. Mater.*, vol. 28, no. 16, pp. 3173–3180, Apr. 2016, doi: 10.1002/adma.201504650.

[33] T. Repenko *et al.*, “Strong Photoacoustic Signal Enhancement by Coating Gold Nanoparticles with Melanin for Biomedical Imaging,” *Adv. Funct. Mater.*, vol. 28, no. 7, p. 1705607, Feb. 2018, doi: 10.1002/adfm.201705607.

[34] H. Cheng *et al.*, “Mussel-Inspired Multifunctional Hydrogel Coating for Prevention of Infections and Enhanced Osteogenesis,” *ACS Appl. Mater. Interfaces*, vol. 9, no. 13, pp. 11428–11439, Apr. 2017, doi: 10.1021/acsami.6b16779.

[35] Y. J. Kim, W. Wu, S.-E. Chun, J. F. Whitacre, and C. J. Bettinger, “Biologically derived melanin electrodes in aqueous sodium-ion energy storage devices,” *Proc. Natl. Acad. Sci.*, vol. 110, no. 52, pp. 20912–20917, Dec. 2013, doi: 10.1073/pnas.1314345110.

[36] M. Caldas, A. C. Santos, F. Veiga, R. Rebelo, R. L. Reis, and V. M. Correlo, “Melanin nanoparticles as a promising tool for biomedical applications – a review,” *Acta Biomater.*, vol. 105, pp. 26–43, Mar. 2020, doi: 10.1016/j.actbio.2020.01.044.

[37] E. Kim *et al.*, “Redox-Cycling and H_2O_2 Generation by Fabricated Catecholic Films in the Absence of Enzymes,” *Biomacromolecules*, vol. 12, no. 4, pp. 880–888, Apr. 2011, doi: 10.1021/bm101499a.

[38] E. Kim *et al.*, “Context-Dependent Redox Properties of Natural Phenolic Materials,” *Biomacromolecules*, vol. 15, no. 5, pp. 1653–1662, May 2014, doi: 10.1021/bm500026x.

[39] H. Liu *et al.*, “Bio-inspired redox-cycling antimicrobial film for sustained generation of reactive oxygen species,” *Biomaterials*, vol. 162, pp. 109–122, Apr. 2018, doi: 10.1016/j.biomaterials.2017.12.027.

[40] B. Liu, C. Zhou, Z. Zhang, J. D. Roland, and B. P. Lee, “Antimicrobial property of halogenated catechols,” *Chem. Eng. J.*, vol. 403, p. 126340, Jan. 2021, doi: 10.1016/j.cej.2020.126340.

[41] H. Meng *et al.*, “Biomimetic recyclable microgels for on-demand generation of hydrogen peroxide and antipathogenic application,” *Acta Biomater.*, vol. 83, pp. 109–118, Jan. 2019, doi: 10.1016/j.actbio.2018.10.037.

[42] C. Xu, J. Li, L. Yang, F. Shi, L. Yang, and M. Ye, “Antibacterial activity and a membrane damage mechanism of Lachnum YM30 melanin against Vibrio parahaemolyticus and Staphylococcus aureus,” *Food Control*, vol. 73, pp. 1445–1451, Mar. 2017, doi: 10.1016/j.foodcont.2016.10.048.

[43] P. Manivasagan, J. Venkatesan, K. Senthilkumar, K. Sivakumar, and S.-K. Kim, “Isolation and characterization of biologically active melanin from Actinoalloteichus sp. MA-32,” *Int. J. Biol. Macromol.*, vol. 58, pp. 263–274, Jul. 2013, doi: 10.1016/j.ijbiomac.2013.04.041.

[44] Y. Liang, Q. Han, N. Byrne, L. Sun, and X. Wang, “Recyclable One-Step Extraction and Characterization of Intact Melanin from Alpaca Fibers,” *Fibers Polym.*, vol. 19, no. 8, pp. 1640–1646, Aug. 2018, doi: 10.1007/s12221-018-8144-9.

[45] J. Ilavsky and P. R. Jemian, “*Irena* : tool suite for modeling and analysis of small-angle scattering,” *J. Appl. Crystallogr.*, vol. 42, no. 2, pp. 347–353, Apr. 2009, doi: 10.1107/S0021889809002222.

[46] D. Dębski *et al.*, “Mechanism of oxidative conversion of Amplex® Red to resorufin: Pulse radiolysis and enzymatic studies,” *Free Radic. Biol. Med.*, vol. 95, pp. 323–332, Jun. 2016, doi: 10.1016/j.freeradbiomed.2016.03.027.

[47] L. Xiao, R. Zhang, and W. Zhu, “The distribution of melanocytes and the degradation of melanosomes in fetal hair follicles,” *Micron*, vol. 119, pp. 109–116, Apr. 2019, doi: 10.1016/j.micron.2019.01.010.

[48] P. Meredith, B. J. Powell, J. Riesz, S. P. Nighswander-Rempel, M. R. Pederson, and E. G. Moore, “Towards structure–property–function relationships for eumelanin,” *Soft Matter*, vol. 2, no. 1, pp. 37–44, 2006, doi: 10.1039/B511922G.

[49] I.-E. Pralea *et al.*, “From Extraction to Advanced Analytical Methods: The Challenges of Melanin Analysis,” *Int. J. Mol. Sci.*, vol. 20, no. 16, p. 3943, Aug. 2019, doi: 10.3390/ijms20163943.

[50] T. Imai, K. Higuchi, Y. Yamamoto, S. Arai, T. Nakano, and N. Tanaka, “Sub-nm 3D observation of human hair melanin by high-voltage STEM,” *Microscopy*, vol. 65, no. 2, pp. 185–189, Apr. 2016, doi: 10.1093/jmicro/dfv372.

[51] I. Hurbain *et al.*, “Electron tomography of early melanosomes: Implications for melanogenesis and the generation of fibrillar amyloid sheets,” *Proc. Natl. Acad. Sci.*, vol. 105, no. 50, pp. 19726–19731, Dec. 2008, doi: 10.1073/pnas.0803488105.

[52] A. K. Chakraborty, J. T. Platt, K. K. Kim, B. Kwon, D. C. Bennett, and J. M. Pawelek, “Polymerization of 5,6-Dihydroxyindole-2-Carboxylic Acid to Melanin by the Pmel 17/Silver Locus Protein,” *Eur. J. Biochem.*, vol. 236, no. 1, pp. 180–188, Feb. 1996, doi: 10.1111/j.1432-1033.1996.t01-1-00180.x.

[53] C. M. R. Clancy and J. D. Simon, “Ultrastructural Organization of Eumelanin from *Sepia officinalis* Measured by Atomic Force Microscopy †,” *Biochemistry*, vol. 40, no. 44, pp. 13353–13360, Nov. 2001, doi: 10.1021/bi010786t.

[54] Z. Tian, W. Hwang, and Y. J. Kim, “Mechanistic understanding of monovalent cation transport in eumelanin pigments,” *J. Mater. Chem. B*, vol. 7, no. 41, pp. 6355–6361, 2019, doi: 10.1039/C9TB01211G.

[55] W. Xie *et al.*, “Natural Melanin/Polyurethane Composites as Highly Efficient Near-Infrared-Photoresponsive Shape Memory Implants,” *ACS Biomater. Sci. Eng.*, vol. 6, no. 9, pp. 5305–5314, Sep. 2020, doi: 10.1021/acsbiomaterials.0c00933.

[56] M. Thommes *et al.*, “Physisorption of gases, with special reference to the evaluation of surface area and pore size distribution (IUPAC Technical Report),” *Pure Appl. Chem.*, vol. 87, no. 9–10, pp. 1051–1069, Oct. 2015, doi: 10.1515/pac-2014-1117.

[57] Y. Liu *et al.*, “Comparison of Structural and Chemical Properties of Black and Red Human Hair Melanosomes¶,” *Photochem. Photobiol.*, vol. 81, no. 1, p. 135, 2005, doi: 10.1562/2004-08-03-RA-259.1.

[58] L.-F. Wang and J.-W. Rhim, “Isolation and characterization of melanin from black garlic and sepia ink,” *LWT*, vol. 99, pp. 17–23, Jan. 2019, doi: 10.1016/j.lwt.2018.09.033.

[59] N. E.-A. El-Naggar and S. M. El-Ewasy, “Bioproduction, characterization, anticancer and antioxidant activities of extracellular melanin pigment produced by newly isolated microbial cell factories Streptomyces glaucescens NEAE-H,” *Sci. Rep.*, vol. 7, no. 1, p. 42129, Mar. 2017, doi: 10.1038/srep42129.

[60] Q. Xing, P. Buono, D. Ruch, P. Dubois, L. Wu, and W.-J. Wang, “Biodegradable UV-Blocking Films through Core–Shell Lignin–Melanin Nanoparticles in Poly(butylene adipate- *co* -terephthalate),” *ACS Sustain. Chem. Eng.*, vol. 7, no. 4, pp. 4147–4157, Feb. 2019, doi: 10.1021/acssuschemeng.8b05755.

[61] W. Xie, E. Pakdel, D. Liu, L. Sun, and X. Wang, “Waste-Hair-Derived Natural Melanin/TiO_2 Hybrids as Highly Efficient and Stable UV-Shielding Fillers for Polyurethane Films,” *ACS Sustain. Chem. Eng.*, vol. 8, no. 3, pp. 1343–1352, Jan. 2020, doi: 10.1021/acssuschemeng.9b03514.

[62] M. Lozano, P. Rodríguez-Ulibarri, J. C. Echeverría, M. Beruete, M. Sorolla, and M. J. Beriain, “Mid-Infrared Spectroscopy (MIR) for Simultaneous Determination of Fat and Protein Content in Meat of Several Animal Species,” *Food Anal. Methods*, vol. 10, no. 10, pp. 3462–3470, Oct. 2017, doi: 10.1007/s12161-017-0879-1.

[63] S. A. Centeno and J. Shamir, “Surface enhanced Raman scattering (SERS) and FTIR characterization of the sepia melanin pigment used in works of art,” *J. Mol. Struct.*, vol. 873, no. 1–3, pp. 149–159, Feb. 2008, doi: 10.1016/j.molstruc.2007.03.026.

[64] V. Capozzi *et al.*, “Raman and optical spectroscopy of eumelanin films,” *J. Mol. Struct.*, vol. 744–747, pp. 717–721, Jun. 2005, doi: 10.1016/j.molstruc.2004.11.074.

[65] S. Ito, “Reexamination of the structure of eumelanin,” *Biochim. Biophys. Acta BBA - Gen. Subj.*, vol. 883, no. 1, pp. 155–161, Aug. 1986, doi: 10.1016/0304-4165(86)90146-7.

[66] E. Tacconelli *et al.*, “Discovery, research, and development of new antibiotics: the WHO priority list of antibiotic-resistant bacteria and tuberculosis,” *Lancet Infect. Dis.*, vol. 18, no. 3, pp. 318–327, Mar. 2018, doi: 10.1016/S1473-3099(17)30753-3.

[67] M. S. Orellano *et al.*, “Chitosan nanoparticles enhance the antibacterial activity of the native polymer against bovine mastitis pathogens,” *Carbohydr. Polym.*, vol. 213, pp. 1–9, Jun. 2019, doi: 10.1016/j.carbpol.2019.02.016.

[68] J. Qian, C. Pan, and C. Liang, “Antimicrobial activity of Fe-loaded chitosan nanoparticles,” *Eng. Life Sci.*, vol. 17, no. 6, pp. 629–634, Jun. 2017, doi: 10.1002/elsc.201600172.

[69] A. Sarwar, H. Katas, and N. M. Zin, “Antibacterial effects of chitosan–tripolyphosphate nanoparticles: impact of particle size molecular weight,” *J. Nanoparticle Res.*, vol. 16, no. 7, p. 2517, Jul. 2014, doi: 10.1007/s11051-014-2517-9.

[70] H. Liu *et al.*, “Role of polydopamine’s redox-activity on its pro-oxidant, radical-scavenging, and antimicrobial activities,” *Acta Biomater.*, vol. 88, pp. 181–196, Apr. 2019, doi: 10.1016/j.actbio.2019.02.032.

[71] E. Linley, S. P. Denyer, G. McDonnell, C. Simons, and J.-Y. Maillard, “Use of hydrogen peroxide as a biocide: new consideration of its mechanisms of biocidal action,” *J. Antimicrob. Chemother.*, vol. 67, no. 7, pp. 1589–1596, Jul. 2012, doi: 10.1093/jac/dks129.

[72] J. A. Imlay and S. Linn, “Bimodal pattern of killing of DNA-repair-defective or anoxically grown Escherichia coli by hydrogen peroxide.,” *J. Bacteriol.*, vol. 166, no. 2, pp. 519–527, 1986, doi: 10.1128/JB.166.2.519-527.1986.

[73] M. Exner *et al.*, “Antibiotic resistance: What is so special about multidrug-resistant Gram-negative bacteria?,” *GMS Hyg. Infect. Control 12Doc05*, Apr. 2017, doi: 10.3205/DGKH000290.

[74] Z. Breijyeh, B. Jubeh, and R. Karaman, “Resistance of Gram-Negative Bacteria to Current Antibacterial Agents and Approaches to Resolve It,” *Molecules*, vol. 25, no. 6, p. 1340, Mar. 2020, doi: 10.3390/molecules25061340.

[75] M. Hayyan, M. A. Hashim, and I. M. AlNashef, “Superoxide Ion: Generation and Chemical Implications,” *Chem. Rev.*, vol. 116, no. 5, pp. 3029–3085, Mar. 2016, doi: 10.1021/acs.chemrev.5b00407.

[76] A. B. Mostert, S. B. Rienecker, C. Noble, G. R. Hanson, and P. Meredith, “The photoreactive free radical in eumelanin,” *Sci. Adv.*, vol. 4, no. 3, p. eaaq1293, Mar. 2018, doi: 10.1126/sciadv.aaq1293.

[77] Z. Zhang *et al.*, “Iron Magnetic Nanoparticle-Induced ROS Generation from Catechol-Containing Microgel for Environmental and Biomedical Applications,” *ACS Appl. Mater. Interfaces*, vol. 12, no. 19, pp. 21210–21220, May 2020, doi: 10.1021/acsami.9b19726.

[78] A. Lampel *et al.*, “Polymeric peptide pigments with sequence-encoded properties,” *Science*, vol. 356, no. 6342, pp. 1064–1068, Jun. 2017, doi: 10.1126/science.aal5005.

[79] W.-Z. Qiu, H.-C. Yang, and Z.-K. Xu, “Dopamine-assisted co-deposition: An emerging and promising strategy for surface modification,” *Adv. Colloid Interface Sci.*, vol. 256, pp. 111–125, Jun. 2018, doi: 10.1016/j.cis.2018.04.011.

[80] K.-Y. Ju, Y. Lee, S. Lee, S. B. Park, and J.-K. Lee, “Bioinspired Polymerization of Dopamine to Generate Melanin-Like Nanoparticles Having an Excellent Free-Radical-Scavenging Property,” *Biomacromolecules*, vol. 12, no. 3, pp. 625–632, Mar. 2011, doi: 10.1021/bm101281b.

[81] D. Wei *et al.*, “Graphene from electrochemical exfoliation and its direct applications in enhanced energy storage devices,” *Chem Commun*, vol. 48, no. 9, pp. 1239–1241, 2012, doi: 10.1039/C2CC16859F.

[82] L. C. Capozzi, F. M. Mehmood, M. Giagnorio, A. Tiraferri, M. Cerruti, and M. Sangermano, “Ultrafiltration Membranes Functionalized with Polydopamine with Enhanced Contaminant Removal by Adsorption,” *Macromol. Mater. Eng.*, vol. 302, no. 5, p. 1600481, May 2017, doi: 10.1002/mame.201600481.

[83] I. S. Kwon, Y. J. Kim, L. Klosterman, M. Forssell, G. K. Fedder, and C. J. Bettinger, “In vitro electrochemical characterization of polydopamine melanin as a tissue stimulating electrode material,” *J. Mater. Chem. B*, vol. 4, no. 18, pp. 3031–3036, 2016, doi: 10.1039/C5TB02618K.

[84] J. Luo, A. S. Meyer, R. V. Mateiu, D. Kalyani, and M. Pinelo, “Functionalization of a Membrane Sublayer Using Reverse Filtration of Enzymes and Dopamine Coating,” *ACS Appl. Mater. Interfaces*, vol. 6, no. 24, pp. 22894–22904, Dec. 2014, doi: 10.1021/am507308k.

CHAPTER 3
Melanin zinc complex as a biocompatible agent for clearing bacteremia

3.1 Introduction

Sepsis is a severe whole-body inflammation caused by an extreme immune response to bacterial infection of the blood, often leading to organ dysfunction and even death [1], [2]. Worldwide, 49 million cases of sepsis were reported each year, of which an estimated 11 million patients ultimately died from complications related to septic shock [3]. Due to an aging population, increased use of invasive procedures, and immunosuppressive therapies, including cancer chemotherapy and organ transplantation, sepsis has become one of the leading causes of death in adults and infants in the United States [4]. Current therapies rely on the use of broad-spectrum antibiotics before the pathogen is identified, raising concerns for the disruption of natural microbiome balance and antimicrobial resistance [5]. Even in the case of effective antibiotic therapy against gram-negative bacteria, the outer cellular membranes of dead bacteria release negatively charged and reactive endotoxins such as lipopolysaccharides (LPS) [6]. LPS can initiate the sepsis inflammatory cascade, resulting in multiorgan failure, septic shock, and death [7]. Based on these observations, targeted separation of LPS and the bacteria from the blood can complement conventional antibiotic therapy.

Successful removal of LPS and bacteria from the patient blood can be accomplished using an extracorporeal blood-cleaning device that specifically targets the endotoxin and/or bacteria. [8], [9]. Such devices include hemoperfusion and microfluidic-magnetic apparatuses which are

designed to draw the patients' blood and selectively remove bacteria/endotoxins in the filtration unit [10]. The filtration relies on the specific binding using antibodies, engineered proteins, or synthetic molecules incorporated in the membrane [11]. For example, antibodies against bacterial cell membrane were immobilized on the surface of magnetic micro/nanoparticles for the specific binding with bacteria in microfluidic devices. In another study, an innate immune protein, mannose-binding lectin (MBL), was used for the recognition of bacteria and endotoxin [12]. MBL was fused with the Fc region of antibody and immobilized on a membrane surface to capture bacteria and endotoxin [7]. In another example, a zinc-chelating synthetic molecule, bis-dipicolylamine (bis-DPA), which mimics the structure of annexin V, was immobilized on magnetic nanoparticles for the rapid removal of bacteria and endotoxin from blood [4]. Despite the promising research and development, there are inherent limitations to these methods. The antibody-based methods have a very low separation speed as they rely on highly specific antibody-antigen interactions. Additionally, protein-based methods including the fused MBL are associated with high production costs and show challenges in storage and quality control.

In this Chapter, we demonstrate that naturally occurring melanin pigments loaded with zinc ions may serve as active material in separating LPS and bacteria from blood. Melanins are the class of multifunctional biopolymers that can be found throughout nature [13]. As the most ubiquitous form of melanins, eumelanins (hereafter called melanins for simplicity) is primarily composed of subunits of 5,6-dihydroxyindole (DHI) and 5,6-dihydroxyindole-2-carboxylic acid (DHICA) monomers in various ratios that are π-stacked to form homogeneous nanoparticles [14]. It is highly biocompatible and has many favorable physical and chemical properties [15]. Melanins contain diverse chemical functional groups including pendant carboxylic acids, aromatic amines, and catechols. Redox-active catechols are oxidized into ortho(*o*)-quinones by losing two electrons,

and two protons [16]. During the redox reaction, catechols can form coordination bonding with protons, and ions [17]. This electrochemical feature has enabled melanins to be used in aqueous charge storage devices with divalent cations [18]. Here, we show a novel approach leveraging melanin redox reactions to immobilize zinc ions (Zn^{2+}) and bind to bacteria and endotoxin from blood. Zn^{2+} largely exhibits a stronger affinity toward negatively charged molecules compared to other divalent cations, (e.g. Mg^{2+} or Ca^{2+}) due to the presence of a filled d-orbital [19]. Zn^{2+} plays an import role as an anion receptor in biological systems, particularly associated with phosphate derivatives [20]. This property, initially described in metalloenzymes with high phosphate selectivity, allows phosphates to act as substrates or inhibitors by reversible binding to Zn^{2+} in the active site [21]. The interactions between Zn^{2+} and phosphates have been utilized to develop biological assays to detect apoptotic cells and bacteria [21], [22]. Subsequently, we hypothesize that Zn^{2+}-loaded melanins (Mel-Zn) would form a coordination bond with anionic phospholipid groups in LPS that exists as either a component of the outer membrane of gram-negative bacteria or a freely circulating molecule. Simple and cost-effective preparation of Mel-Zn along with rapid binding kinetics would make its clinical application plausible for the extracorporeal blood-cleansing device.

3.2 Materials and methods

3.2.1 Preparation of Mel-Zn

Melanin isolated from *Sepia officinalis* (Sigma-Aldrich, St. Louis, MO USA) was suspended in ethanol (5 wt%) and sonicated using 80 W of power for 5 min using a probe sonicator (Digital Sonifier SFX 550, Branson, Brookfield, CT USA). Melanin suspension was filtered using filter paper (Grade 41, Whatman, Fisher Scientific, Pittsburgh, PA USA) and dried at 100 °C for 2 h in a vacuum oven. Polytetrafluoroethylene (PTFE) (Good Fellow, Cambridge, England)) was blended with melanin in a 2:8 mass ratio using an agate mortar and pestle (Mel). Zinc ion (Zn^{2+}) loaded melanin was prepared using electrochemical, and solution methods. Melanin (70 mg) were pressed into stainless steel mesh current collector (Type 304, McMaster-Carr, Cleveland, OH USA) using a hydraulic press (P = 4 metric tons). A three-electrode cell was configured with melanin, platinum wire and Ag/AgCl as working, counter, and reference electrodes, respectively. A multichannel potentiostat-galvanostat (VMP3, Biologic, Knoxville, TN USA) was used to measure Cyclic voltammetry (CV) profiles. CV experiments were performed in the aqueous electrolyte of 0.5 M $Zn(NO_3)_2$ at a scan rate of 5 mV/s . Mel-Zn_{CV} was collected after 5 cycles of CV and stopped after the oxidation cycle. The sample was dried at 100 °C for 1 h in a vacuum oven and stored in ambient conditions. In the second method, Zn^{2+} loading was performed by immersing melanin (50 mg) into 10 ml solutions of 0.1 and 0.05 M $Zn(NO_3)_2$ at room temperature for 3 h. After washing twice with dd-H_2O, Zn^{2+} loaded melanin samples (Mel-$Zn_{0.1}$ and Mel-$Zn_{0.05}$) were dried at 100 °C for 1 h in a vacuum oven and stored in ambient conditions.

3.2.2 Materials characterization

X-ray photoelectron spectroscopy was performed using the Kratos Axis Supra XPS (Axis Supra XPS, Manchester, U.K.). Survey and high-resolution spectra of zinc (Zn) was obtained using aluminum (Al) source and were further analyzed by CasaXPS software. Elemental analysis was done by determining the peak areas and taking in to account the relative sensitivity factors of the instrumentation to individual atomic species.

Raman spectra of Mel and Mel-Zn were collected using an AFM-Raman microscope (NTEGRA Spectra, NT-MDT Spectrum Instruments, Moscow, Russia) with a 10X objective and 500 nm wavelength laser over a Raman shift range of 800–2500 cm^{-1}. To minimize sample degradation and maximize the signal-to-noise ratio, data from five separate scans using 1 mW of laser power and 10 s exposure time were averaged. Raman peaks were deconvolved using automatic multiple peak fit methods and Voigt function (Originlab, Northampton, MA USA).

Transmission electron microscopy was performed to analyze the shape and structure of melanin using JEOL JEM 2100 LaB6 (JEM 2100 LaB6, Peabody, MA USA). The particle solution was deposited on a carbon coated TEM grid (Structure Probe, Inc., West Chester, PA). Once the surface of the grid dried, it was transferred to the TEM grid holder and examined without staining. The acceleration voltage was set to 200 kV. All images were collected via the CCD camera attached to the TEM.

3.2.3 LPS binding assay

Endotoxin removal capacity of Mel-Zn was measured by chromogenic Limulus amoebocyte lysate (LAL) assay (ThermoFisher Scientific, Waltman, MA USA). Briefly, 2, 5 and 10 mg/ml of Mel-Zn samples were incubated with 1 EU/ml (EU = endotoxin unit) *Escherichia*

coli LPS endotoxin standard (011: B4) at 37 ℃. After 1 h, remaining endotoxin in the solution was measured by addition of 50 µl LAL reagent and 100 µl chromogenic substrate solution and incubation for 10 and 6 min at 37 ℃, respectively. After incubation, 100 ml of the stop reagent (acetic acid, 25 % v/v in water) was added, and absorbance was measured at 405 nm on a microplate reader. LPS concentration in the sample solutions was determined using a known standard calibration curve [23].

3.2.4 Bacteria binding efficiency

Binding of Mel-Zn to bacteria was evaluated using a gram-negative *E. coli* strain (ATCC®15597™). Prior to each binding test, *E. coli* was streaked from a frozen glycerol stock onto lysogeny broth (LB) agar. A single colony of *E. coli* was collected from the LB plate and inoculated in 5 mL of LB liquid medium at 37°C in shaking condition. After 15-16 hours, bacterial density was determined by means of optical density (OD) at 600 nm and adjusted to 5×10^5 CFU/ml (CFU = Colony forming unit). Five mg of Mel-Zn complexes were inoculated with bacteria suspension in PBS and animal whole blood at 37 ℃ for 1 h in shaking condition. Aliquots of the samples were serially diluted and plated on LB agar for overnight incubation at 37°C. Visible colonies were counted and compared with the negative control which was grown without Mel-Zn to evaluate the bacteria removal efficiencies.

3.2.5 Protein recovery

Bovine serum albumin (BSA) was used as model protein to evaluate protein adsorption by Mel-Zn complexes. Mel and Mel-Zn (5 mg/ml) were incubated with 1000, 500, and 20 µg/ml BSA at 37 ℃. After 1h, BSA concentrations in the solutions were determined using Pierce BCA protein

assay kit (ThermoFisher Scientific, Waltman, MA US). BSA recovery was calculated based on comparing BSA concentration in solution before and after being incubated with Mel or Mel-Zn.

3.2.6 Coagulation activation

Human Thrombin-Antithrombin Complex (TAT) *in vitro* enzyme-linked immunosorbent assay (ELISA) (Abcam INC, Waltham, MA USA) was used for quantitative measurement of TAT complex concentrations in plasma. Blood coagulation was characterized by incubating 5 mg Mel and Mel-Zn in 300 µl human whole blood containing heparin as an anticoagulant. After 30 min incubation at 37 ℃ blood was centrifuged at 3000 g for 10 min and supernatant containing plasma was collected. Standards and plasma samples were added to the wells of a precoated 96-well plate with TAT specific antibodies and washed with wash buffer after 2 h incubation. Afterward a TAT specific biotinylated detection antibody is added and then followed by washing with wash buffer. Next streptavidin-peroxidase conjugate was added, and unbound conjugates was washed away with wash buffer. Chromogen substrate was then used to visualize Streptavidin-Peroxidase enzymatic reaction. Chromogen substrate is catalyzed by Streptavidin-Peroxidase to generate a blue color which changes into yellow after adding acidic stop solution. The absorbance was measured at a wavelength of 540 nm. TAT concentration in the sample solutions was determined using a known standard calibration curve.

3.2.7 Hemolysis ratio

To evaluate hemolytic potential, 5 mg of Mel and Mel-Zn were incubated with 1 ml animal red blood cells (2×10^8 cell/ml) for 30 min and then centrifuged at 900 rcf for 5 min to separate the supernatant. The absorbance of the supernatant was measured at a wavelength of 540 nm. PBS

solution and distilled water were used as negative (0 % lysis) and positive controls (100 % lysis), respectively. The hemolysis ratio will be calculated using the following equation:

$$Hemolysis\ ratio\ \% = \frac{A_s - A_{nc}}{A_{pc} - A_{nc}} \times 100$$

where A_s, A_{nc}, and A_{pc} represent absorbance of the samples, negative control and positive control, respectively.

3.2.8 Statistical analysis

All data were presented as mean ± standard deviation (SD). Each result is average of three parallel experiments. The statistical significance was analyzed using one-way ANOVA. (*p < 0.05, *p < 0.01, ***p < 0.001).

3.3 Results and discussion

3.3.1 Preparation and characterization of Mel-Zn

As a major structural component of the outer membrane of gram-negative bacteria, LPS has high density of anionic phospholipids and has long been recognized as a key factor in septic shock in humans [24]. LPS is an amphipathic molecule with a general structure consisting of three defined regions: lipid A, core oligosaccharide, and O-antigen (**Figure 3.1**). Lipid A is most often composed of a dimer of glucosamine (GlcN) attached to acyl chains (fatty acids) by ester or amide linkages and normally contains phosphate groups on each GlcN [3], [25]. Lipid A is covalently attached to anionic groups, 2-keto-3-deoxyoctanic acid (Kdo) in the core region together with L-glycero-D-manno-heptose (Hep) and hexoses [25]. The O-antigen is a repeating oligosaccharide unit, which determines the strain-specific serological identity of the respective bacterium [25]. Although both the polysaccharide regions and lipid A can induce immune responses, the latter is the most immunogenic and considered the endotoxin center of LPS [26]. The core oligosaccharide of LPS largely consists of phosphorylated or phosphate-containing groups, such as pyrophosphate or 2-aminoethylphosphate. Our hypothesis was that rapid formation of coordination bonding between these phosphates and Zn^{2+} would facilitate the separation of LPS.

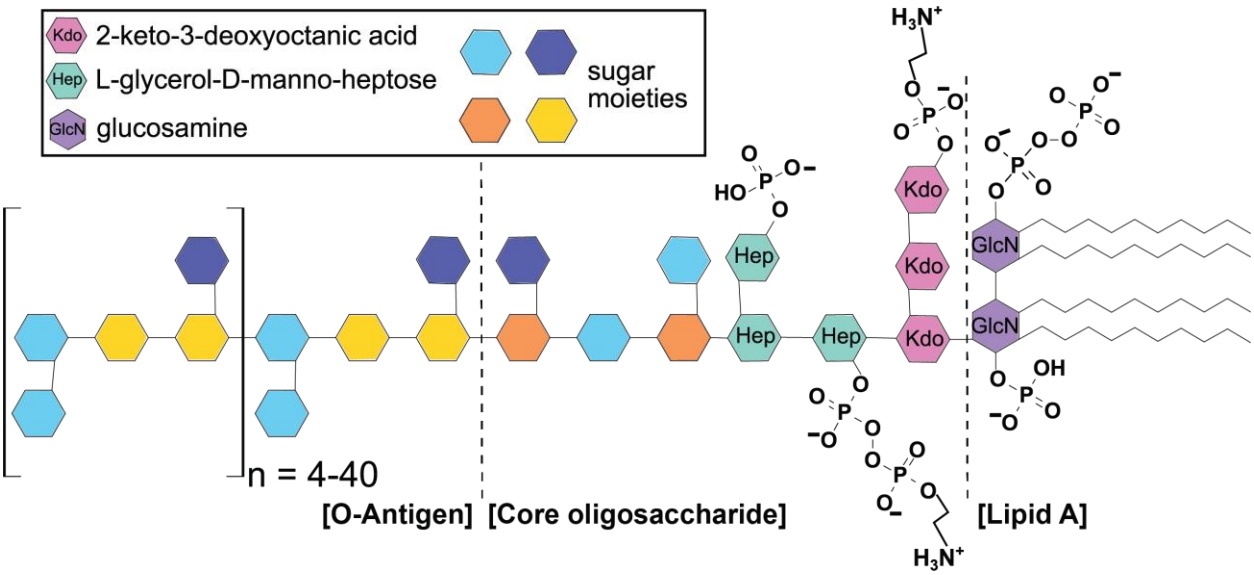

Figure 3.1: Chemical structure of Lipopolysaccharide (LPS) from *E. coli* O111:B4. LPS is characterized by three main units: Lipid A, Core oligosaccharide and O-Antigen. Lipid A is critical to endotoxin activity of LPS [25], [27]. High density of negatively charged phosphate groups are observed from oligosaccharide and Lipid A regions.

Melanin extracted from *Sepia officinalis* exhibits homogeneous nanoparticle aggregates with a characteristic length of 80-120 nm in diameter (**Figure 3.2(a)**). Spherical microstructures contain layers of protomolecules that are π-stacked with an intermolecular spacing of 3.8 Å. The presence of ordered protomolecules of melanin in mesoscale has been corroborated by computational simulation [13], [28]. Catechols present in melanin can reversibly bind multivalent ions such as Mg^{2+}, Ca^{2+}, $Fe^{2+/3+}$ or Zn^{2+} by undergoing redox reaction induced by two electrons and two protons [18], [29]. Catechols largely exhibit a stronger affinity for multivalent ions (0.95 eV) than oxidized *o*-quinones (0.23 eV). Concerted redox reactions, differential cation binding affinity, and nanostructure collectively promote the multivalent ion insertion and release in melanins [18], [30].

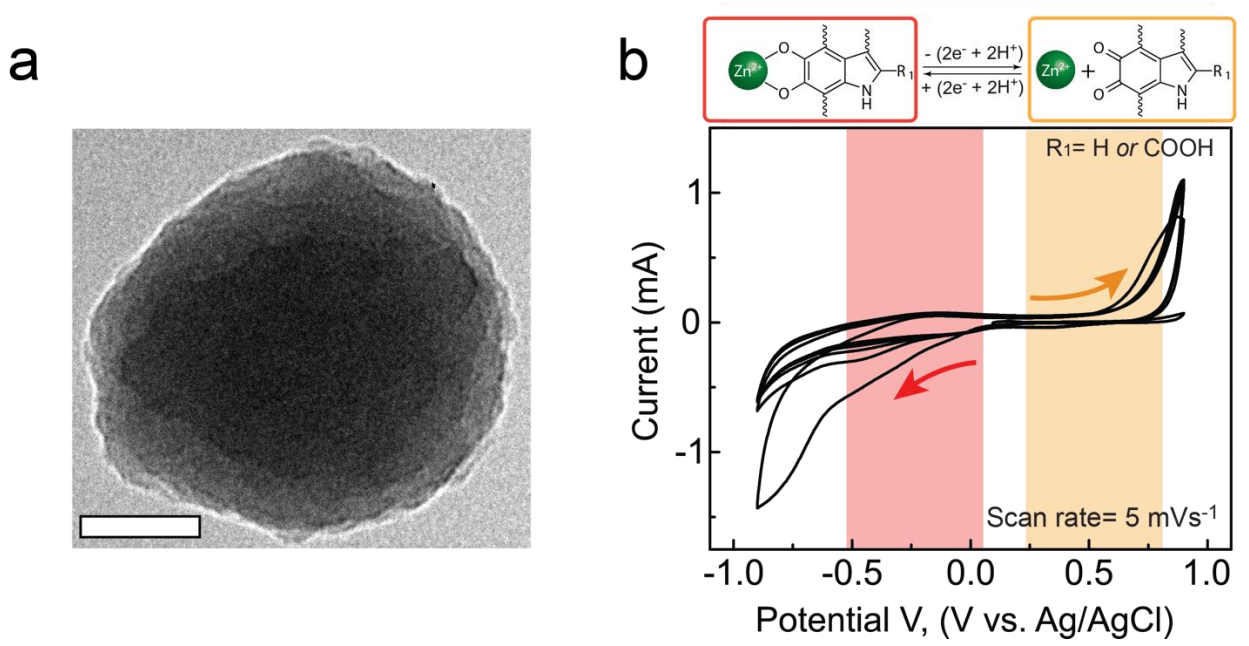

Figure 3.2: (a) Transmission electron microscopy (TEM) shows the microstructure of melanins. Scale bar indicates 50 nm. Zinc ions are electrochemically incorporated in melanin using cyclic voltammetry (CV) over five cycles as shown in (b). CV was performed in 0.5 M $Zn(NO_3)_2$ at a scan rate of 5 mV/s. The cathodic region corresponds to simultaneous Zn^{2+} removal and oxidation of catechols to o-quionones. Zinc ions can form coordination bonding at the anodic region during the electrochemical reduction from o-quinone to catechol.

The electrochemical behavior of melanins in Zn-containing solution was measured by cyclic voltammetry (CV, **Figure 3.2(b)**). Due to low number of cycles (5 cycles) no significant peak was observed from both anodic and cathodic regions [17]. Incorporation of zinc ion with melanin occurs when *o*-quinones of melanins are reduced by the addition of two electrons and two protons at the anodic region, generating Zn^{2+}-loaded melanin (Mel-Zn_{CV}). Conversely, in the cathodic region, Zn^{2+} is removed from melanins during the oxidation reaction from catechols to *o*-quinone. In this process, Zn^{2+} will form a coordination bond with melanin and there is no ion exchange; therefore, it exists as a zinc cation. Running the multiple redox cycles assists in increasing the amount of zinc loading in melanin by making more catechols accessible during the

repeated redox reaction. To compare the binding efficiency of electrochemically prepared Mel-Zn_{CV}, Zn^{2+}-loaded melanin was prepared by incubating melanin in a zinc solution at 0.1 and 0.05 M, resulting in Mel-$Zn_{0.1}$, and Mel-$Zn_{0.05}$.

The successful loading of zinc ions in melanin was assessed by X-ray photoelectron spectroscopy (XPS) and Raman spectroscopy (**Figure 3.3, 3.4, 3.5, and 3.6**). The presence of zinc ions loaded in melanin was probed by comparing Zn 2p peaks in the XPS survey (**Figure 3.3(a)**). Mel-Zn_{CV} contained 8 x 10^{-3} Zn/C, which is approximately two times higher zinc density than Mel-$Zn_{0.1}$ and Mel-$Zn_{0.05}$ (**Figure 3.3(b)**). In addition, high resolution Zn 2p peaks shown in **Figure 3.4** further confirm zinc coupling in melanin with defined peaks for Mel-Zn samples, which are absent in pristine melanin. Detailed peak positions of high-resolution Zn 2p peaks are summarized in **Table 3.1**.

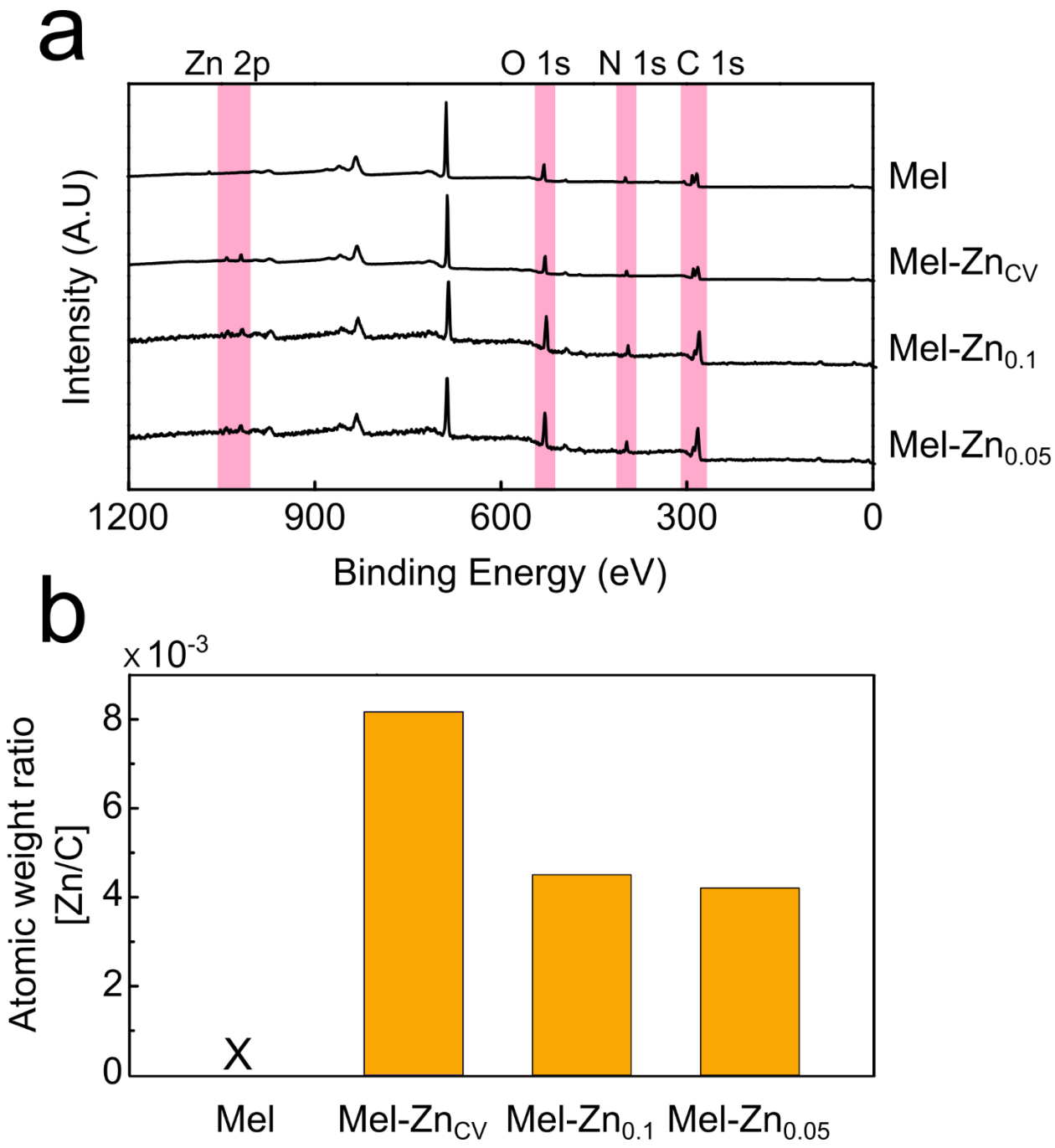

Figure 3.3: (a) XPS survey peaks for pristine melanin (Mel) and Zn^{2+}-loaded melanins (Mel-Zn_{CV}, Mel-$Zn_{0.1}$, and Mel-$Zn_{0.05}$). (b) Zn^{2+} incorporation was demonstrated by comparing the atomic weights of Zn 2p and C 1s peaks. Zn/C atomic weight ratio indicates Mel-Zn_{CV} exhibits approximate 2x higher binding density of Zn than Mel-$Zn_{0.1}$ and Mel-$Zn_{0.05}$.

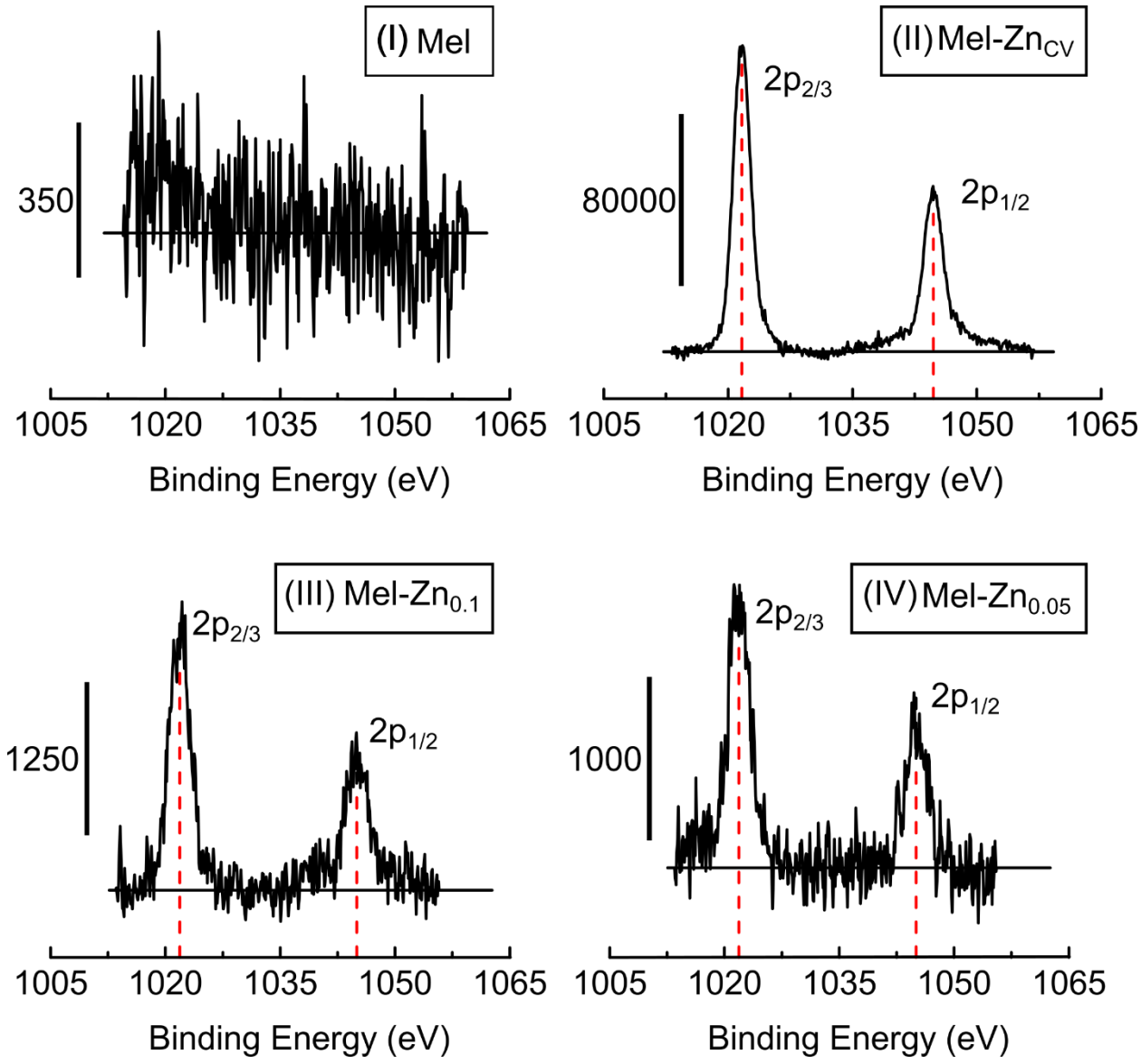

Figure 3.4: High-resolution XPS Zn 2p peaks show more detailed peak comparisons. Detailed peak positions are summarized in Table 3.1.

Table 3.1: Summary of high resolution XPS analysis of Zn 2p peak for Mel and Mel-Zn.

	Binding energy, eV
	Zn 2p
Mel-Zn_{CV}	1021.65 [Zn $2p_{3/2}$] 1044.76 [Zn $2p_{1/2}$]
Mel-$Zn_{0.1}$	1021.87 [Zn $2p_{3/2}$] 1045.01 [Zn $2p_{1/2}$]
Mel-$Zn_{0.05}$	1021.88 [Zn $2p_{3/2}$] 1045.04 [Zn $2p_{1/2}$]
Mel	– –

Pristine and Zn-loaded melanins show Raman spectra comparable to other sp^2-hybridized carbon materials [31] (**Figure 3.5**). Raman spectra were deconvolved into five peaks (α-ε) corresponding to carbon-carbon bonds of melanin subunits, DHI or DHICA [16], [31] (**Table 3.2**). Peak shift comparison from Raman spectra has been used to evaluate the potential locations of ion loading in melanin subunits compared to the pristine melanin. All deconvolved peaks of Zn-loaded melanins demonstrated peak shifts. The highest peak shift was found from α, which corresponds to the carboxylic acid of DHICA (**Figure 3.6**). This region can also be regarded as the location where the subunits polymerize to form a macromolecule such as the tetramer shown in **Figure 3.6(d)**. Compared to the planar indole backbones, the polymer bond formed among the subunits can be considered to be relatively weak, which results in the highest peak shifts observed from the α band (**Figure 3.6(d)**). This suggests that Zn^{2+} binds to the catechol during electrochemical redox process by CV, promoting the structural reconfiguration in mesoscale. Taken together, Zn-binding was corroborated by both XPS and Raman and higher density of Zn^{2+}

occurred during electrochemical loading compared to the spontaneous loading in aqueous zinc solutions.

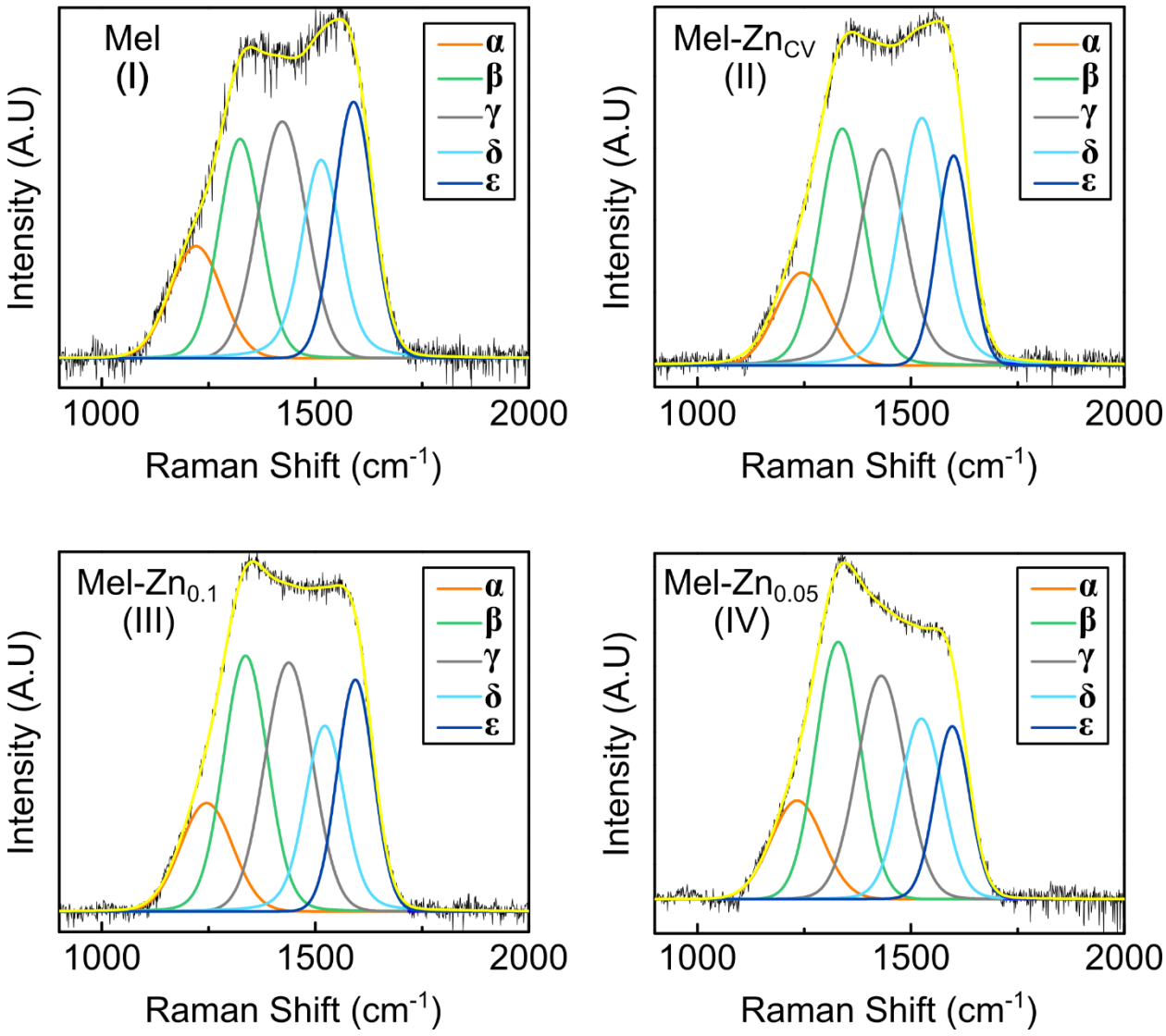

Figure 3.5: Raman spectra of Mel and Mel-Zn are deconvolved into five bands (α-ε) using a Voigt function. Black lines represent the raw XPS spectra as recorded. Peak fitting and deconvolution were performed by CasaXPS and represented by different line colors. Detailed peak positions are summarized in Table 3.2.

Table 3.2: Peak positions of Raman spectra of Mel and Mel-Zn are shown after the deconvolution using Voigt function.

Vibration mode and main functional groups	**Peak position [cm^{-1}]**			
	Mel-Zn_{CV}	Mel-$Zn_{0.1}$	Mel-$Zn_{0.05}$	Mel
(α) C–O stretching in carboxylic acid and C–OH	1245.58758	1245.38174	1233.432	1220.38463
(β) stretching vibration of aromatic C–N in indole	1339.22241	1336.65228	1329.66047	1323.63799
(γ) pyrrole ring stretching	1432.51518	1437.61442	1430.48443	1422.47989
(δ) stretching vibration of C=N in semiquinone and bending vibration of N–H	1525.7027	1522.23258	1524.44646	1513.56871
(ε) stretching vibration of aromatic C=C in indole	1600.08169	1593.85551	1596.7694	1589.42381

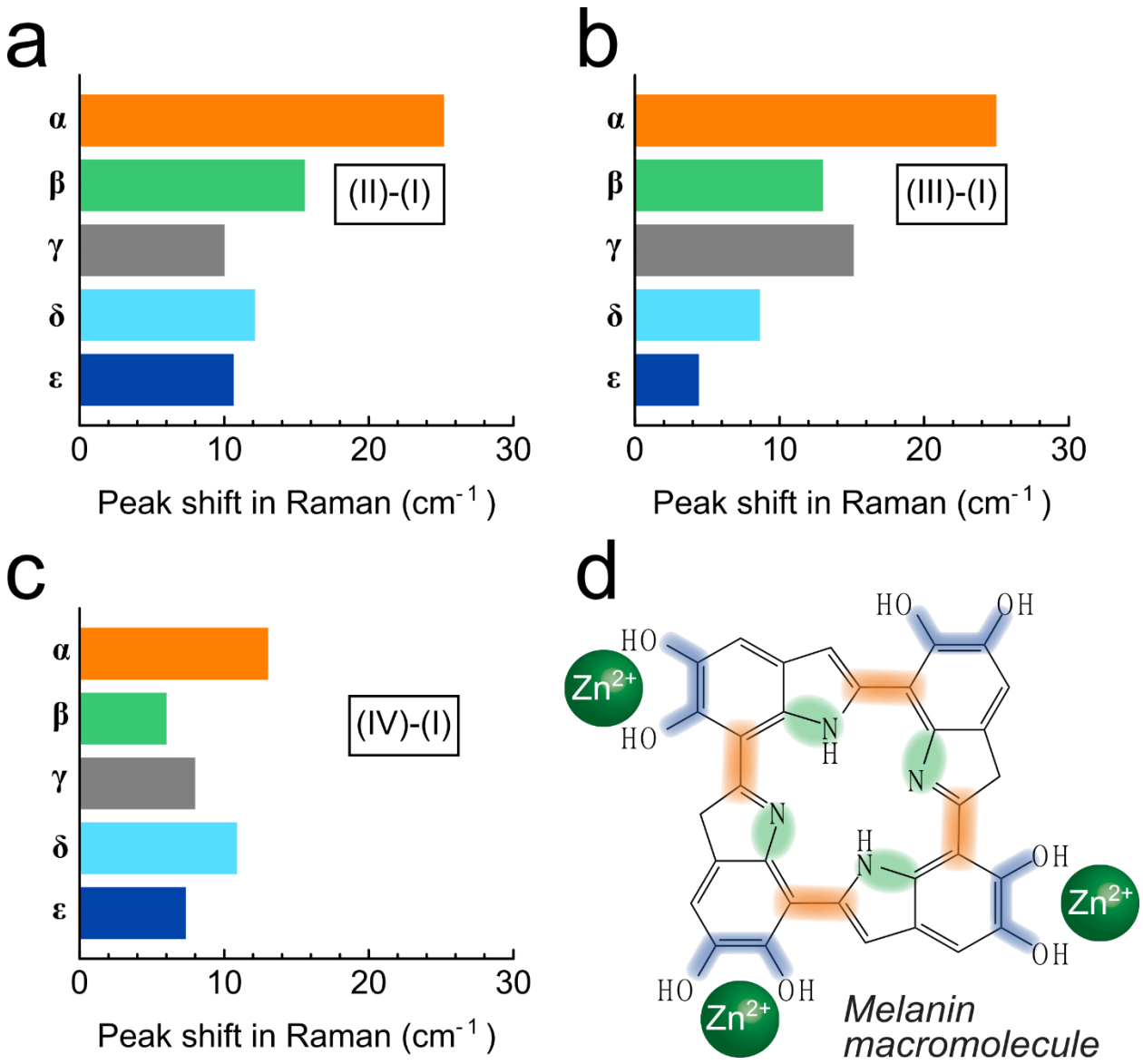

Figure 3.6: (a-c) Peak shifts of (II-IV) Mel-Zn relative to (I) Mel demonstrates that the macromolecular structure of melanin is reconfigured in mesoscale by Zn^{2+} loading (d).

3.3.2 LPS and bacteria binding

Rapid initiation of appropriate antibiotic therapy is critical for patients with sepsis or septic shock. A microbiologically confirmed diagnosis is necessary for pathogen targeted antibiotic therapy. However, because culture-based diagnostics require several days to be completed, broad-spectrum antibiotic therapy is often recommended as soon as possible after recognition of sepsis or septic shock [5]. In cases of antibiotic-resistant pathogens, or to reduce the risk of antibiotic resistance development, direct removal of pathogens from the blood via purification techniques could be an effective alternative strategy to treat septic patients [7], [12], [32].

Among culture-positive septic patients, 62.2% have gram-negative bacteria, of which, approximately 20% are infected with *Escherichia coli* [33]. Thus, an infection model of sepsis in PBS and whole blood was established using *E. coli* at a concentration of 5×10^5 CFU/ml (CFU = Colony forming unit). Removal of *E. coli* from the PBS was studied by incubating Mel and Mel-Zn in *E. coli* solutions for 1h and comparing the number of remaining *E. coli* with the negative control. As shown in **Figure 3.7(a)**, Mel-Zn_{CV} attained the highest efficiency of *E. coli* removal with 87.45±16% in PBS while Mel-$Zn_{0.1}$ and Mel-$Zn_{0.05}$ showed 69.41±16.3% and 28.82±7.4% *E. coli* removal efficiencies. The bacteria concentration in culture positive sepsis patients is much lower (1 to 10 CFU/ml) than the initial concentration used in this study [34]. However, the culture-based methods of measuring these concentrations only account for live bacterial cells, which does not include the potential impact of dead bacteria or associated debris. Accordingly, the concentration of pathogen in our study was selected to be higher than what would be seen in natural blood infection.

Next, it was tested if Mel-Zn could remove bacteria from whole blood by 1h incubation of Mel-Zn in the whole blood with *E. coli* (5×10^5 CFU/ml). Mel-Zn_{CV} attained 90.6±4 % removal

of *E. coli* while Mel-$Zn_{0.1}$ and Mel-$Zn_{0.05}$ achieved 67.69±7.9 %, and 30.39±1.2 % removal, respectively (**Figure 3.7(b)**). These results demonstrate that Mel-Zn can bind to bacteria in whole blood as well as PBS despite more complex cellular and molecular compositions of the whole blood.

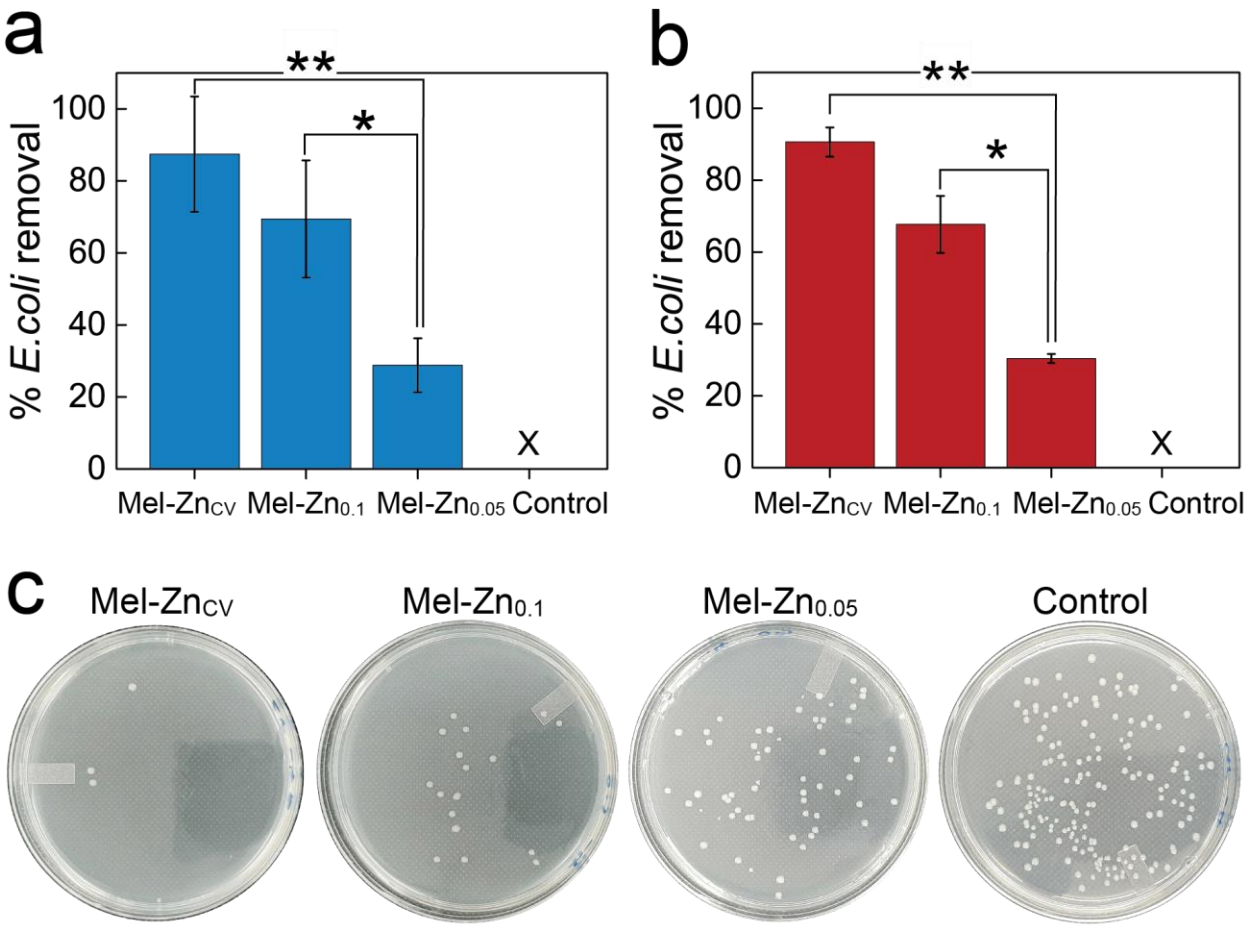

Figure 3.7: *E. coli* (5 x 10^5 CFU/ml) removal efficiency are shown for Zn^{2+}-loaded melanins (5 mg/ml) after 1 h incubation in PBS solution (a) and animal whole blood (b) at 37 ^{o}C. (c) Digital images of agar plates after incubating Mel-Zn in animal whole blood with *E. coli*. X indicates zero percent. Data are presented as mean ± SD, n = 3. $^{n.s.}p > 0.05$, *$p < 0.05$, and **$p < 0.01$.

As gram-negative bacteria die under the antibiotic treatment, a large amount of LPS can be released into the blood. This could be highly detrimental as LPS can trigger release of inflammatory cytokines that drive the sepsis cascade. As such, many patients do not respond to antibiotics alone since they only target the microbes [7]. Mel-Zn exhibit exceptional LPS removal efficiencies (**Figure 3.8)**. After 1h incubation with LPS (1 EU/mL) in PBS, Mel-Zn_{CV} at concentrations of 10 mg/ml and 2 mg/ml removed 100% and 85.56±10.4% of LPS, respectively. Likewise, Mel-$Zn_{0.1}$ and Mel-$Zn_{0.05}$ at the higher concentration of 10 mg/ml achieved LPS removal of 95.83±8% and 78.55±7.4%, respectively, while at 2 mg/ml concentration, LPS removal was reduced to 57.35±8.9% and 44.99±11.3%, respectively.

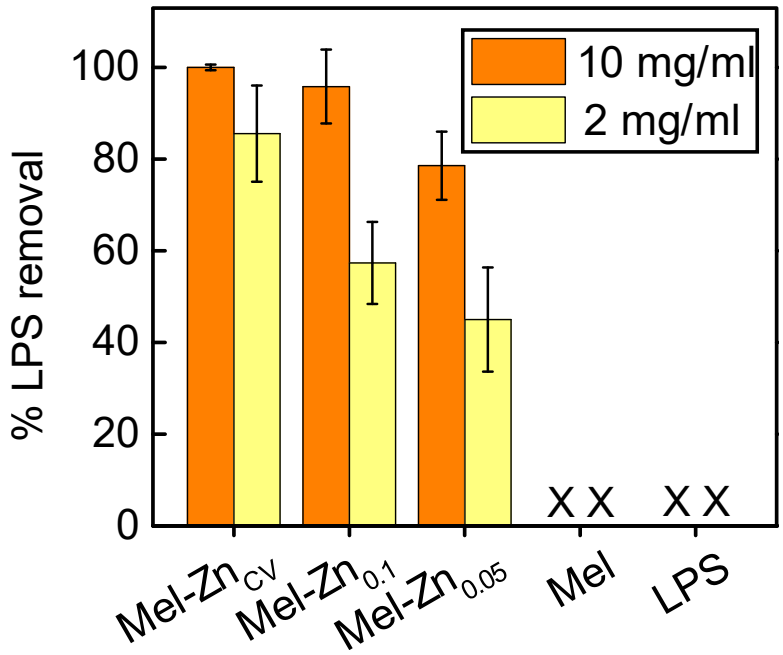

Figure 3.8: LPS removal efficiency after incubation of 10 and 2 mg/ml Mel and Mel-Zn with 1 EU/ml LPS for 1h at 37 °C. X indicates zero percent. Data are presented as mean ± SD, n = 3.

The high selectivity of Mel-Zn toward LPS was not altered by the presence of other proteins such as bovine serum albumin (**Figure 3.9a**). After 1h incubation of 5 mg/ml Mel and Mel-Zn with 1 EU/ml LPS and 20 µg/ml BSA at 37 ℃, 93.99±2.2 %, 94.4±1.6 %, and 67.2±4.1 % of LPS was removed by Mel-Zn_{CV}, Mel-$Zn_{0.1}$, and Mel-$Zn_{0.05}$, respectively. Simultaneously, 102.8 %, 98.48±3 %, and 100±1.3 % of the BSA was recovered from the model solution incubated with Mel-Zn_{CV}, Mel-$Zn_{0.1}$, and Mel-$Zn_{0.05}$, respectively (**Figure 3.9(b)**). It is notable that LPS or *E. coli* removal became more efficient as Zn^{2+} concentration increased, corroborating the hypothesis that binding is mediated through LPS and Zn^{2+} interaction.

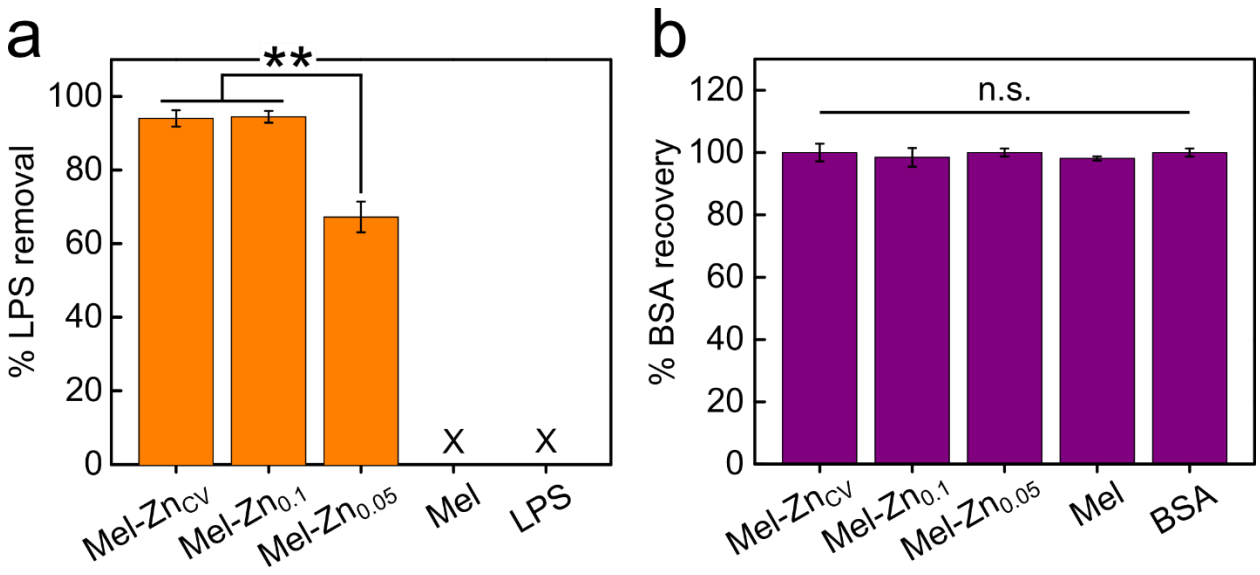

Figure 3.9: (a) High percentage of LPS removal and (b) BSA recovery by the Mel-Zn after 1h incubation of 5 mg/ml Mel and Mel-Zn with 1 EU/ml LPS and 20 µg/ml BSA at 37 °C in the same solution indicate the potential of the Mel-Zn to selectively bind with LPS in the presence of protein. X indicates zero percent. Data are presented as mean ± SD, n = 3. $^{n.s.}p > 0.05$, $*p < 0.05$, and $**p < 0.01$.

3.3.3 Hemocompatibility

Hemocompatibility is a basic requirement for biomaterials that interface human blood. Hemocompatibility of Mel-Zn was test by protein adsorption, blood coagulation and hemolysis. Protein adsorption on biomaterials can initiate the undesirable blood coagulation cascade, which can ultimately be fatal [35]. Protein adsorption on Mel-Zn was studied by incubating Mel-Zn in an aqueous solution of bovine serum albumin (BSA), the most prevalent protein in the human blood (~ 54 mg/ml). Minimal BSA adsorption on Mel-Zn was observed regardless of the amount of zinc loading when melanin was incubated in 1000 and 500 µg/mL BSA in PBS for 1 h (**Figure 3.10**), which is consistent with the earlier reports on melanin-based biomaterials [36]. Low protein adsorption might be due to the hydrophilic groups in melanin such as carboxylic and hydroxyl groups and water molecules forming a hydration layer that prevents the protein adsorption.

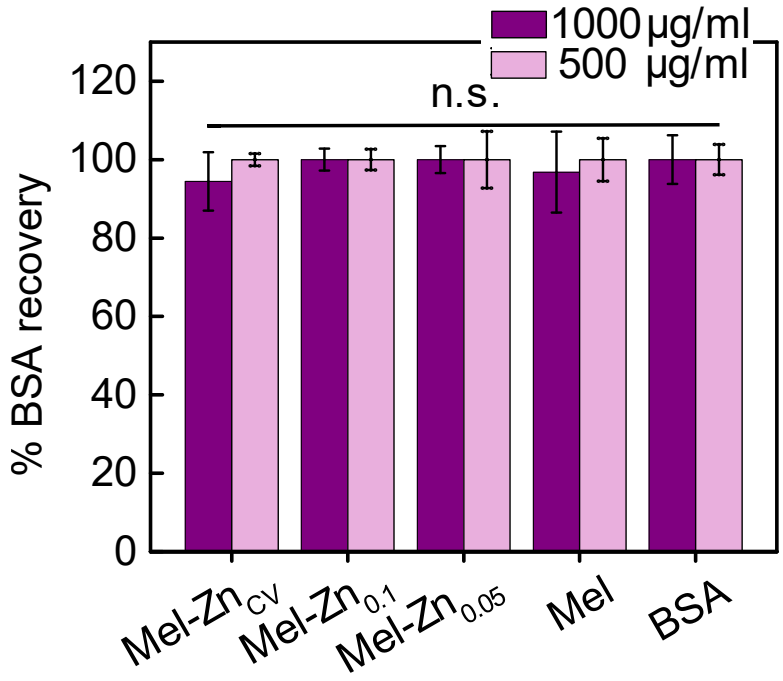

Figure 3.10: Blood compatibility is tested by BSA recovery after incubating melanins (5 mg/ml) within 1000 and 500 µg/ml BSA for 1h at 37 ℃. Data are presented as mean ± SD, n = 3. $^{n.s}p > 0.05$.

Blood coagulation on Mel-Zn was investigated by measuring thrombin-antithrombin III (TAT) complex levels in the blood after the incubation with Mel-Zn for 30 min at 37 °C. TAT complexes are rapidly formed through antithrombin III-mediated neutralization of thrombin, therefore can be used as a proxy for thrombin concentration [35]. No significant TAT complex formation was detected in all melanin groups compared to the negative control ($p > 0.05$) (**Figure 3.11**). The TAT complex levels generated by Mel and Mel-Zn are well below the upper limit of 4.1 ng/ml for a healthy human [37], indicating the exceptional hemocompatibility. This result is in accordance with plasma protein adsorption analysis that indicates no significant protein loss due to introduction to Mel and Mel-Zn.

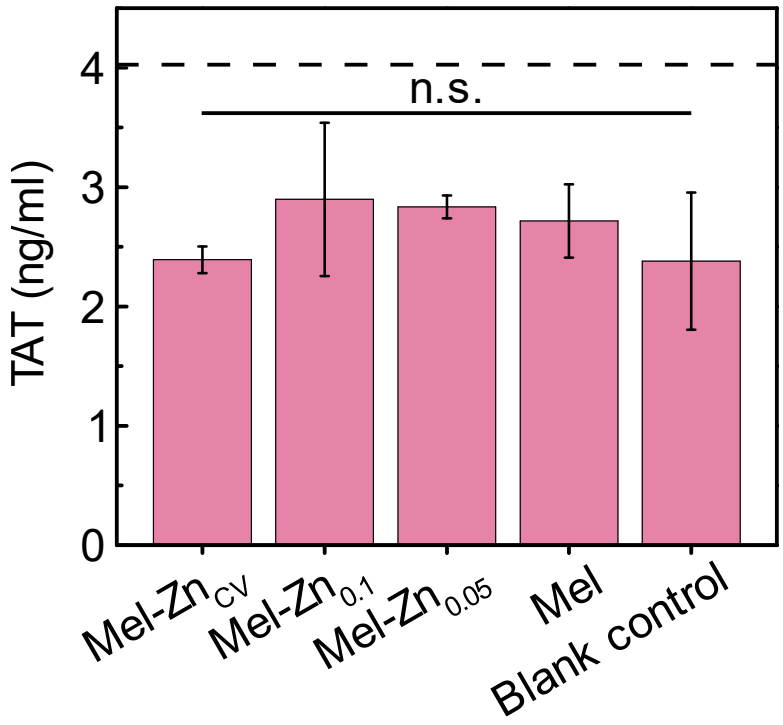

Figure 3.11: Blood coagulation is tested by measuring thrombin antithrombin (TAT) complex levels. TAT levels are shown in (c) after incubation of melanins in human blood for 30 min at 37 °C, which indicates no significant coagulation. Dashed line shows normal upper limit of TAT complex for healthy humans [37]. Data are presented as mean ± SD, n = 3. $^{n.s}$ $p > 0.05$.

Excellent hemocompatibility of Mel-Zn was further confirmed by hemolysis tests. Hemolysis ratios were calculated after incubating 5 mg/ml of melanins with red blood cells (RBC, 2 x 10^8 RBC/ml) for 1 h. As indicated in **Figure 3.12** the hemolysis ratios for Mel, Mel-Zn_{CV}, Mel-$Zn_{0.01}$, and Mel-$Zn_{0.05}$ were 2.18%, 1.65% 1.83%, and 1.74%, respectively. Mel and Mel-Zn show lower hemolysis than the maximum limit permitted (5%) for biomaterials, according to ASTM F756-13 standards [35], [36]. This indicates that Mel-Zn can be used to remove LPS or pathogen from sepsis blood effectively with minimal nonspecific interaction with RBCs.

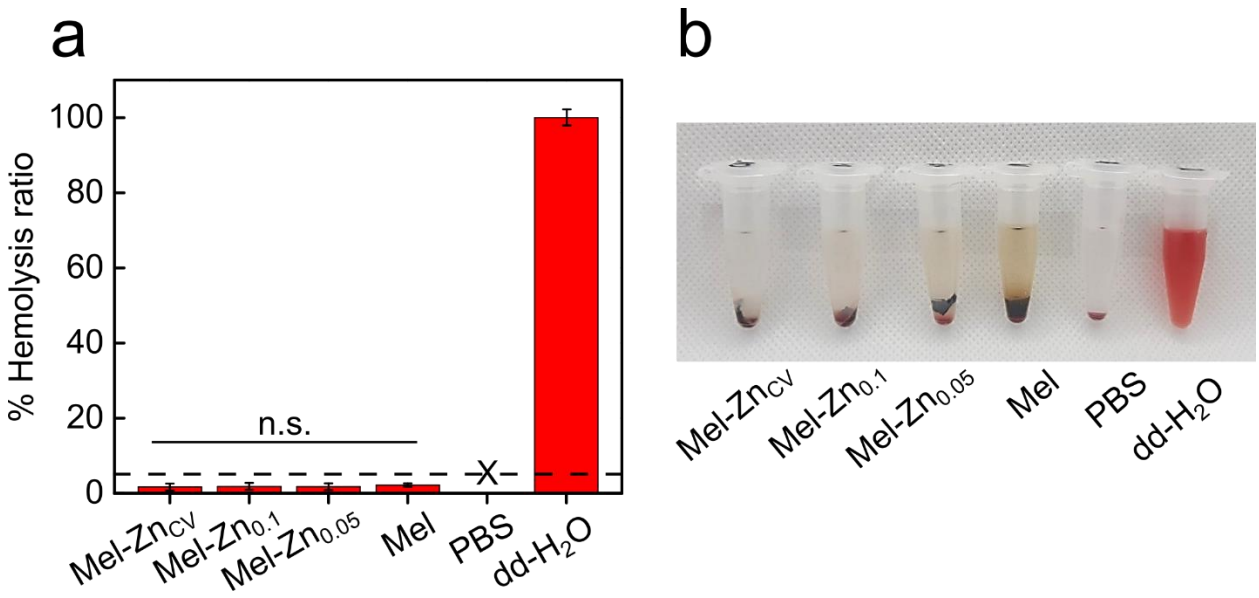

Figure 3.12: Hemolysis ratios are measured and shown in (a) by incubating melanins (5 mg/ml) with human red blood cells (RBCs) at a concentration of 2x10^8 cell/ml for 30 min. No severe damage to RBCs by melanins was observed. Dashed line shows ASTM standard limit (5%) of hemolysis caused by biomaterials. PBS and double-distilled H_2O were used as negative and positive controls, respectively. Digital images of RBC suspensions after incubation with melanin are shown in (b). X indicates zero percent hemolysis. Data are presented as mean ± SD, n = 3. $^{n.s.}p > 0.05$.

3.4 Conclusion

For the removal of bacteria and endotoxin from septic patients, antibody-modified surface has been widely used due to their high specificities for their binding targets. However, there have been inherent limitations regarding the poor separation speed, high production costs, and poor biocompatibilities/hemocompatibilities. This study demonstrated the utility of Zn^{2+}-loaded melanin as an active agent to bind bacteria and endotoxin. Melanin, a naturally occurring biopigment is highly biocompatible and has many favorable features for the physiological systems. Melanin contains various chemical functional groups including pendant carboxylic acids, aromatic amines, and redox-active catechols. Electrochemical Zn^{2+} loading allowed the maximum loading density of Zn^{2+} into melanins compared to the solution method. XPS and Raman analysis corroborated that the loading of Zn^{2+} is largely associated with catechol groups. Zn^{2+}-loaded melanin was found to remove approximately 90% of *E. coli*, and 100% of endotoxin when incubating in PBS buffer and whole blood for 1 h. Moreover, adsorption of protein from individual protein model solutions, as well as LPS-spiked protein solutions, was found to be minimal. In addition, while antibiotic therapies leave behind LPS as cellular debris, simultaneous binding to bacteria and LPS by Mel-Zn enhances the efficacy of antibiotics. Hemolysis and coagulation assays demonstrated the exceptional blood biocompatibility of Mel-Zn. Taken together, melanin would be a promising agent when implemented in an extracorporeal filtration to remove pathogens and endotoxins in acute sepsis patients.

3.5 References

[1] M. Giustozzi *et al.*, “Coagulopathy and sepsis: Pathophysiology, clinical manifestations and treatment,” *Blood Rev.*, vol. 50, p. 100864, Nov. 2021, doi: 10.1016/j.blre.2021.100864.

[2] World Health Organization, *Global report on the epidemiology and burden of sepsis: current evidence, identifying gaps and future directions*. Geneva: World Health Organization, 2020. Accessed: Apr. 05, 2022. [Online]. Available: https://apps.who.int/iris/handle/10665/334216

[3] K. E. Rudd *et al.*, “Global, regional, and national sepsis incidence and mortality, 1990–2017: analysis for the Global Burden of Disease Study,” *The Lancet*, vol. 395, no. 10219, pp. 200–211, Jan. 2020, doi: 10.1016/S0140-6736(19)32989-7.

[4] J.-J. Lee *et al.*, “Synthetic Ligand-Coated Magnetic Nanoparticles for Microfluidic Bacterial Separation from Blood,” *Nano Lett.*, vol. 14, no. 1, pp. 1–5, Jan. 2014, doi: 10.1021/nl3047305.

[5] V. D’Onofrio *et al.*, “Audit of empirical antibiotic therapy for sepsis and the impact of early multidisciplinary consultation on patient outcomes.,” *Int. J. Antimicrob. Agents*, vol. 58, no. 3, p. 106379, Sep. 2021, doi: 10.1016/j.ijantimicag.2021.106379.

[6] M. L. Donnell, A. J. Lyon, M. R. Mormile, and S. Barua, “Endotoxin hitchhiking on polymer nanoparticles,” *Nanotechnology*, vol. 27, no. 28, p. 285601, Jul. 2016, doi: 10.1088/0957-4484/27/28/285601.

[7] T. F. Didar *et al.*, “Improved treatment of systemic blood infections using antibiotics with extracorporeal opsonin hemoadsorption,” *Biomaterials*, vol. 67, pp. 382–392, Oct. 2015, doi: 10.1016/j.biomaterials.2015.07.046.

[8] C. Monard, T. Rimmelé, and C. Ronco, “Extracorporeal Blood Purification Therapies for Sepsis,” *Blood Purif.*, vol. 47, no. Suppl. 3, pp. 2–15, 2019, doi: 10.1159/000499520.

[9] H. Shoji, “Extracorporeal Endotoxin Removal For The Treatment of Sepsis:Endotoxin Adsorption Cartridge (Toraymyxin),” *Ther. Apher. Dial.*, vol. 7, no. 1, pp. 108–114, Feb. 2003, doi: 10.1046/j.1526-0968.2003.00005.x.

[10] L. Papafilippou, A. Claxton, P. Dark, K. Kostarelos, and M. Hadjidemetriou, “Nanotools for Sepsis Diagnosis and Treatment,” *Adv. Healthc. Mater.*, vol. 10, no. 1, p. 2001378, Jan. 2021, doi: 10.1002/adhm.202001378.

[11] I. K. Herrmann *et al.*, “Endotoxin Removal by Magnetic Separation-Based Blood Purification,” *Adv. Healthc. Mater.*, vol. 2, no. 6, pp. 829–835, Jun. 2013, doi: 10.1002/adhm.201200358.

[12] J. H. Kang *et al.*, “An extracorporeal blood-cleansing device for sepsis therapy,” *Nat. Med.*, vol. 20, no. 10, pp. 1211–1216, Oct. 2014, doi: 10.1038/nm.3640.

[13] L. Panzella *et al.*, “Atypical Structural and π-Electron Features of a Melanin Polymer That Lead to Superior Free-Radical-Scavenging Properties,” *Angew. Chem. Int. Ed.*, vol. 52, no. 48, pp. 12684–12687, Nov. 2013, doi: 10.1002/anie.201305747.

[14] A. A. R. Watt, J. P. Bothma, and P. Meredith, “The supramolecular structure of melanin,” *Soft Matter*, vol. 5, no. 19, p. 3754, 2009, doi: 10.1039/b902507c.

[15] M. d’Ischia, A. Napolitano, A. Pezzella, P. Meredith, and T. Sarna, “Chemical and Structural Diversity in Eumelanins: Unexplored Bio-Optoelectronic Materials,” *Angew. Chem. Int. Ed.*, vol. 48, no. 22, pp. 3914–3921, May 2009, doi: 10.1002/anie.200803786.

[16] T. Rahmani Eliato *et al.*, “Melanin pigments extracted from horsehair as antibacterial agents,” *J. Mater. Chem. B*, vol. 9, no. 6, pp. 1536–1545, 2021, doi: 10.1039/D0TB02475A.

[17] Y. J. Kim, W. Wu, S.-E. Chun, J. F. Whitacre, and C. J. Bettinger, “Catechol-Mediated Reversible Binding of Multivalent Cations in Eumelanin Half-Cells,” *Adv. Mater.*, vol. 26, no. 38, pp. 6572–6579, Oct. 2014, doi: 10.1002/adma.201402295.

[18] Y. J. Kim, W. Wu, S.-E. Chun, J. F. Whitacre, and C. J. Bettinger, “Biologically derived melanin electrodes in aqueous sodium-ion energy storage devices,” *Proc. Natl. Acad. Sci.*, vol. 110, no. 52, pp. 20912–20917, Dec. 2013, doi: 10.1073/pnas.1314345110.

[19] A. Krężel and W. Maret, “The biological inorganic chemistry of zinc ions,” *Arch. Biochem. Biophys.*, vol. 611, pp. 3–19, Dec. 2016, doi: 10.1016/j.abb.2016.04.010.

[20] V. Ganesh, K. Bodewits, S. J. Bartholdson, D. Natale, D. J. Campopiano, and J. C. Mareque-Rivas, “Effective Binding and Sensing of Lipopolysaccharide: Combining Complementary Pattern Recognition Receptors,” *Angew. Chem. Int. Ed.*, vol. 48, no. 2, pp. 356–360, Jan. 2009, doi: 10.1002/anie.200804168.

[21] H. T. Ngo, X. Liu, and K. A. Jolliffe, “Anion recognition and sensing with Zn(ii)–dipicolylamine complexes,” *Chem. Soc. Rev.*, vol. 41, no. 14, p. 4928, 2012, doi: 10.1039/c2cs35087d.

[22] E. J. O'Neil and B. D. Smith, "Anion recognition using dimetallic coordination complexes," *Coord. Chem. Rev.*, vol. 250, no. 23–24, pp. 3068–3080, Dec. 2006, doi: 10.1016/j.ccr.2006.04.006.

[23] Y. Li *et al.*, "Bacterial endotoxin (lipopolysaccharide) binds to the surface of gold nanoparticles, interferes with biocorona formation and induces human monocyte inflammatory activation," *Nanotoxicology*, vol. 11, no. 9–10, pp. 1157–1175, Nov. 2017, doi: 10.1080/17435390.2017.1401142.

[24] M. D. Firouzjaei *et al.*, "Recent advances in functionalized polymer membranes for biofouling control and mitigation in forward osmosis," *J. Membr. Sci.*, vol. 596, p. 117604, Feb. 2020, doi: 10.1016/j.memsci.2019.117604.

[25] P. O. Magalhães, A. M. Lopes, P. G. Mazzola, C. Rangel-Yagui, T. C. V. Penna, and A. Pessoa, "Methods of endotoxin removal from biological preparations: a review," *J. Pharm. Pharm. Sci. Publ. Can. Soc. Pharm. Sci. Soc. Can. Sci. Pharm.*, vol. 10, no. 3, pp. 388–404, 2007.

[26] L. Mazgaeen and P. Gurung, "Recent Advances in Lipopolysaccharide Recognition Systems," *Int. J. Mol. Sci.*, vol. 21, no. 2, p. 379, Jan. 2020, doi: 10.3390/ijms21020379.

[27] F. Amini Tapouk *et al.*, "Endotoxin removal from aqueous solutions with dimethylamine-functionalized graphene oxide: Modeling study and optimization of adsorption parameters," *J. Hazard. Mater.*, vol. 368, pp. 163–177, Apr. 2019, doi: 10.1016/j.jhazmat.2019.01.028.

[28] A. A. R. Watt, J. P. Bothma, and P. Meredith, "The supramolecular structure of melanin," *Soft Matter*, vol. 5, no. 19, p. 3754, 2009, doi: 10.1039/b902507c.

[29] H.-A. Park, Y. J. Kim, I. S. Kwon, L. Klosterman, and C. J. Bettinger, "Lithium purification from aqueous solutions using bioinspired redox-active melanin membranes: Lithium purification using bioinspired redox-active melanin membranes," *Polym. Int.*, vol. 65, no. 11, pp. 1331–1338, Nov. 2016, doi: 10.1002/pi.5184.

[30] Y. J. Kim, W. Wu, S.-E. Chun, J. F. Whitacre, and C. J. Bettinger, "Catechol-Mediated Reversible Binding of Multivalent Cations in Eumelanin Half-Cells," *Adv. Mater.*, vol. 26, no. 38, pp. 6572–6579, Oct. 2014, doi: 10.1002/adma.201402295.

[31] V. Capozzi *et al.*, "Raman and optical spectroscopy of eumelanin films," *J. Mol. Struct.*, vol. 744–747, pp. 717–721, Jun. 2005, doi: 10.1016/j.molstruc.2004.11.074.

[32] Z. Shi *et al.*, “Hemocompatible magnetic particles with broad-spectrum bacteria capture capability for blood purification,” *J. Colloid Interface Sci.*, vol. 576, pp. 1–9, Sep. 2020, doi: 10.1016/j.jcis.2020.04.115.

[33] H. H. Dolin, T. J. Papadimos, X. Chen, and Z. K. Pan, “Characterization of Pathogenic Sepsis Etiologies and Patient Profiles: A Novel Approach to Triage and Treatment,” *Microbiol. Insights*, vol. 12, p. 117863611882508, Jan. 2019, doi: 10.1177/1178636118825081.

[34] J. Dien Bard and E. McElvania TeKippe, “Diagnosis of Bloodstream Infections in Children,” *J. Clin. Microbiol.*, vol. 54, no. 6, pp. 1418–1424, Jun. 2016, doi: 10.1128/JCM.02919-15.

[35] N. Jacob Kaleekkal, “Heparin immobilized graphene oxide in polyetherimide membranes for hemodialysis with enhanced hemocompatibility and removal of uremic toxins,” *J. Membr. Sci.*, vol. 623, p. 119068, Apr. 2021, doi: 10.1016/j.memsci.2021.119068.

[36] K. Zhao *et al.*, “Polydopamine-assisted immobilization of L-serine onto PES electrospun fiber membrane for effective endotoxin removal,” *Compos. Commun.*, vol. 20, p. 100365, Aug. 2020, doi: 10.1016/j.coco.2020.100365.

[37] G. Tatra and A. Reinthaller, “Elevated thrombin-antithrombin III complex concentrations in patients with gynaecological malignancy,” *Klin. Wochenschr.*, vol. 69, no. 3, pp. 124–127, Feb. 1991, doi: 10.1007/BF01795956.

CHAPTER 4
Summary

The work present in this dissertation demonstrate potential applications of biologically derived melanin in fighting bacterial infections, including severe and invasive bacteremia. Biomaterials, whether natural or synthetic, play an integral role in biomedical products and devices. Selecting and designing a well-performing biomaterial depends on its specific application and characteristics. Therefore, understanding the structural properties of biomaterials is of great importance. Design and modification of biomaterials facilitate their applications in drug delivery, medical devices, regenerative human tissues, and medical implants. Additionally, this will modulate the host–material interactions to prevent an undesirable host response. I have investigated the structural property of melanin from different sources and demonstrated that it has antibacterial and endotoxin bonding activity.

In Chapter 2, I extracted melanin embedded in *Equus ferus* hair using acid hydrolysis (*Equus*Mel). *Equus*Mel is composed of homogeneous elliptical nanoparticle aggregates. When looking at the transmittance electron microscopy image of *Equus*Mel, the outer surface of melanin granules is multilayered and has several spherical pores distributed across the surface which represents a mesoporous biomaterial. Strong correlation at $q = 0.139$ $Å^{-1}$ from wide-angle (WAXS) and small-angle (SAXS) X-ray scattering presents the order structure of *Equss*Mel with the d-spacing of 45.2 Å. The pore size distribution of *Equus*Mel determined by the Barrett–Joyner–Halenda method exhibits the presence of the primary pores within the range of 30–50 Å. In addition, N_2 adsorption–desorption isotherms indicate that *Equus*Mel contains a Brunaur–

Emmett–Teller (BET) surface area of 3 m^2 /g. The UV-Vis absorption spectrum of *Equus*Mel shows a featureless, monotonically decreasing curve with increasing wavelength, which is in line with typical melanin characteristics. Fourier transform infrared spectroscopy (FTIR) spectra show strong, broad band at approximately 3800–2800 cm^{-1} that has been assigned to stretching vibration of O–H and N–H groups, which are components of carboxylic acid and phenolic OH, and indole amines, respectively. Two distinct peaks observed between 2950-2850 cm^{-1} belongs to stretching vibration of aliphatic C–H in *Equus*Mel. The third strong absorption band, found in the 1720 cm^{-1} zone, corresponds to stretching vibration of aromatic C=O group in carboxylic acid. Two bands at lower wavenumbers are observed at 1650 and 1260 cm^{-1}. These features are assigned to conjugated C=C stretching vibration and C–N stretching vibration in indole. The Raman spectra is deconvoluted in 5 peaks using a Voigt function. The peak positioned at 1590 cm^{-1} (ε) is corresponding to vibration of aromatic C=C in indole structure. The peak centered at 1510 cm^{-1} (δ) has been assigned to stretching vibration of C=N in semiquinone and bending vibration of N–H. The bands recorded at 1418 cm^{-1} (γ) and 1341 cm^{-1} (β) are associated with pyrrole ring stretching and vibration of aromatic C–N in indole, respectively. The smallest wavenumber 1220 cm^{-1} (α) is attributed to C–O stretching in carboxylic acid and C–OH. X-ray photoelectron spectroscopy (XPS) survey peak and elemental analysis of *Equus*Mel and synthetic melanin (SynMel) indicate that *Equus*Mel contains more carbon and less oxygen and nitrogen elements compared to SynMel. Each high-resolution C1s and O1s peaks is deconvolved into two peaks at binding energies of 284.8, 287.22, 532.39, 533.82, and 531.12 eV, which were associated with the chemical signature of C–C/C=C, C–N/C–O, C–OH, COOH, and C–O, respectively. About, 13.3% and 19.9% of the Subunits of *Equus*Mel and SynMel contain catechol groups.

The antibacterial activity of *Equus*Mel and SynMel against *Escherichia coli* and *Staphylococcus aureus* was quantitatively evaluated using a colony count method after exposure to varying concentrations of melanin for 4 h. The number of colony forming units (CFU) dropped dramatically at almost every concentration for both melanin types and bacteria species. Apart from 2.5 mg/ml *Equus*Mel, all concentrations of both melanin types had significant decreases in bacterial growth for both *E. coli* and *S. aureus*. The antibacterial effect of SynMel against *E. coli* and *S. aureus* was stronger than *Equus*Mel at the lower melanin concentrations of 2.5 mg/ml and 5 mg/ml after 4 h of exposure. 150 mg/ml of SynMel and *Equus*Mel were tested against *E. coli* and *S. aureus* at 1, 2, 4, and 24 h. A complete reduction in bacterial growth was observed after 2 h incubation with SynMel and 4 h incubation with *Equus*Mel. I measured the H_2O_2 content of SynMel and *Equus*Mel solutions at different concentrations of 2.5, 5, 20 and 150 mg/ml at 4 h. Measurable levels of H_2O_2 were detected in all the samples, indicating the potential of *Equus*Mel and SynMel to generate reactive oxygen species and eventually damage bacterial cells. The amounts of H_2O_2 produced from SynMel are 1.5 times higher than *Equus*Mel, which is in close agreement with findings of the chemical signatures of redox-active groups in *Equus*Mel.

In Chapter 3, I loaded Zinc cations (Zn^{2+}) in melanin either in aqueous electrolyte in a half-cell or incubated them in zinc solution (0.1 and 0.05 M). XPS survey peak demonstrates noticeable Zn peaks for Mel-Zn_{cv}, Mel-$Zn_{0.1}$, and Mel-$Zn_{0.5}$. A quantitative comparison utilizing the weight percent ratio of Zn to C peak areas shows an absence of Zn in Mel samples, while positive values were calculated for Mel-Zn samples, indicating the successful loading of zinc on melanin. High-resolution Zn 2p peaks, further confirm the zinc coupling on melanin structure. Raman spectra of Mel and Mel-Zn were deconvolved into five peaks (α-ε) that are assigned to the known prominent functional groups in melanin substituents. Significant peak shifts are observed in Mel-Zn

compared to Mel. The presence of Zn^{2+} influences the vibrational modes in melanin protomolecules relative to the complementary Mel. The largest peak shift is observed in α, which suggests the mesoscale reconfiguration of melanin after zinc loading.

An infection model of sepsis in whole blood and PBS was established using gram-negative *E. coli* at a concentration of 5×10^5 CFU/ml. Mel-Zn_{CV} attained the highest efficiency of *E. coli* removal in both PBS and blood sepsis model. Furthermore, *E. coli* removal percentage from the more complex composition of whole blood is approximately the same as PBS, supporting the rationale of using Mel-Zn for infected bloodstream purification. Mel-Zn removes lipopolysaccharide (LPS) equally as well as living *E. coli* as indicated by percentage of LPS removal after incubating 10 and 2 mg/ml Mel and Mel-Zn with 1 EU/ml LPS for 1 h at 37 ℃. Much as I observed in the pathogen removal studies, Mel-Zn_{CV} removed 100% and 85.56% of LPS at 10 mg/ml and 2 mg/ml, respectively. Likewise, Mel-$Zn_{0.1}$ and Mel-$Zn_{0.05}$ achieved LPS removal of 95.83% and 78.55% at 10 mg/ml, while at 2 mg/ml concentration, LPS removal reduced to 57.35% and 44.99%, respectively. It is notable that LPS or *E. coli* removal percentages increased with increasing the Zn^{2+} concentration, corroborating the rational in bonding between LPS and Zn^{2+}.

I used bovine serum albumin (BSA) to simulate human plasma protein. More than 94% BSA recovery at concentrations of 1000 and 500 μg/mL after 1 h contact with Mel and Mel-Zn suggests high blood compatibility. Mel-Zn showed high selectivity toward LPS in the presence of protein. After 1h incubation of 5 mg/ml Mel and Mel-Zn with 1 EU/ml LPS and 20 μg/ml BSA at 37 ℃, 93.99%, 94.4% and 67.2% of LPS was removed by Mel-Zn_{CV}, Mel-$Zn_{0.1}$ and Mel-$Zn_{0.05}$, respectively. Simultaneously, 100%, 98.48% and 100% of the BSA was recovered from the model solution incubated with Mel-Zn_{CV}, Mel-$Zn_{0.1}$ and Mel-$Zn_{0.05}$, respectively. I determined

coagulation activation by measuring Thrombin-antithrombin complex (TAT) levels in the blood. Compared to the negative control, no significant TAT complex formation was detected ($p > 0.05$) after incubation of human blood with Mel and Mel-Zn for 30 minutes at 37 °C, which suggests no coagulation cascade activation. The hemolysis ratios caused by Mel, Mel-Zn_{CV}, Mel-$Zn_{0.01}$ and Mel-$Zn_{0.05}$ were 2.18%, 1.65% 1.83% and 1.74%, respectively. Mel and Mel-Zn showed no significant differences in the hemolysis ratios ($p > 0.05$). These results demonstrate that Mel-Zn can be used to remove LPS or pathogen from sepsis blood with minimal nonspecific interaction with red blood cells.

4.1 Future work

Facile extraction of *Equus*Mel and its unique antibacterial property makes this biomolecule an ideal candidate to be used as a coating in biomedical devices to prevent biofilm formation and bacteria colonization. Also, it has potential to be used as a therapeutic against bacterial infection in skin or soft-tissue wounds. Beyond the medical field, *Equus*Mel can be used in many other areas where biofilm-prevention and bacteria mitigation are important, such as wastewater filtration. Further studies into molecular level modification of melanin surfaces such as exfoliation may extend the redox functionalities and improve antibacterial activity.

Mel-Zn could be adapted for clinical use in an extracorporeal membrane to remove bacteria and LPS in acute sepsis patients. This could provide much needed additional time to identify both the nidus of infection and the invading pathogen and to initiate appropriate antibiotic therapy. Polymers such as polyvinylidene fluoride (PVDF), polyethersulfone (PES), polyvinylpyrrolidone (PVP), and polyvinyl alcohol (PVA) are commonly used for fabricating membranes via techniques

such as phase inversion, electrospinning, and dry-jet wet-spinning. Melanin can be incorporated in the membrane structure during the fabrication process to take advantages of its LPS bonding during blood filtration (**Figure 4.1**). It should be mentioned that Mel-Zn could be used for other applications, including removing bacterial contaminants from water or LPS from pharmaceutical products.

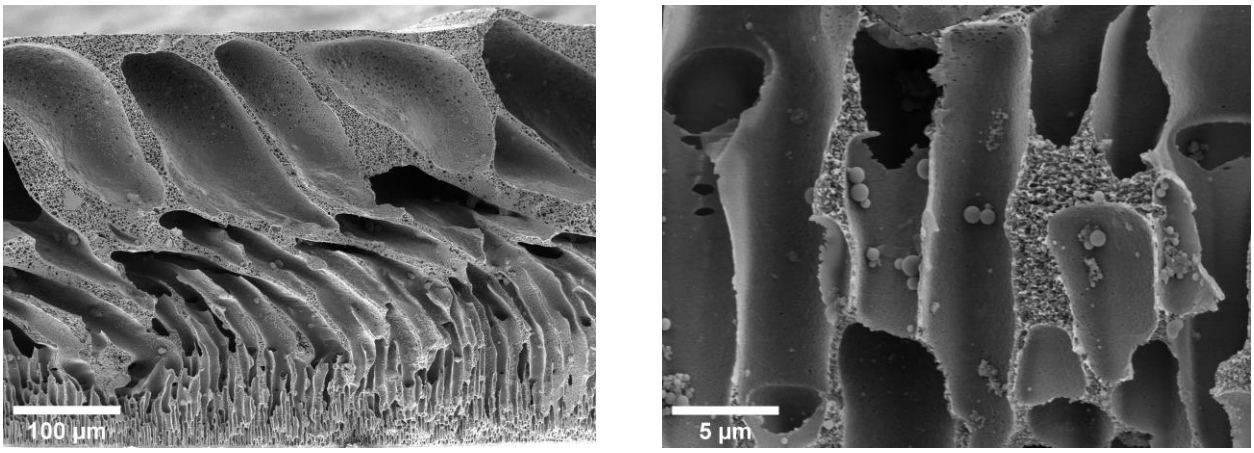

Figure 4.1: Porous structure of a melanin-based PES-PVP membrane prepared by phase inversion method. The cross section of the membrane is composed of a typical asymmetric porous structure with a skin layer and a parallel finger-like sublayer.

In this dissertation, I show that Mel-Zn can be used for separation of LPS from septic blood. This provides a foundation for the future studies. Since time is a critical component of LPS removal, rapid binding formation (less than 1 hour) between the Mel-Zn and LPS is important and should be studied in the future. Here I show more than 94% BSA recovery at concentrations of 1000, 500, and 20 µg/mL after being in contact with 5 mg/ml Mel and Mel-Zn. In the future, this experiment should be repeated with higher concentrations of protein to model the composition of human blood.